

Syracuse University

**SURFACE**

---

Dissertations - ALL

SURFACE

---

May 2014

## Solving time domain scattering and radiation problems in a marching-on-in-degree technique for method of moment

Zicong Mei  
*Syracuse University*

Follow this and additional works at: <https://surface.syr.edu/etd>



Part of the [Engineering Commons](#)

---

### Recommended Citation

Mei, Zicong, "Solving time domain scattering and radiation problems in a marching-on-in-degree technique for method of moment" (2014). *Dissertations - ALL*. 116.

<https://surface.syr.edu/etd/116>

This Dissertation is brought to you for free and open access by the SURFACE at SURFACE. It has been accepted for inclusion in Dissertations - ALL by an authorized administrator of SURFACE. For more information, please contact [surface@syr.edu](mailto:surface@syr.edu).

# Abstract

The time domain method of moment has been proposed for a long time. The marching-on-in-time solver suffers from late time instability, while the marching-on-in-degree technique can avoid this problem.

This thesis introduces a new temporal basis function and a new Green's function form that improves the computation speed of the marching-on-in-degree technique. This method can be used for the perfect conductor and can also be applied to conductors with loss or dielectric.

As a method of moment solver, this marching-on-in-degree technique must solve a dense matrix equation and it may be time consuming if the objects are very large. Therefore, parallelization and a hybrid method are also proposed to handle large objects.

This thesis will cover all my improvements to the time domain marching-on-in-degree method.

**Solving time domain scattering and radiation  
problems in a marching-on-in-degree technique  
for method of moment**

Zicong Mei

Dissertation

Submitted in partial fulfillment of the requirements for the degree of Doctor of  
Philosophy in Electrical Engineering in the Graduate School of Syracuse University.

May 2014

Copyright 2014 Zicong Mei

All Rights Reserved

# Acknowledgement

First, I want to thank my advisors Tapan K. Sarkar and Magdalena Salazar-Palma. I am very lucky to have had the benefit of their time and ideas during my Ph. D. period. I was fortunate to have Prof. Sarkar and Salazar-Palma, who are also world famous scholars, to guide my research.

I want to thank the support of my family during my pursuing of this degree. It is impossible to finish this achievement without their help.

I also want to thank Prof. Yu Zhang, Prof. Baek-Ho Jung, and Dr. Zhong Ji, who initiated my research topic. They, especially Dr. Yu Zhang, taught me many basic concepts of how to start my research.

My defense committee members also spent much time and effort reading my thesis and helping me with the defense. Therefore, I would like to thank Dr. Carlos Hartmann, Dr. Duane Marcy, Dr. Jay K. Lee, and my committee chair Dr. Kathy Vander Werff.

Daniel García Doñoro is the first student that I want to thank. He helped me a lot in developing the software and taught me the basic concepts of software.

I also want to thank all the members in the CEMLAB: Dr. Xiaopeng Yang, Dr. Santana Burintramart, Dr. Mary Taylor, Dr. Arijit De, Dr. Sio Weng Ting, Dr. Woojim Lee, Dr. Jinhwan Koh, Dr. Weixin Zhao, Walid Dyab, Mohammad Abdallah, Latoya Brown, and HongSik Moon. They helped and inspired me very much in my courses and research.

# Table of Contents

Chapter 1.	Introduction.....	1
Chapter 2.	Time-Domain Electric Field Integral Equation for Conducting Object .....	5
2.1	The Time-Domain Electric Field Integral Equation .....	5
2.2	Spatial Basis Functions .....	7
2.3	Temporal Basis Functions.....	10
2.4	Testing of the Integral Equation.....	12
Chapter 3.	The Improvements of the Temporal Basis Function.....	17
3.1	New Combination of Temporal Basis Functions .....	18
3.2	Testing Procedure and the Matrix Equation.....	20
3.3	Property of Green's Function Terms.....	22
3.4	Improvement of the Computation Time.....	24
3.5	Solution for the Unperfected Metal Surface .....	25
3.6	Numerical Examples for the Improved Time Domain MoM.....	29
3.6.1	Use of Various Excitation Sources .....	30
3.6.2	Improved Performance in Accuracy and Stability .....	31
3.6.3	Improvement in Computational Efficiency of the New MOD Method.....	33
3.6.4	The Examples of Large Objects.....	38
Chapter 4.	The Time Domain MoM Method for Dielectric Objects.....	47
4.1	Time Domain PMCHW Equation .....	48

4.2	Basis Functions of the Time Domain PMCHW Equations.....	51
4.3	Testing of the Time Domain PMCHW Equations .....	53
4.4	Numerical Examples .....	57
	Example 4-1: A Dielectric Sphere .....	57
	Example 4-2: A Dielectric Cylinder .....	57
	Example 4-3: Structures with Different Relative Permittivity .....	59
	Example 4-4: Structures with Different Relative Permeability .....	59
Chapter 5.	Parallelization of the Time Domain MoM Code .....	61
5.1	Parallelization Architecture of the Time Domain MoM .....	61
5.2	Matrix Filling .....	62
5.3	Solving the Matrix Equation .....	66
5.4	Numerical Examples for the Parallelization.....	68
Chapter 6.	A Hybrid Method of Moment and Physical Optics Method.....	77
6.1	Solving the Current in the MoM Region by EFIE .....	78
6.2	Solving the Current in the PO Region.....	82
6.3	Solve the Hybrid MoM-PO Problem Iteratively .....	84
6.4	Numerical Examples .....	86
6.5	Conclusion.....	94
Appendix A.	The Laguerre Function and Related Integrals.....	95
Appendix B.	The Singularity of the Surface Integrals .....	99

Appendix C. The Choice of Scaling Factor.....	103
C.1 Introduction.....	103
C.2 Development of the Least Upper Bound .....	104
C.3 Optimum Scaling Factor in Sense of the Least Upper Bound .....	112
C.4 Examples.....	113
C.5 Conclusion .....	115
Appendix D. Numerical Accuracy for MOD Integrals.....	117
D.1 Introduction.....	117
D.2 Difference in Greens' Function Terms .....	118
D.3 Examples.....	122
D.4 Conclusion .....	130
References.....	131
Publications.....	137



## List of Figures

Figure 2.1 The MoM scattering problem.....	5
Figure 2.2 An arbitrarily-shaped conducting wire with a segmentation scheme.....	8
Figure 2.3 A pair of triangular patches associated with a non-boundary edge.....	9
Figure 3.1 The T-pulse.....	31
Figure 3.2 Triangular patch model for a pair of 0.6 m $\times$ 0.6 m conducting plates connected at an angle of 5°.....	33
Figure 3.3 Current on the conducting plates computed by the improved MOD method plotted against the results from the conventional MOD and the IDFT of the frequency-domain MoM solution.....	33
Figure 3.4 Transient response at the central point of the dipole due to an incident $T$ -pulse.....	35
Figure 3.5 Transient response at a point near the end of the Helix due to an incident $T$ -pulse.....	36
Figure 3.6 Current response in the frequency domain at a point on the loop antenna illuminated by a $T$ -Pulse. (a) Magnitude. (b) Phase. ....	37
Figure 3.7 The $\theta$ -component of the back scattered wave from a 1m-radiused sphere with an incident pulse of 200MHz.....	39
Figure 3.8 The $\theta$ -component of the back scattered wave from a 1m-radiused sphere with an incident pulse of 400MHz.....	40
Figure 3.9 A sedan with triangular mesh.....	41
Figure 3.10 The current distribution at different time steps. ....	43

Figure 3.11 Triangular patch model for a Boeing-737 Aircraft with a size of $26 \text{ m} \times 26 \text{ m} \times 11 \text{ m}$ .	44
Figure 3.12 Transient current distributions on the Boeing-737 aircraft.	45
Figure 4.1 Problem for a dielectric object.	47
Figure 4.2 Transient scattered far field from a dielectric sphere of $\epsilon_r = 1$ and $\mu_r = 0.5$ ...	58
Figure 4.3 Transient scattered far field from a dielectric cylinder of $\epsilon_r = -2$ and $\mu_r = -1$ .	58
Figure 4.4 Transient scattered far field from a dielectric sphere with $\mu_r = 1$ : (a) $\epsilon_r = 0.5$ . (b) $\epsilon_r = 10$ .	59
Figure 4.5 Transient scattered far field for a dielectric sphere with $\epsilon_r = 2$ : (a) $\mu_r = 1$ . (b) $\mu_r = 2$ .	60
Figure 5.1 The difference between a distributed memory system and a shared memory system.	62
Figure 5.2 The distribution of matrix in Example 1.	64
Figure 5.3 The distribution of matrix in Example 2.	65
Figure 5.4 The distribution of matrix in Example 3.	66
Figure 5.5. The far field comparison of the time and frequency domain results for the first numerical example.	70
Figure 5.6 The far field comparison of the time and frequency domain results for the second numerical example.	70
Figure 5.7 The comparison of parallel efficiency for different number of unknowns	72
Figure 5.8 A sedan with a monopole antenna on the roof.	73
Figure 5.9 Comparison of the far field result in time and frequency domain.	73
Figure 5.10 A dipole inside a dielectric sphere.	74

Figure 5.11 Comparison the far field results in the time and frequency domain.....	75
Figure 6.1. The iterative method for analyzing a hybrid MoM-PO problem. ....	86
Figure 6.2. A dipole and a plate reflector .....	88
Figure 6.3. The T-pulse fed into the dipole .....	88
Figure 6.4. The spectrum of the T-pulse fed into the dipole.....	89
Figure 6.5. The far field radiated at the direction of direction of $\theta = \varphi = 0^\circ$ . ....	89
Figure 6.6. The far field radiated at the direction of direction of $\theta = 90^\circ, \varphi = 0^\circ$ . ....	90
Figure 6.7. A dipole over a Boeing 737 plane .....	91
Figure 6.8. Transient current density distribution on the Boeing aircraft.....	94
Figure B.1 Geometric of the RWG basis function.....	101
Figure C.1 The least upper bound and the error for different scaling factor for the pulse given in Example 1 .....	115
Figure C.2 The error for different scaling factor for the pulse shown in Example 2.....	115
Figure D.1 The time domain Green's function $G_{TD}$ . ....	121
Figure D.2 The frequency domain Green's function $G_{FD}$ .....	122
Figure D.3 Orientation of the two basis functions for Example 1 .....	123
Figure D.4 Relative error in the evaluation of $A_{mnab}^{TD}$ and $A_{mn}^{FD}$ for Example 1. ....	124
Figure D.5 Relative error in the evaluation of $B_{mnab}^{TD}$ and $B_{mn}^{FD}$ for Example 1. ....	124
Figure D.6 The two basis functions for Example 2. ....	126
Figure D.7 Relative error in the evaluation of $A_{mnab}^{TD}$ and $A_{mn}^{FD}$ in Example 2.....	127
Figure D.8 Relative error in the evaluation of $B_{mnab}^{TD}$ and $B_{mn}^{FD}$ in Example 2.....	128
Figure D.9 Relative error in the evaluation of $A_{mnab}^{TD}$ and $A_{mn}^{FD}$ in Example 3.....	129

Figure D.10 Relative error in the evaluation of  $B_{mmab}^{TD}$  and  $B_{mn}^{FD}$  in Example 3..... 129

# List of Tables

Table 3.1. The number of operations for the conventional and the new MOD methods..	25
Table 3.2 Comparison of the computation time for the analysis of the dipole using different time-domain methods.....	35
Table 3.3 Comparison of computation time for the analysis of the helix using different time-domain methods.....	36
Table 3.4 Comparison of computation time for the analysis of the loop antenna using different time-domain methods.....	38
Table 5.1. Examples for ScaLAPACK distributing the matrix for different process grids and block sizes. ....	63
Table 5.2. Comparison of the parallel time domain code for different number of CPU cores for a 2160-unknown problem. ....	71
Table 5.3. Comparison of the parallel time domain code for different number of CPU cores for a 5949-unknown problem. ....	72
Table 6.1. Convergence test of different iterations.....	90
Table 6.2. Reduction in memory usage and computation time.....	90
Table D.1. Numerical error for time domain integrals .....	125
Table D.2. Numerical error for frequency domain integrals .....	125
Table D.3. Numerical error for time domain integrals .....	126
Table D.4. Numerical error for frequency domain integrals .....	127

# Abbreviations

CFIE	Combined field integral equation
CPU	Central processing unit
DC	Direct current
EFIE	Electric-field integral equation
FDTD	Finite difference time domain
FEM	Finite element method
GUI	Graphical user interface
HOBBIES	Higher order basis based integral equation solver (An electromagnetics software)
IDFT	Inverse discrete Fourier transform
LU decomposition	Lower-upper decomposition
MFIE	Magnetic Field Integral Equation
MOD	Marching-on-in-degree
MoM	Method of moment
MOT	Marching-on-in-time
MPI	Message passing interface
PEC	Perfect electric conductor
PMCHW	Poggio, Miller, Chang, Harrington and Wu
PO	Physical optics
RWG	Rao-Wilton-Glisson
ScaLAPACK	Scalable linear algebra package (A computer library)
TD-EFIE	Time domain EFIE
TD-PMCHW	Time domain PMCHW

# Chapter 1.

## Introduction

This thesis introduces the *marching-on-in-degree* (MOD) method, which is a time domain method of moment (MoM) solver, as a way to solve the transient electromagnetic response from conducting and dielectric objects. The method of moment is a general method for solving linear systems that is widely applied to electromagnetic radiation and scattering systems. [1] It usually contains integrals of current or other parameters to set up equations in terms of fields. Unlike other kinds of solvers, such as finite element method (FEM) or finite difference time domain method (FDTD) that compute the field in the whole volume, Mom only needs to perform the computation on the surface of the objects and does not need a boundary to include all the components. Therefore, it can greatly reduce the number of unknowns, especially when the components are far away.

Researchers have applied the MoM to time domain problems for a long time.[2] The conventional methodology to solve this problem takes the form of a *marching-on-in-time* (MOT) algorithm, which splits the entire time domain into many time samples and calculates sample by sample [2]-[8]. However, the MOT method may suffer from a late time instability and may not provide reliable results in some cases [5]-[14]. Therefore, an alternative MOD technique has been proposed to overcome this instability [15]-[17]. In the MOD method, the transient response is approximated by a set of *associated Laguerre polynomials*, which are a set of causal orthogonal functions defined in the interval  $[0, +\infty)$  [18][19]. By choosing the associated Laguerre polynomials to represent the transient part

of the response, the time domain integral can be analytically analyzed and temporal variables can be eliminated from the final computational equations. In the computation of the unknowns, the equation does not rely on the temporal variables and purely relies on the unknowns of lower degree. After obtaining these unknowns of lower degree, the unknowns of the next higher degree can be computed. This is why it is called marching-on-in-degree method.

The current and potential on the object surfaces are expanded by both temporal and spatial basis functions. The procedure for solving the integral equations using the MOD method is based on application of Galerkin's testing method, twice, for separate temporal and spatial testing. In the spatial expansion and testing, piecewise triangular basis functions are used for wires and Rao-Wilton-Glisson (RWG) basis functions are used for surfaces. The time variation in the MOD scheme is approximated by a set of orthogonal temporal basis functions — *associated Laguerre functions* — which are derived from the *Laguerre polynomials*. These basis functions are also used for temporal testing.

In previous work in this field, only one associated Laguerre polynomial is used in each temporal basis function. It is a complete and orthogonal basis function set and can represent all the transient processes. However, this approach has a drawback in that the derivative of the associated Laguerre polynomial is a summation of its lower degrees. Consequently, the final equations that are programmed contain many summations. Therefore, I proposed a new basis function set, which is a combination of associated Laguerre polynomials. This basis function set retains all the advantages of the associated



Laguerre polynomials while its derivative is another combination of polynomials instead of a summation; this reduces the computation time by a factor about 10 to 20.

This thesis includes six chapters. This first chapter introduces the background of the research. The remaining five chapters cover the MOD method with different applications.

Chapter 2 is a summary and brief introduction to the MOD method for time domain electromagnetics problems.

Chapter 3 contains my improvements to the MOD methods for conducting surfaces. It includes the new temporal basis function and an organization of Green's function. The new temporal basis function contains a combination of Laguerre polynomials so that it can automatically satisfy the initial condition. In addition, Green's function can be combined so that the computation can be much faster. These improvements speed up the computation 10–20 times. Cases of unperfected conducting objects such as skin effect loss or other types of arbitrary loss with a definition in time or frequency domain are also included.

Chapter 4 introduces the application of MOD method to dielectric surfaces. I apply the MOD method to the PMCHW (Poggio, Miller, Chang, Harrington, and Wu) equation so that it can solve the dielectric objects in time domain.

Chapter 5 contains the method of parallelization of the time domain MOD method. The popular existing parallelization setups are first summarized and an explanation is given to justify why MPI is chosen to implement the job. I also explain the way I distribute the matrix into different machines and compute the problem in detail.

Chapter 6 describes a hybrid method of MOD and physical optics. The MOD can solve the problem quickly with the improvements, but the memory usage and computation time still increase as a square and a cube, respectively, of the number of unknowns. This reaches the limit of computers very quickly. Physical optics is an asymptotic technique and the memory usage and computation time increase linearly with the number of unknowns. However, it cannot handle fine and small components accurately. A hybrid method between these two methods is developed that can solve some of these problems both rapidly and accurately.

## Chapter 2.

# Time-Domain Electric Field Integral Equation for Conducting Object

### 2.1 The Time-Domain Electric Field Integral Equation

The objective of this section is to introduce how to obtain the current distribution in time domain on structures with conducting thin wires and surfaces when illuminated by an incident electromagnetic pulse, as shown in Figure 2.1. For method of moment, the current on the object surfaces are solved. The scattered wave is then computed from the time domain Green's function.

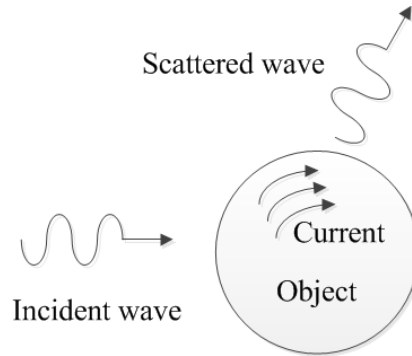


**Figure 2.1** The MoM scattering problem.

For a perfect electric conductor (PEC), the shape of the objects comes into the picture by enforcing the boundary condition, which is that the tangential electric field on the boundary is zero. Therefore, one has

$$\left(\mathbf{E}^i(\mathbf{r},t) + \mathbf{E}^s(\mathbf{r},t)\right)_{\tan} = 0, \quad \text{for } \mathbf{r} \in S \quad (2.1)$$

where  $\mathbf{E}^i$  is the incident electric field and  $\mathbf{E}^s$  is the scattered electric field due to the induced current  $\mathbf{J}$ . The subscript ‘tan’ denotes the tangential component. The scattered electric field is also expressed in terms of the scalar and vector potentials as

$$\mathbf{E}^s(\mathbf{r}, t) = -\frac{\partial}{\partial t} \mathbf{A}(\mathbf{r}, t) - \nabla \Phi(\mathbf{r}, t) \quad (2.2)$$

where  $\mathbf{A}$  and  $\Phi$  are the magnetic vector and the electric scalar potential, respectively. They are given by

$$\mathbf{A}(\mathbf{r}, t) = \frac{\mu}{4\pi} \int_S \frac{\mathbf{J}(\mathbf{r}', \tau)}{R} dS' \quad (2.3)$$

$$\Phi(\mathbf{r}, t) = \frac{1}{4\pi\epsilon} \int_S \frac{\rho(\mathbf{r}', \tau)}{R} dS' \quad (2.4)$$

and  $R = |\mathbf{r} - \mathbf{r}'|$  represents the distance between the arbitrary observation point  $\mathbf{r}$  and the source point  $\mathbf{r}'$  located on the surface. The retarded time  $\tau$  is defined as  $\tau = t - R / c$ , where  $c$  is the velocity of the electromagnetic wave propagation in that space. The parameters  $\mu$  and  $\epsilon$  are the permeability and permittivity of free space, respectively, and  $\rho$  is the surface-charge density. The electric current and the electric charge density described in Eq. (2.3) and (2.4) can be expressed in terms of a Hertz vector  $\mathbf{u}(\mathbf{r}, t)$  defined by

$$\mathbf{J}(\mathbf{r}, t) = \frac{\partial}{\partial t} \mathbf{u}(\mathbf{r}, t) \quad (2.5)$$

$$\rho(\mathbf{r}, t) = -\nabla \cdot \mathbf{u}(\mathbf{r}, t) \quad (2.6)$$

Substitution of Eqs. (2.2) to (2.6) into Eq. (2.1) results in

$$\left( \frac{\mu}{4\pi} \frac{\partial^2}{\partial t^2} \int_S \frac{\mathbf{u}(\mathbf{r}', \tau)}{R} dS' - \frac{\nabla}{4\pi\epsilon} \int_S \frac{\nabla' \cdot \mathbf{u}(\mathbf{r}', \tau)}{R} dS' \right)_{\tan} = \left( \mathbf{E}^i(\mathbf{r}, t) \right)_{\tan} \quad (2.7)$$

Here, one obtains an integral equation with an unknown value of Hertz potential. Using the Hertz potential instead of current directly provides the advantage that the charge density is a time integral of current; one then needs a time derivative on the whole equation to remove this integral. When the excitation is a non-continuous wave, the derivative will have problems, whereas the Hertz potential does not suffer from this drawback.

In order to solve the time-domain electric field integral equation (TD-EFIE) of Eq. (2.7) using Galerkin's method, the basis functions must first be defined.

## 2.2 Spatial Basis Functions

The potential on the wire is expanded with a piecewise triangular basis function and on the surface it is expanded with an RWG basis function. The thin-wire structure to be analyzed is approximated by straight wire segments, as illustrated in Figure 2.2. The wire is divided into  $N$  segment pairs. The piecewise triangular basis function associated with the Hertz potential at the  $n$ -th common node at  $\mathbf{r}_n$  is defined by

$$\mathbf{f}_n(\mathbf{r}) = \mathbf{f}_n^+(\mathbf{r}) + \mathbf{f}_n^-(\mathbf{r}) \quad (2.8)$$

where

$$\mathbf{f}_n^\pm(\mathbf{r}) = \begin{cases} \pm \frac{\mathbf{l}_n^\pm}{\Delta l_n^\pm}, & \mathbf{r} \in L_n^\pm \\ 0, & \mathbf{r} \notin L_n^\pm \end{cases} \quad (2.9)$$

$$\Delta l_n^\pm = \sqrt{|\mathbf{r}_n - \mathbf{r}_n^\pm|^2 + a^2} \quad (2.10)$$

$$\mathbf{l}_n^\pm = \mathbf{r} - \mathbf{r}_n^\pm \quad (2.11)$$

In the above equations,  $\Delta l_n^\pm$  is the length of the segment  $L_n^\pm$ ,  $\mathbf{l}_n^\pm$  is the local position vector, and  $a$  is the radius of the wire.

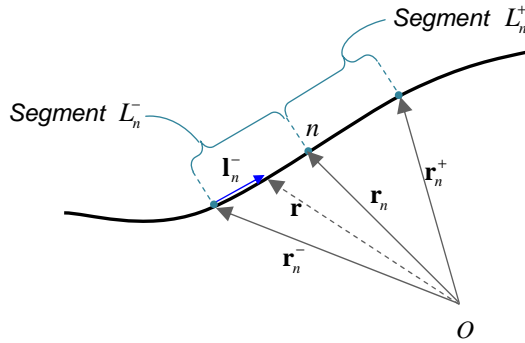


**Figure 2.2** An arbitrarily-shaped conducting wire with a segmentation scheme.

Assuming that the surface of the structure is to be meshed by many planar triangular patches, consider a pair of triangles  $T_n^+$  and  $T_n^-$  connected with the  $n$ -th non-boundary edge, as illustrated in Figure 2.3.

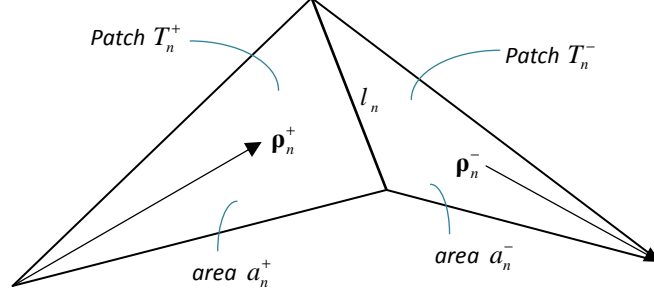


**Figure 2.3** A pair of triangular patches associated with a non-boundary edge.

In Figure 2.3,  $l_n$  is the length of the non-boundary edge (edge common to both triangles) and  $a_n^+$  and  $a_n^-$  are the areas of the triangles  $T_n^+$  and  $T_n^-$ , respectively. Vectors  $\boldsymbol{\rho}_n^+$  and  $\boldsymbol{\rho}_n^-$  are the position vectors defined with respect to the free vertices (vertices not connected to the common edge) of  $T_n^+$  and  $T_n^-$ , respectively. The position vector  $\boldsymbol{\rho}_n^+$  is oriented from the free vertex of  $T_n^+$  to any point inside the triangle. Similar remarks can be applied to the position vector  $\boldsymbol{\rho}_n^-$ , except its direction is toward the free vertex from any point in  $T_n^-$ . The plus or minus designation of the triangles is defined based on the assumption that the positive direction of the current flow is from the triangle  $T_n^+$  to  $T_n^-$ . Applying the RWG basis [2], the expansion function associated with the  $n$ -th edge is defined on the pair of adjacent triangular patches as

$$\mathbf{f}_n(\mathbf{r}) = \mathbf{f}_n^+(\mathbf{r}) + \mathbf{f}_n^-(\mathbf{r}) \quad (2.12)$$

$$\mathbf{f}_n^\pm(\mathbf{r}) = \begin{cases} \frac{l_n}{2a_n^\pm} \boldsymbol{\rho}_n^\pm, & \mathbf{r} \in T_n^\pm \\ 0, & \mathbf{r} \notin T_n^\pm \end{cases} \quad (2.13)$$

The surface divergence of the above basis function can then be calculated as follows. [2]

$$\nabla_S \cdot \mathbf{f}_n(\mathbf{r}) = \nabla_S \cdot \mathbf{f}_n^+(\mathbf{r}) + \nabla_S \cdot \mathbf{f}_n^-(\mathbf{r}) \quad (2.14)$$

$$\nabla_S \cdot \mathbf{f}_n^\pm(\mathbf{r}) = \begin{cases} \pm \frac{l_n}{a_n^\pm}, & \mathbf{r} \in T_n^\pm \\ 0, & \mathbf{r} \notin T_n^\pm \end{cases} \quad (2.15)$$

### 2.3 Temporal Basis Functions

The Hertz vector can now be expressed in terms of the RWG basis function for the spatial variable. Hence,

$$\mathbf{u}(\mathbf{r}, t) = \sum_{n=1}^N u_n(t) \mathbf{f}_n(\mathbf{r}) \quad (2.16)$$

where  $u_n(t)$  is the transient part and needs to be expanded by temporal basis function.

The associated Laguerre function set is defined by

$$\phi_j(t) = \begin{cases} e^{-t/2} L_j(t) & (t \geq 0) \\ 0 & (t < 0) \end{cases} \quad (2.17)$$

where  $L_j(t)$  is the Laguerre polynomial of order  $j$  [18][19]. Using it to represent the causal temporal basis functions, the transient variation introduced in Eq. (2.17) can be expanded as



$$u_n(t) = \sum_{j=0}^{\infty} u_{n,j} \phi_j(st) \quad (2.18)$$

where  $u_{n,j}$  are the unknown coefficients to be solved and  $s$  is a scaling factor. Controlling the factor  $s$  allows the support provided by the expansion functions to be increased or decreased. The expression of the first and second derivatives of the transient variations for the solution can be given analytically as

$$\frac{d}{dt} u_n(t) = s \sum_{j=0}^{\infty} \left( \frac{1}{2} u_{n,j} + \sum_{k=0}^{j-1} u_{n,k} \right) \phi_j(st) \quad (2.19)$$

$$\frac{d^2}{dt^2} u_n(t) = s^2 \sum_{j=0}^{\infty} \left( \frac{1}{4} u_{n,j} + \sum_{k=0}^{j-1} (j-k) u_{n,k} \right) \phi_j(st) \quad (2.20)$$

This assumes that the functions  $u_n(0) = 0$  and  $du_n(0)/dt = 0$  as the time response have not started at  $t = 0$  because of causality.

In summary, five characteristic properties of the associated Laguerre functions derived from Laguerre polynomials have been used in this new formulation:

1. *Causality*: The Laguerre polynomials are defined over  $0 \leq t < +\infty$ . Therefore, they are quite suitable to represent any natural time domain responses as they are always causal.
2. *Recursive computation*: The Laguerre polynomials of higher orders can be generated recursively using the lower orders through a stable computational process.

3. *Orthogonality*: With respect to a weighting function, the Laguerre polynomials are orthogonal to each other. One can construct a set of orthonormal basis functions, which is called the weighted Laguerre polynomials or associated Laguerre functions. Physical quantities that are functions of time can be spanned in terms of these orthonormal basis functions.
4. *Convergence*: The associated Laguerre functions decay to zero as time goes to infinity; therefore, the solution does not diverge for late times. Also, because the associated Laguerre functions form an orthonormal set, any arbitrary time function can be spanned by these basis functions and the approximation converges.
5. *Separability of the space and time variables*: Due to the additive property of the weighted Laguerre functions, the spatial and the temporal variables can be completely separated and the time variable can be completely eliminated from all the computations except the calculation of the excitation coefficient, which is determined by the excitation waveform only. This eliminates the interpolation that is necessary to estimate values of the current or the charge at time instances that do not correspond to a sampled time instance. Therefore, the values of the current can be obtained quite accurately at any time.

## **2.4 Testing of the Integral Equation**

Substituting Eqs. (2.8)–(2.20) into the TD-EFIE in Eq. (2.7) results in

$$\left( \frac{\mu s^2}{4\pi} \sum_{n=1}^N \sum_{j=0}^{\infty} \left( \frac{1}{4} u_{n,j} + \sum_{k=0}^{j-1} (j-k) u_{n,k} \right) \int_S \frac{\phi_j(s\tau) \mathbf{f}_n(\mathbf{r}')}{R} dS' \right. \\ \left. - \frac{1}{4\pi\epsilon} \sum_{n=1}^N \sum_{j=0}^{\infty} u_{n,j} \int_S \nabla \left( \frac{\phi_j(s\tau) \nabla' \cdot \mathbf{f}_n(\mathbf{r}')}{R} \right) dS' \right)_{\tan} = (\mathbf{E}^i(\mathbf{r}, t))_{\tan} \quad (2.21)$$

Next, Galerkin's method is employed to solve this integral equation. First is the temporal testing, where another temporal basis function is multiplied to both sides of Eq. (2.21) and integrated over the whole domain of  $[0, +\infty)$ , which eliminates the transient variable. One then has

$$\frac{\mu s^2}{4\pi} \sum_{n=1}^N \sum_{j=0}^{\infty} \left( \frac{1}{4} u_{n,j} + \sum_{k=0}^{j-1} (j-k) u_{n,k} \right) \int_S \frac{1}{R} I_{ij}(sR/c) \mathbf{f}_n(\mathbf{r}') dS' \\ - \frac{1}{4\pi\epsilon} \sum_{n=1}^N \sum_{j=0}^{\infty} u_{n,j} \int_S \nabla \left( \frac{1}{R} I_{ij}(sR/c) \nabla' \cdot \mathbf{f}_n(\mathbf{r}') \right) dS' = V_i(\mathbf{r}) \quad (2.22)$$

where

$$I_{ij}(sR/c) = \int_{sR/c}^{\infty} \phi_i(st) \phi_j(st - sR/c) d(st) \\ = \begin{cases} \phi_{i-j}(sR/c) - \phi_{i-j-1}(sR/c) & j < i \\ \phi_0(sR/c) & j = i \\ 0 & j > i \end{cases} \quad (2.23)$$

$$V_i(\mathbf{r}) = \int_0^{\infty} \phi_i(st) \mathbf{E}^i(\mathbf{r}, t) d(st) \quad (2.24)$$

Because of this orthogonality condition in Eq. (2.23), the upper limit of the sum in Eq. (2.22) can be changed from  $\infty$  to  $i$ . The spatial testing can then be performed with different  $\mathbf{f}_m(\mathbf{r})$  ( $m = 1, 2, \dots, N$ ). In this spatial testing, another basis function  $\mathbf{f}_m(\mathbf{r})$  is

multiplied to both sides of Eq. (2.22) and integrates the equation for the whole surface.

One obtains

$$\begin{aligned} \sum_{n=1}^N \left( \frac{\mu s^2}{4} \alpha_{mn} + \frac{1}{\varepsilon} \beta_{mn} \right) u_{n,i} = & \Omega_{mi} - \mu s^2 \sum_{n=1}^N \sum_{k=0}^{i-1} (i-k) u_{n,k} \alpha_{mn} \\ & - \mu s^2 \sum_{n=1}^N \sum_{j=0}^{i-1} \sum_{k=0}^{j-1} (j-k) u_{n,k} A_{mnij} - \sum_{n=1}^N \sum_{j=0}^{i-1} \left( \frac{\mu s^2}{4} A_{mnij} + \frac{1}{\varepsilon} B_{mnij} \right) u_{n,j} \end{aligned} \quad (2.25)$$

where

$$\alpha_{mn} = \int_S \mathbf{f}_m(\mathbf{r}) \cdot \int_{S'} \frac{e^{(-sR/(2c))}}{4\pi R} \mathbf{f}_n(\mathbf{r}') dS' dS \quad (2.26)$$

$$\beta_{mn} = \int_S \nabla \cdot \mathbf{f}_m(\mathbf{r}) \int_{S'} \frac{e^{(-sR/(2c))}}{4\pi R} \nabla' \cdot \mathbf{f}_n(\mathbf{r}') dS' dS \quad (2.27)$$

$$A_{mnij} = \int_S \mathbf{f}_m(\mathbf{r}) \cdot \int_{S'} \frac{I_{ij}(sR/c)}{4\pi R} \mathbf{f}_n(\mathbf{r}') dS' dS \quad (2.28)$$

$$B_{mnij} = \int_S \nabla \cdot \mathbf{f}_m(\mathbf{r}) \int_{S'} \frac{I_{ij}(sR/c)}{4\pi R} \nabla' \cdot \mathbf{f}_n(\mathbf{r}') dS' dS \quad (2.29)$$

$$\Omega_{m,i} = \int_S \mathbf{f}_m(\mathbf{r}) \cdot \mathbf{V}_i(\mathbf{r}) dS . \quad (2.30)$$

Finally, Eq. (2.25) can be written into a matrix equation as

$$[Z_{mi}] [u_{n,i}] = [\gamma_{m,i}] . \quad i = 1, 2, 3, \dots, I . \quad (2.31)$$

where

$$Z_{mn} = \frac{\mu s^2}{4} \alpha_{mn} + \frac{1}{\epsilon} \beta_{mn} \quad (2.32)$$

$$\begin{aligned} \gamma_{m,i} = & \Omega_{mi} - \mu s^2 \sum_{n=1}^N \sum_{k=0}^{i-1} (i-k) u_{n,k} \alpha_{mn} - \\ & \mu s^2 \sum_{n=1}^N \sum_{j=0}^{i-1} \sum_{k=0}^{j-1} (j-k) u_{n,k} A_{mnij} - \sum_{n=1}^N \sum_{j=0}^{i-1} \left( \frac{\mu s^2}{4} A_{mnij} + \frac{1}{\epsilon} B_{mnij} \right) u_{n,j} \end{aligned} \quad (2.33)$$

The matrix element  $Z_{mn}$  is not a function of the order of the temporal testing functions. Eq. (2.31) indicates that the unknown coefficient of a temporal degree  $i$  can be characterized by its lower degrees; this leads to a marching-on-in-degree algorithm. This can start from temporal degree 0 and solve Eq. (2.31) one degree at a time up to the maximum degree. Solving the matrix equation in this marching-on-in-degree manner allows the unknown coefficients  $u_{n,j}$  to be found for all the degrees. The electric current is expressed using unknown coefficients  $u_{n,j}$ .



## **Chapter 3.**

# **The Improvements of the Temporal Basis Function**

In the previous work in this field, the associated Laguerre functions were chosen as the temporal basis functions. However, this choice has a drawback; namely, that the derivative of the associated Laguerre function forms a summation over its lower degrees. Consequently, the final equations that are conventionally used contain many summations. Therefore, the use of a new basis function set, which is a combination of associated Laguerre functions, is proposed here. This new basis function set retains all the advantages of the associated Laguerre functions while its derivative now is another combination of associated Laguerre functions instead of a summation, which reduces the computation time by a factor of about 10 to 20.

In addition, in Eq. (2.23) of the previous chapter, the lower degree temporal basis functions with different retarded times were no longer orthogonal to each other. Calculation of the coefficients for each degree required integration over the previous polynomial orders to eliminate the components of the lower degree basis functions. This takes significant CPU time and results in a computationally inefficient procedure. Therefore, a new computational form of the Green's function is used to treat the retarded time component associated with the basis functions of a lower degree in order to reduce the operation count. This results in an increase in the computational efficiency over the original formulation.

In this chapter, the novel transient basis function is first described and a form of the new Green's function in the MOD method is introduced. Numerical results are then presented to show the efficiency and accuracy of the improved formulas. The improvement in efficiency gives ordinary PCs the capability to calculate transient responses from full-sized aircraft and their results are shown in this chapter.

### 3.1 New Combination of Temporal Basis Functions

In order to improve the computational efficiency, the temporal basis function is represented by a combination of three associated Laguerre functions with successive degrees multiplied by some unknown constants for the transient coefficient  $u_n(t)$ , as described in [21]

$$u_n(t) = \sum_{j=0}^{\infty} u_{n,j} \left( \phi_j(st) - 2\phi_{j+1}(st) + \phi_{j+2}(st) \right) \quad (3.1)$$

Referring to the property of the Laguerre polynomials [19], the derivative of the Laguerre polynomials can be expressed as a sum of its lower-order components as

$$\frac{d}{dt} L_j(st) = -L_{j-1}^{(1)}(st) = -\sum_{p=0}^{j-1} L_p(st) \quad (3.2)$$

From Eq. (3.2), the derivative of the associated Laguerre function is written as

$$\frac{d}{dt} \phi_j(st) = -\frac{s}{2} \phi_j(st) - s \sum_{p=0}^{j-1} \phi_p(st) \quad (3.3)$$



Using the property given by Eq. (3.3), the first and second derivatives of the transient coefficient  $u_n(t)$  of Eq. (3.1) can be derived and represented as a combination of associated Laguerre functions of different degrees by:

$$\frac{d}{dt}u_n(t) = \sum_{j=0}^{\infty} \frac{s}{2} u_{n,j} (\phi_j(st) - \phi_{j+2}(st)) \quad (3.4)$$

$$\frac{d^2}{dt^2}u_n(t) = \sum_{j=0}^{\infty} u_{n,j} \frac{s^2}{4} (\phi_j(st) + 2\phi_{j+1}(st) + \phi_{j+2}(st)) \quad (3.5)$$

In contrast to the conventional MOD method [16][17], where the transient variable is expanded by a single associated Laguerre function set  $\phi_j(st)$ , as depicted by Eq. (2.18), the new temporal basis function presented here is formed by a combination of three associated Laguerre functions,  $\phi_j(st)$ ,  $\phi_{j+1}(st)$ , and  $\phi_{j+2}(st)$ , for each degree  $j$ . The use of this combinational temporal basis function set means that the first and second derivatives of the transient variable  $u_n(t)$  expressed in Eqs. (3.4) and (3.5) contain fewer terms in the summation compared to those using the conventional MOD. This is due to cancellation of the lower-degree components in the derivatives of the three associated Laguerre functions,  $\phi_j(st)$ ,  $\phi_{j+1}(st)$ , and  $\phi_{j+2}(st)$ . This cancellation leads to fewer terms to be computed and a shorter time for the computation.

Substituting Eqs. (3.1), (3.4) and (3.5) into Eq. (2.16), the TD-EFIE are expressed by the spatial vector function  $\mathbf{f}_n(\mathbf{r})$  and the temporal function  $\phi_j(st) - 2\phi_{j+1}(st) + \phi_{j+2}(st)$  as

$$\left( \begin{aligned} & \frac{\mu}{4\pi} \int_S \sum_{n=1}^N \sum_{j=0}^{\infty} u_{n,j} \frac{1}{R} \frac{s^2}{4} (\phi_j(s\tau) + 2\phi_{j+1}(s\tau) + \phi_{j+2}(s\tau)) \mathbf{f}_n(\mathbf{r}') dS' \\ & - \frac{\nabla}{4\pi\epsilon} \int_S \sum_{n=1}^N \sum_{j=0}^{\infty} u_{n,j} \frac{1}{R} (\phi_j(s\tau) - 2\phi_{j+1}(s\tau) + \phi_{j+2}(s\tau)) \nabla' \cdot \mathbf{f}_n(\mathbf{r}') dS' \end{aligned} \right)_{\tan} = \left( \mathbf{E}^i(\mathbf{r}, t) \right)_{\tan} \quad (3.6)$$

After expanding the terms inside the summation and recombining the terms with the same degree of associated Laguerre functions, Eq. (3.6) can be rewritten by introducing two temporary parameters  $e_{n,j}$  and  $d_{n,j}$  as

$$\left( \begin{aligned} & \frac{\mu}{4\pi} \int_S \sum_{n=1}^N \sum_{j=0}^{\infty} e_{n,j} \frac{1}{R} \frac{s^2}{4} \phi_j(s\tau) \mathbf{f}_n(\mathbf{r}') dS' \\ & - \frac{\nabla}{4\pi\epsilon} \int_S \sum_{n=1}^N \sum_{j=0}^{\infty} d_{n,j} \frac{1}{R} \phi_j(s\tau) \nabla' \cdot \mathbf{f}_n(\mathbf{r}') dS' \end{aligned} \right)_{\tan} = \left( \mathbf{E}^i(\mathbf{r}, t) \right)_{\tan} \quad (3.7)$$

where

$$e_{n,j} = u_{n,j-2} + 2u_{n,j-1} + u_{n,j} \quad (3.8)$$

$$d_{n,j} = u_{n,j-2} - 2u_{n,j-1} + u_{n,j} \quad (3.9)$$

where  $u_{n,j} = 0$  is assumed for  $j < 0$ .

### 3.2 Testing Procedure and the Matrix Equation

Similar to the testing procedure described in the previous chapter, Galerkin's method is used in temporal and spatial testing. Applying the temporal testing with a testing function  $\phi_i(st)$  yields

$$\left( \begin{aligned} & \frac{\mu}{4\pi} \int_S \sum_{n=1}^N \sum_{j=0}^i e_{n,j} \frac{1}{R} \frac{s^2}{4} I_{ij}(sR/c) \mathbf{f}_n(\mathbf{r}') dS' \\ & - \frac{\nabla}{4\pi\epsilon} \int_S \sum_{n=1}^N \sum_{j=0}^i d_{n,j} \frac{1}{R} I_{ij}(sR/c) \nabla' \cdot \mathbf{f}_n(\mathbf{r}') dS' \end{aligned} \right)_{\tan} = (\mathbf{V}^i(\mathbf{r}))_{\tan} \quad (3.10)$$

where  $I_{ij}(sR/c)$  and  $\mathbf{V}^i(\mathbf{r})$  are given in Eqs. (2.23) and (2.24).

It is important to note that the basis functions contain a combination of three associated Laguerre functions, while only one is used for testing. Further, applying spatial testing to Eq. (3.10) with a testing function  $\mathbf{f}_m(\mathbf{r})$  yields

$$\begin{aligned} & \frac{\mu}{4\pi} \int_S \int_S \sum_{n=1}^N \sum_{j=0}^i e_{n,j} \frac{1}{R} \frac{s^2}{4} I_{ij}(sR/c) \mathbf{f}_m(\mathbf{r}) \cdot \mathbf{f}_n(\mathbf{r}') dS' dS \\ & - \frac{1}{4\pi\epsilon} \int_S \mathbf{f}_m(\mathbf{r}) \cdot \nabla \int_S \sum_{n=1}^N \sum_{j=0}^i d_{n,j} \frac{1}{R} I_{ij}(sR/c) \nabla' \cdot \mathbf{f}_n(\mathbf{r}') dS' dS \\ & = \int_S \mathbf{f}_m(\mathbf{r}) \cdot \mathbf{V}^i(\mathbf{r}) dS \end{aligned} \quad (3.11)$$

Equivalently, Eq. (3.11) can be written as

$$\frac{s^2 \mu}{4} \sum_{n=1}^N \sum_{j=0}^i e_{n,j} A_{mnij} + \frac{1}{\epsilon} \sum_{n=1}^N \sum_{j=0}^i d_{n,j} B_{mnij} = \Omega_{m,i} \quad (3.12)$$

where

$$A_{mnij} = \int_S \mathbf{f}_m(\mathbf{r}) \cdot \int_S \frac{1}{4\pi R} I_{ij}(sR/c) \mathbf{f}_n(\mathbf{r}') dS' dS \quad (3.13)$$

$$B_{mnij} = \int_S \nabla \cdot \mathbf{f}_m(\mathbf{r}) \int_S \frac{1}{4\pi R} I_{ij}(sR/c) \nabla' \cdot \mathbf{f}_n(\mathbf{r}') dS' dS \quad (3.14)$$

$$\Omega_{m,i} = \int_S \mathbf{f}_m(\mathbf{r}) \cdot \mathbf{V}^i(\mathbf{r}) dS \quad (3.15)$$

Using Eq. (2.23), Eqs. (3.13) and (3.14) for  $j = i$  can be written as

$$\alpha_{mn} = A_{mnij} \Big|_{j=i} = \int_S \mathbf{f}_m(\mathbf{r}) \cdot \int_S \frac{1}{4\pi R} e^{(-sR/(2c))} \mathbf{f}_n(\mathbf{r}') dS' dS \quad (3.16)$$

$$\beta_{mn} = B_{mnij} \Big|_{j=i} = \int_S \nabla \cdot \mathbf{f}_m(\mathbf{r}) \int_S \frac{1}{4\pi R} e^{(-sR/(2c))} \nabla' \cdot \mathbf{f}_n(\mathbf{r}') dS' dS \quad (3.17)$$

Finally, transforming the variables  $e_{n,i}$  and  $d_{n,i}$  back into  $u_{n,i}$  according to Eq. (3.8) and (3.9), and moving the terms associated with  $u_{n,i}$  of degrees smaller than  $i$  to the right-hand side, yields

$$\begin{aligned} \sum_{n=1}^N u_{n,i} \left( \frac{s^2 \mu}{4} \alpha_{mn} + \frac{1}{\varepsilon} \beta_{mn} \right) &= \Omega_{m,i} - \frac{s^2 \mu}{4} \sum_{n=1}^N (u_{n,i-2} + 2u_{n,i-1}) \alpha_{mn} \\ &\quad - \frac{1}{\varepsilon} \sum_{n=1}^N (u_{n,i-2} - 2u_{n,i-1}) \beta_{mn} - \frac{s^2 \mu}{4} \sum_{n=1}^N \sum_{j=0}^{i-1} (u_{n,j-2} + 2u_{n,j-1} + u_{n,j}) A_{mnij} \\ &\quad - \frac{1}{\varepsilon} \sum_{n=1}^N \sum_{j=0}^{i-1} (u_{n,j-2} - 2u_{n,j-1} + u_{n,j}) B_{mnij} \end{aligned} \quad (3.18)$$

If the unknown coefficients  $u_{n,j}$  lower than degree  $i$  are known, then the coefficients  $u_{n,i}$  of degree  $i$  can be solved by Eq. (3.18) in a marching-on-in-degree manner.

### 3.3 Property of Green's Function Terms

Note that the term  $I_{ij}(sR/c)/R$ , which is the Green's function after testing, exists in all the calculations of  $A_{mnij}$  and  $B_{mnij}$ . In Eq. (3.13) and (3.14), the associated Laguerre functions are not orthogonal, due to the involvement of the retarded time factor; therefore, the computations cannot be simplified using the orthogonality between the functions. This

results in a need for a much longer CPU time to complete the computation of the Green's function. Therefore, a new Green's function is designed that groups the retarded-time terms, in order to minimize the repetitive computations for the Laguerre polynomials of different degrees and the floating-point number divisions for  $R$ . Defining the two parameters  $k_{mni}$  and  $h_{mni}$  associated with the new Green's functions as

$$\begin{aligned}
k_{mni} &= (u_{n,i-2} + 2u_{n,i-1})\alpha_{mn} + \sum_{j=0}^{i-1} (u_{n,j-2} + 2u_{n,j-1} + u_{n,j})A_{mnij} \\
&= \int_S \mathbf{f}_m(\mathbf{r}) \cdot \int_S \mathbf{f}_n(\mathbf{r}') \frac{1}{4\pi R} \left( (u_{n,i-2} + 2u_{n,i-1})I_{ii}(sR/c) \right. \\
&\quad \left. + \sum_{j=0}^{i-1} (u_{n,j-2} + 2u_{n,j-1} + u_{n,j})I_{ij}(sR/c) \right) dS'dS
\end{aligned} \tag{3.19}$$

and

$$\begin{aligned}
h_{mni} &= (u_{n,i-2} - 2u_{n,i-1})\beta_{mn} + \sum_{j=0}^{i-1} (u_{n,j-2} - 2u_{n,j-1} + u_{n,j})B_{mnij} \\
&= \int_S \nabla \cdot \mathbf{f}_m(\mathbf{r}) \int_S \nabla' \cdot \mathbf{f}_n(\mathbf{r}') \frac{1}{4\pi R} \left( (u_{n,i-2} - 2u_{n,i-1})I_{ii}(sR/c) \right. \\
&\quad \left. + \sum_{j=0}^{i-1} (u_{n,j-2} - 2u_{n,j-1} + u_{n,j})I_{ij}(sR/c) \right) dS'dS
\end{aligned} \tag{3.20}$$

Eq. (3.18) can be expressed as

$$\sum_{n=1}^N u_{n,i} \left( \frac{s^2 \mu}{4} \alpha_{mn} + \frac{1}{\varepsilon} \beta_{mn} \right) = \Omega_{m,i} - \frac{s^2 \mu}{4} \sum_{n=1}^N k_{mni} - \frac{1}{\varepsilon} \sum_{n=1}^N h_{mni} \tag{3.21}$$

where  $m = 1, 2, \dots, N$  and  $i = 0, 1, 2, \dots, I$ . This can further be represented in a matrix form as

$$[Z_{mn}]_{N \times N} [u_{n,i}]_{N \times 1} = [\gamma_{m,i}]_{N \times 1} \quad (3.22)$$

where

$$Z_{mn} = \frac{s^2 \mu}{4} \alpha_{mn} + \frac{1}{\varepsilon} \beta_{mn} \quad (3.23)$$

$$\gamma_{m,i} = \Omega_{m,i} - \frac{s^2 \mu}{4} \sum_{n=1}^N k_{mni} - \frac{1}{\varepsilon} \sum_{n=1}^N h_{mni} \quad (3.24)$$

For any temporal degree  $i_0$ , the coefficients  $u_{n,i_0}$  can be computed by a MOD procedure using Eq. (8.23), providing that all the lower-degree coefficients for  $i = 0, 1, 2, \dots, i_0 - 1$  have already been computed. Using the computational scheme outlined, the computation time can be significantly reduced by a factor of more than ten for most applications, when contrasted against the use of the conventional MOD.

### 3.4 Improvement of the Computation Time

The improvement of the computation time for solving the TD-EFIE with the new MOD scheme outlined in this chapter can be quantized by approximating the computational efficiency in terms of the order of magnitude  $\mathcal{O}$  (called big  $O$  notation) of the total number of operations, which mainly depends upon the maximum number of spatial unknowns  $N$  and the maximum temporal degree  $I$ . The TD-EFIE formulations given by Eq. (2.31) and Eq. (3.22) allow determination of the number of operations needed for the floating-point divisions and the calculations of the Laguerre polynomials using the conventional MOD and the new MOD, as listed in Table 3.1.

**Table 3.1.** The number of operations for the conventional and the new MOD methods

	The conventional MOD in Eq. (2.31)	The new MOD in Eq. (3.22)
Floating point divisions	$\mathcal{O}(N^2I^2)$	$\mathcal{O}(N^2I)$
Laguerre polynomial computations	$\mathcal{O}(N^2I^3)$	$\mathcal{O}(N^2I^2)$

These two computation tasks are the most time-consuming in the MOD solution procedures because the number of floating-point divisions involves many instruction cycles and the calculation of the Laguerre polynomials requires a recursive algorithm. Table 3.1 also shows that the a relatively smaller number of operations is needed for these two computation tasks in the new MOD when compared to the conventional MOD. This achieves a significant reduction in time for solving the TD-EFIE. The improvement in the efficiency of the new MOD is better illustrated by numerical examples in this chapter that compare the computation time for these two MOD methods.

### 3.5 Solution for the Unperfected Metal Surface

The objective of this chapter is to present a solution methodology for the analysis of arbitrary frequency dependent losses on conducting structures in a time domain electric field integral equation. An implementing method is proposed whereby the convolution between these two functional variations — namely the loss factor and the current density — can be treated in an analytical fashion, resulting in an accurate and efficient solution methodology.

The parameters of the loads, such as resistors, inductors, capacitors, or skin effects are usually specified in the frequency domain. Therefore, if one transforms this

functional variation into time domain, this results in a convolution between these temporal functional variations of the loads with the transient current densities on the structures. In this section, both of these temporal variations are expanded in terms of the associated Laguerre functions. Hence, in this situation, this convolution can be analytically performed in an efficient and accurate way, thereby simplifying the calculation.

The concentrated or distributed loads applied to conducting structures are often described in the frequency domain as a function of frequency, by  $Z(\omega)$ . Therefore, when transferred into the time domain, this represents a temporal response characterized by  $Z(t)$ . On the surface of the objects, the boundary conditions related to the tangential components of the electric fields are given by

$$\left(\mathbf{E}^i(\mathbf{r},t)\right)_{\tan} + \left(-\frac{\partial}{\partial t}\mathbf{A}(\mathbf{r},t) - \nabla\Phi(\mathbf{r},t)\right)_{\tan} = Z(\mathbf{r},t) * \mathbf{J}(\mathbf{r},t) \quad (3.25)$$

where  $*$  denotes the convolution,  $\mathbf{A}(\mathbf{r},t)$  and  $\Phi(\mathbf{r},t)$  are the magnetic vector and the electric scalar potentials, respectively.  $\mathbf{E}^i(\mathbf{r},t)$  is the incident wave. The subscript *tan* implies the tangential components. Furthermore,  $\mathbf{A}(\mathbf{r},t)$  and  $\Phi(\mathbf{r},t)$  can be expressed in terms of the current density  $\mathbf{J}$  and the charge density  $\rho$ , as indicated in previous chapter in Eq. (2.3) and (2.4), and can be further expressed in one Hertz potential, as in Eq. (2.5) and (2.6).

The time varying loads are also expanded by the associated Laguerre polynomials as



$$Z(\mathbf{r}, t) = \sum_{k=0}^{\infty} Z_k(\mathbf{r}) \phi_k(st) \quad (3.26)$$

where

$$Z_k(\mathbf{r}) = \int_0^{\infty} Z(\mathbf{r}, t) \phi_k(st) dt \quad (3.27)$$

By applying the same expansion procedure as introduced in Section 3.1, the TD-EFIE is then expressed in terms of these basis functions as

$$\begin{aligned} & \left( \frac{\mu}{4\pi} \int_S \sum_{n=1}^N \sum_{j=0}^{\infty} u_{n,j} \frac{1}{R} \frac{s^2}{4} (\phi_j(s\tau) + 2\phi_{j+1}(s\tau) + \phi_{j+2}(s\tau)) \mathbf{f}_n(\mathbf{r}') dS' \right. \\ & \left. - \frac{\nabla}{4\pi\epsilon} \int_S \sum_{n=1}^N \sum_{j=0}^{\infty} u_{n,j} \frac{1}{R} (\phi_j(s\tau) - 2\phi_{j+1}(s\tau) + \phi_{j+2}(s\tau)) \nabla' \cdot \mathbf{f}_n(\mathbf{r}') dS' \right)_{\tan} \\ & + \sum_{k=0}^{\infty} Z_k(\mathbf{r}) \phi_k(st) * \sum_{n=1}^N \sum_{j=0}^{\infty} c_{n,j} \frac{s}{2} (\phi_j(st) - \phi_{j+2}(st)) \mathbf{f}_n(\mathbf{r}) = \left( \mathbf{E}^i(\mathbf{r}, t) \right)_{\tan} \end{aligned} \quad (3.28)$$

This equation is almost the same as Eq. (3.6), except for the additional term for the loads. In Eq. (3.28), a convolution must be performed between two associated Laguerre functions. This can be analytically calculated as [18].

$$\begin{aligned} \phi_k(st) * \phi_j(st) &= \int_0^t e^{-\frac{s\tau}{2}} L_k(s\tau) e^{-\frac{st-s\tau}{2}} L_j(st-s\tau) d\tau \\ &= e^{-\frac{st}{2}} \int_0^{st} L_k(s\tau) L_j(st-s\tau) d(s\tau) \\ &= e^{-\frac{st}{2}} [L_{k+j}(st) - L_{k+j+1}(st)] \end{aligned} \quad (3.29)$$

The temporal testing is applied first and then the spatial testing. As in Section 3.2, multiplying with the testing function  $\phi_i(st)$  to Eq. (3.29) and then integrating over the domain  $[0, +\infty)$  yields

$$\begin{aligned} & \left( \frac{\mu}{4\pi} \int_S \sum_{n=1}^N \sum_{j=0}^i (u_{n,j-2} + 2u_{n,j-1} + u_{n,j}) \frac{1}{R} \frac{s^2}{4} I_{ij}(sR/c) \mathbf{f}_n(\mathbf{r}') dS' - \right. \\ & \left. \frac{\nabla}{4\pi\mathcal{E}} \int_S \sum_{n=1}^N \sum_{j=0}^i (u_{n,j-2} - 2u_{n,j-1} + u_{n,j}) \frac{1}{R} I_{ij}(sR/c) \nabla' \cdot \mathbf{f}_n(\mathbf{r}') dS' \right)_{\tan} \quad (3.30) \\ & + \frac{s}{2} \sum_{n=1}^N \sum_{j=0}^i \mathbf{f}_n(\mathbf{r}) u_{n,j} \begin{pmatrix} Z_{i-j}(\mathbf{r}) - Z_{i-j-1}(\mathbf{r}) - \\ Z_{i-j-2}(\mathbf{r}) + Z_{i-j-3}(\mathbf{r}) \end{pmatrix} = \left( \mathbf{V}^i(\mathbf{r}) \right)_{\tan} \end{aligned}$$

where  $\mathbf{V}^i(\mathbf{r})$  and  $I_{ij}(sR/c)$  are same as previously defined in Eq. (2.23) and (2.24).

Furthermore, application of a spatial testing to Eq. (3.30) with the testing function  $\mathbf{f}_m(\mathbf{r})$  and then integrating it over the surface  $S$  yields

$$\begin{aligned} & \frac{s^2 \mu}{4} \sum_{n=1}^N \sum_{j=0}^i (u_{n,j-2} + 2u_{n,j-1} + u_{n,j}) A_{mnij} + \frac{1}{\mathcal{E}} \sum_{n=1}^N \sum_{j=0}^i (u_{n,j-2} - 2u_{n,j-1} + u_{n,j}) B_{mnij} \\ & + \frac{s}{2} \sum_{n=1}^N \sum_{j=0}^i u_{n,j} \begin{pmatrix} Z_{mn,i-j} - Z_{mn,i-j-1} - \\ Z_{mn,i-j-2} + Z_{mn,i-j-3} \end{pmatrix} = \Omega_{m,i} \quad (3.31) \end{aligned}$$

where  $A_{mnij}$ ,  $B_{mnij}$ ,  $\Omega_{m,i}$  are defined in Eq. (2.28) – (2.30), and

$$Z_{mnk} = \int_S Z_k(\mathbf{r}) \mathbf{f}_m(\mathbf{r}) \cdot \mathbf{f}_n(\mathbf{r}) dS \quad (3.32)$$

Finally, the above equations are written in a form that is now amenable to the MOD method by moving all the terms associated with  $u_{n,i}$  to the left hand side and the terms associated with  $u_{n,j}$  ( $j < i$ ) to the right side of Eq. (3.32). Once the coefficients  $u_{n,j}$

( $j=0,1,2,\dots,i-1$ ) are evaluated, the unknown coefficient of the next degree  $u_{n,i}$  can easily be accomplished as

$$\begin{aligned}
& \sum_{n=1}^N c_{n,i} \left( \frac{s^2 \mu}{4} A_{mn00} + \frac{1}{\epsilon} B_{mn00} + \frac{s}{2} Z_{mn,0} \right) = \\
& \Omega_{m,i} - \frac{s^2 \mu}{4} \sum_{n=1}^N (c_{n,i-2} + 2c_{n,i-1}) A_{mn00} - \frac{1}{\epsilon} \sum_{n=1}^N (c_{n,i-2} - 2c_{n,i-1}) B_{mn00} \\
& - \frac{s^2 \mu}{4} \sum_{n=1}^N \sum_{j=0}^{i-1} (c_{n,j-2} + 2c_{n,j-1} + c_{n,j}) A_{mnij} - \frac{1}{\epsilon} \sum_{n=1}^N \sum_{j=0}^{i-1} (c_{n,j-2} - 2c_{n,j-1} + c_{n,j}) B_{mnij} \\
& - \frac{s}{2} \sum_{n=1}^N \sum_{j=0}^{i-1} c_{n,j} \begin{pmatrix} Z_{mn,i-j} - Z_{mn,i-j-1} - \\ Z_{mn,i-j-2} + Z_{mn,i-j-3} \end{pmatrix}
\end{aligned} \tag{3.33}$$

Not surprisingly, Eq. (3.33) is the same as Eq. (3.18), which is the perfect conductor case, except for two terms of loads. When the loads are zero, Eq. (3.33) changes back to Eq. (3.18). This equation can apply the same marching-on-in-degree technique and all the other improvements.

### 3.6 Numerical Examples for the Improved Time Domain MoM

In this section, some numerical examples are presented to illustrate the methods introduced in the previous sections. The results obtained in the time-domain are then compared with the IDFT of the frequency domain solutions to validate the accuracy. In addition, the results are also compared with the MOT method to assess the performance of these numerical methods in terms of accuracy, stability, and computational efficiency. The comparisons are made realistic by using the same surface mesh for the MOD approach, the frequency-domain method, and the MOT methods for the analysis of the conducting and dielectric structures.

### 3.6.1 Use of Various Excitation Sources

Two types of transient plane waves used to illuminate the scatterers are presented in this chapter: the Gaussian pulse and  $T$ -pulse. The temporal electric field shaped by a Gaussian pulse is given by

$$\mathbf{E}^i(\mathbf{r}, t) = \mathbf{E}_0 \frac{4}{\sqrt{\pi T}} e^{-\gamma^2} \quad (3.34)$$

where

$$\gamma = \frac{4}{T} (ct - ct_0 - \mathbf{r} \cdot \hat{\mathbf{k}}) \quad (3.35)$$

The parameter  $\hat{\mathbf{k}}$  is the unit vector along the direction of wave propagation,  $T$  is the pulse width of the Gaussian pulse, and  $t_0$  is the time delay, which represents the time from the origin at which the pulse reaches its peak.

The  $T$ -pulse is a discrete time signal, with most of its prescribed energy focused in a given bandwidth [22][23]. It is a strictly time-limited pulse with the added stipulation that 99% of its signal energy is concentrated in a narrow band. Hence, effectively, the pulse is also approximately band limited. In addition, the pulse can be designed to be orthogonal with its shifted version as well and can have a zero DC bias if required. By interpolating this discrete pulse, a continuous pulse can be generated while its bandwidth remains approximately the same. The mathematical generation of a  $T$ -pulse is described in [24][25]. Figure 3.1 shows the transient and frequency responses of a  $T$ -pulse that is 6 light-meters (lm) in duration. Most of its energy is concentrated in the band from 0–200 MHz and only less than 0.008% of the energy is out of this band; therefore, this time

limited pulse is also practically band limited and thus is very convenient for system applications.

Next, responses of the system to these pulses are discussed.

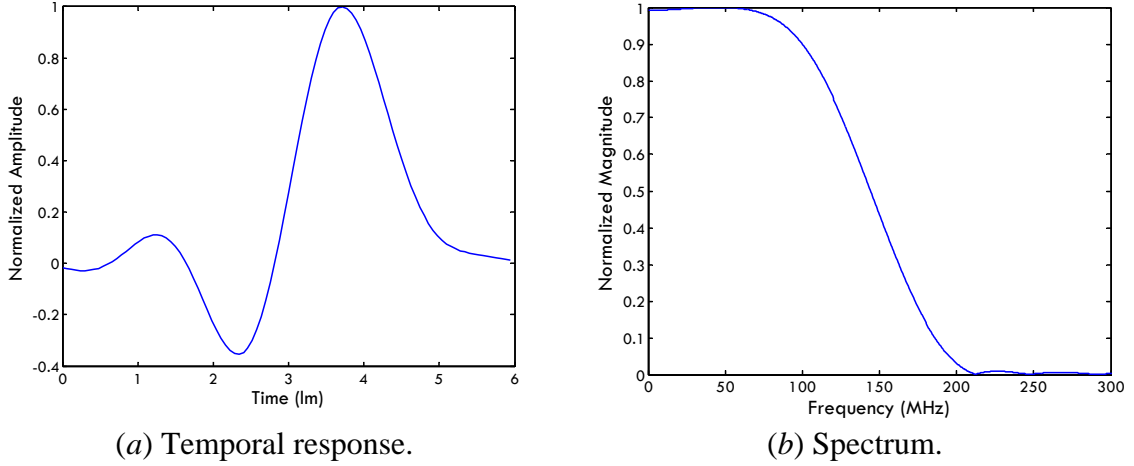


**Figure 3.1** The T-pulse.

### 3.6.2 Improved Performance in Accuracy and Stability

#### Example 3-1: A Pair of Conducting Plates

The first example deals with a pair of  $1\text{m} \times 1\text{m}$  perfectly conducting (PEC) plates forming a narrow angle ( $5^\circ$ ), as shown in Figure 3.2. The objective is to demonstrate that the shortcomings of the conventional MOD in [15] in accuracy and stability are alleviated in this new MOD formulation. The surfaces of the two plates are discretized into triangular patches, as shown in Figure 3.2. There are 274 patches and 435 edges. Some of the patches along the connected edge of the two metal plates are in very close proximity to each other; this results in strong coupling between them. Hence, a highly accurate computation is required for the spatial integrals over the patches.

The incident wave is a  $\theta$ -polarized Gaussian wave arriving from  $\phi = 0^\circ$  and  $\theta = 0^\circ$  with a pulse width of 8 lm and delayed by 12 lm. Here, 1 lm is 3.33 nanoseconds. The wave has an approximate bandwidth of 120 MHz. The induced current on this conducting structure is calculated by the frequency-domain MoM, the new MOD, and the conventional MOD method in [15]. The current across the edge connecting the nodes (0, 0, 0) and (0.0375, 0, 0) are plotted in Figure 3.3, with the three plots marked as IDFT, Improved MOD, and conventional MOD, respectively. The conventional MOD in Figure 3.3 is obviously completely unstable, whereas the new improved MOD method is stable and its results agree with the IDFT of the frequency-domain solution.

When the conventional MOD method in [15] is used to analyze this structure, the spatial integrals over the patch are tested at the center of the patch only. This leads to an error, which may result in an unstable solution. By first employing the temporal testing followed by the spatial testing, the retarded time terms can be handled analytically in the new MOD scheme, as opposed to the conventional one. This example illustrates that the approximations used in the conventional MOD may lead to the failure of the method for some types of scatterers. However, this shortcoming can be eliminated by using the new MOD methodology.

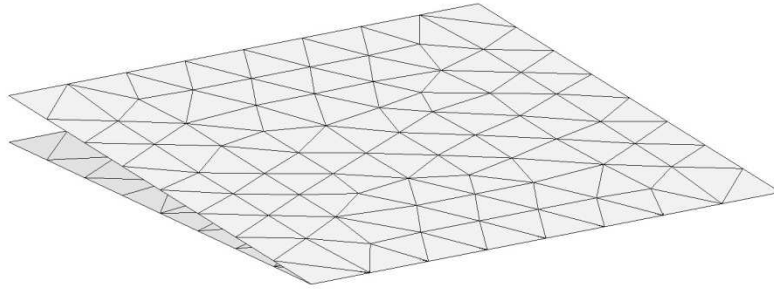


**Figure 3.2** Triangular patch model for a pair of  $0.6 \text{ m} \times 0.6 \text{ m}$  conducting plates connected at an angle of  $5^\circ$ .

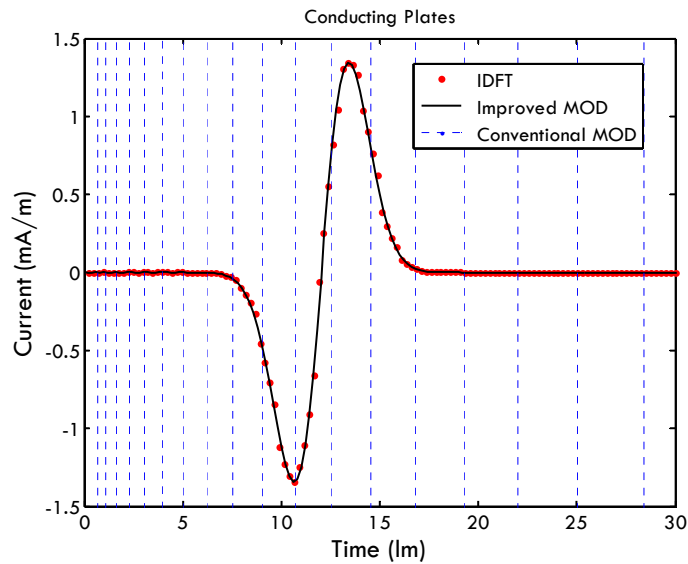


**Figure 3.3** Current on the conducting plates computed by the improved MOD method plotted against the results from the conventional MOD and the IDFT of the frequency-domain MoM solution.

### 3.6.3 Improvement in Computational Efficiency of the New MOD Method

The utilization of a combination of associated Laguerre functions as temporal basis functions, as well as the introduction of a new mathematical form of the Green's functions, leads to a simplified formulation in the new MOD method. This also

significantly reduces the computation time by at least a factor of *ten*, thereby making this new method as competitive as the MOT algorithm. These claims are illustrated through some examples.

#### Example 3-2: A Dipole

Consider a 1 meter long dipole placed along the  $x$ -axis and illuminated by a  $T$ -pulse of width 6 ns, starting at 8 ns. The pulse has an approximate bandwidth of 200 MHz. It is incident from the  $z$ -axis and is polarized along the  $x$ -axis. Figure 3.4 plots the current at the central point of the dipole, calculated using the conventional MOD, the new MOD described in Chapter 8, and the IDFT of the frequency-domain solution. The highest temporal order of the Laguerre polynomial selected is 50 in the two MOD calculations. The computation time needed for all the time-domain methods are listed in Table 3.2. Figure 3.4 shows that the results of the conventional MOD and the new MOD completely overlap, and they agree well with the IDFT of the frequency-domain solution. However, the computation time for the new MOD method over the conventional one is less by a factor of eighteen (46.3s as opposed to 2.45s). Figure 3.4 also shows that the conventional MOT method becomes unstable at a late time (after 15 ns), although it takes the least amount of computation time.



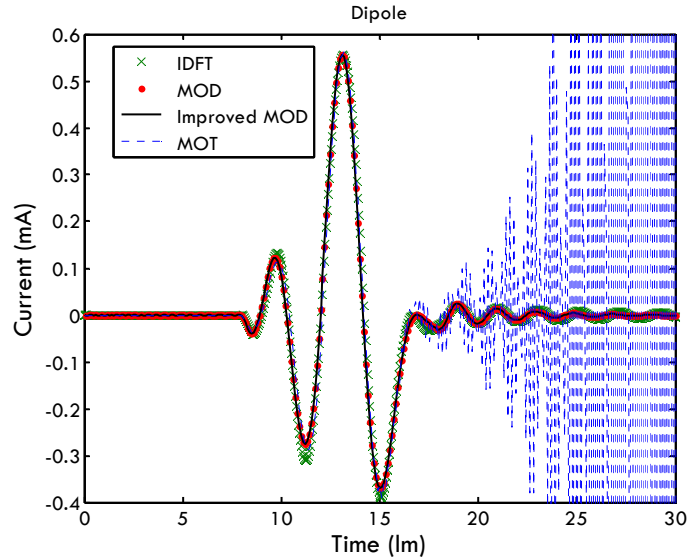


**Figure 3.4** Transient response at the central point of the dipole due to an incident  $T$ -pulse.

**Table 3.2** Comparison of the computation time for the analysis of the dipole using different time-domain methods

Methods	Total Calculation Time (s)
The conventional MOD	46.30
The new MOD	2.45
The MOT	2.04

Example 3-3: A Helix

Next, consider the analysis of a helix with a height of 8.8 meters and a radius of 2 meters, which contains 100 spatial unknowns. Its axis is oriented along the  $z$ -axis. A plane wave consisting of a  $\theta$ -polarized  $T$ -pulse is incident from  $\phi = 0^\circ$  and  $\theta = 0^\circ$ . The  $T$ -pulse has a pulse width of 6 lm and starts at 8 lm. It has a bandwidth of 200 MHz. The transient current near the end of the structure is computed using the improved MOD method. This is plotted in Figure 3.5, along with the results from the IDFT of a frequency

domain MoM solution, the conventional MOD, and the MOT techniques. The computational time required by all the methods is listed in Table 3.3 for comparison. Figure 3.5 shows a very good agreement between the solutions obtained by the conventional MOD, the new MOD, and the IDFT of the frequency-domain solution. The computational time required by the conventional MOD is twenty-two times greater than that of the new MOD (326.2s and 14.23s, respectively). The MOT can solve the problem much faster, but its result starts oscillating at an early time, as shown in Figure 3.5.

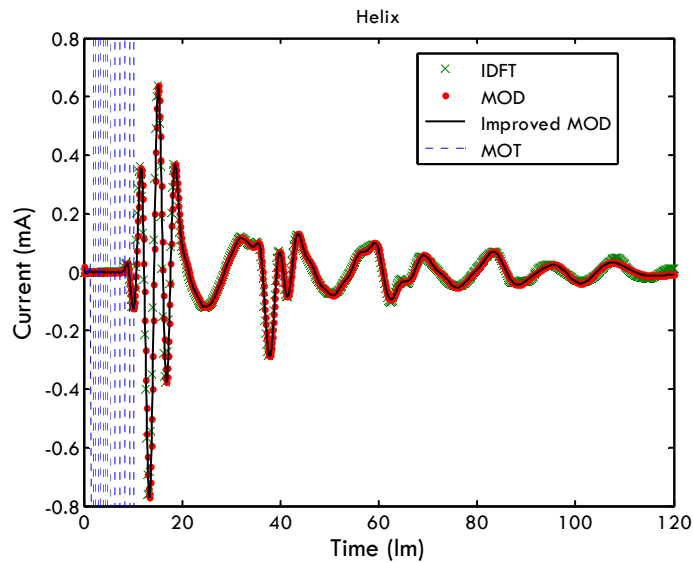


**Figure 3.5** Transient response at a point near the end of the Helix due to an incident  $T$ -pulse.

**Table 3.3** Comparison of computation time for the analysis of the helix using different time-domain methods

Methods	Total Calculation Time (min)
The conventional MOD	326.20
The new MOD	14.23
The MOT	6.66

Example 3-4: A Loop Antenna

A loop antenna with a diameter of 0.5 meter is placed in the  $xoy$  plane. A  $y$ -polarized  $T$ -pulse of duration 10 ns and delayed by 8 ns is incident from the  $x$ -axis. It has a bandwidth of 120 MHz. The highest temporal order of the Laguerre polynomials used is 100. In this example, the solution obtained by the conventional and the improved MOD are transformed into the frequency domain, and compared with the frequency-domain MoM solution. Figure 3.6 plots the currents on the loop at a point (0.25, 0, 0) m in the frequency domain. The results from the two MOD methods agree very well, along with the frequency domain MoM solution, in both magnitude and phase. The computation time to obtain the time-domain solutions using the two MOD and the MOT methods are listed in Table 3.4. A much shorter computation time, by a factor of 25, is required for the improved MOD than for the conventional MOD method. For this structure, the new MOD technique is faster than the MOT method, whose results are not shown because they are highly oscillatory.

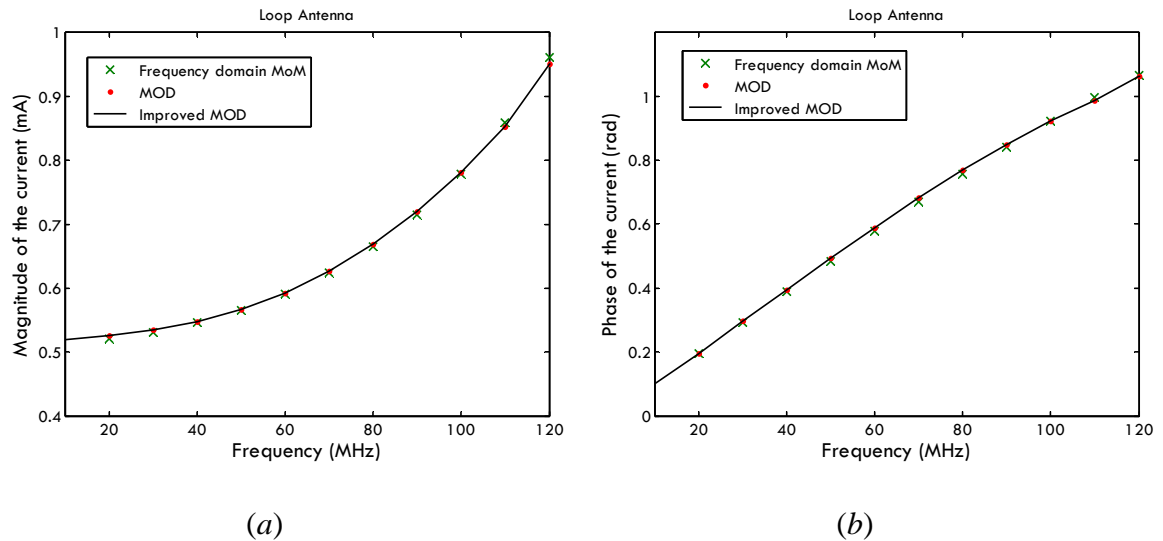


**Figure 3.6** Current response in the frequency domain at a point on the loop antenna illuminated by a  $T$ -Pulse. (a) Magnitude. (b) Phase.

**Table 3.4 Comparison of computation time for the analysis of the loop antenna using different time-domain methods**

<b>Methods</b>	<b>Total Calculation Time (s)</b>
The conventional MOD	155.56
The new MOD	6.20
The MOT	6.90

In summary, the analysis of the four wire structures discussed so far reveals that the computed results using the new MOD method are not only accurate and stable, but the computation time has been reduced at least by an order of magnitude over the conventional MOD method.

### **3.6.4 The Examples of Large Objects**

In this section, results of scattering from various shapes and sizes of conducting structures with relatively large sizes are presented to demonstrate the improved performance of this new time domain MOD algorithm. Example 3-5 is a simple sphere with a large number of meshes. Comparing it to the frequency domain results will illustrate the accuracy of the MOD method. The next two examples are a sedan and a plane, which show that the MOD can be used for arbitrary objects with a large number of unknowns.

Example 3-5: A sphere with 1 meter radius

A sphere with 1 m radius is illuminated by a  $\theta$ -polarized incident T-pulse plane wave. The back scattered wave is computed and the result is compared to the result of a commercial frequency domain MoM solver HOBBIES. I tested two T-pulse waves, one with a bandwidth of 200MHz, as shown in Figure 3.1. The other has a bandwidth of 400MHz, by scaling the T-pulse in time domain. The 200MHz pulse results in a mesh

with 14738 triangular patches and a number of unknowns of 22107. The 400MHz pulse results in a mesh with 39810 triangular patches and a number of unknowns of 59715. The  $\theta$ -component of the back scattered wave is plotted in Figure 3.7 and Figure 3.8 along with comparisons with the HOBBIES results. These plots show that the MOD results agree well with the frequency domain results for a large number of unknowns.

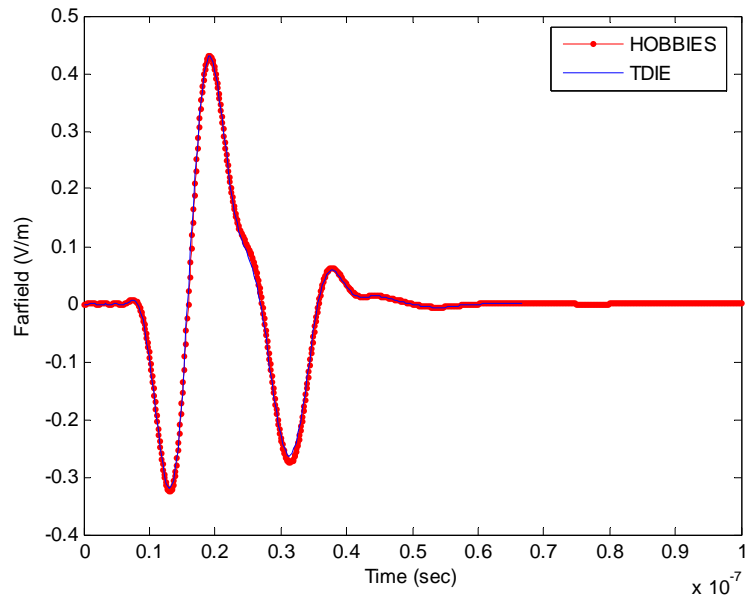


**Figure 3.7** The  $\theta$ -component of the back scattered wave from a 1m-radiused sphere with an incident pulse of 200MHz.

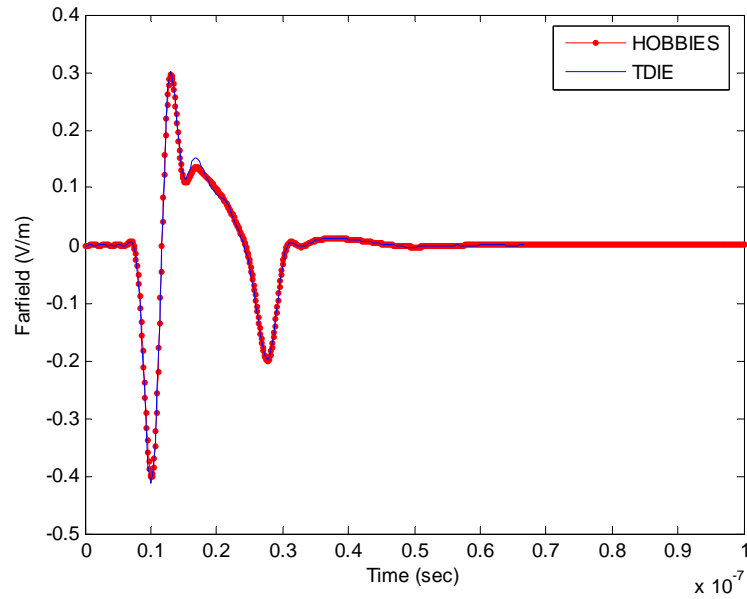


**Figure 3.8** The  $\theta$ -component of the back scattered wave from a 1m-radius sphere with an incident pulse of 400MHz.

#### Example 3-6: A sedan

The scattering from a conducting sedan with size of  $5 \text{ m} \times 1.8 \text{ m} \times 1.8 \text{ m}$  is shown Figure 3.9. A total of 15262 patches and 22893 edges are used for the triangular patch model of this structure. It also has a small dipole with two piecewise sections on top of the sedan. The transient current is computed on the vehicle when the sedan is illuminated by a  $\theta$ -polarized 200MHz-bandwithed T-pulse, as shown in Figure 3.1, incident head on from  $\phi = 0^\circ$  and  $\theta = 90^\circ$ . The transient current computed by the improved MOD method is plotted in Figure 3.10. The current moves from the head to the tail of the vehicle, as expected.

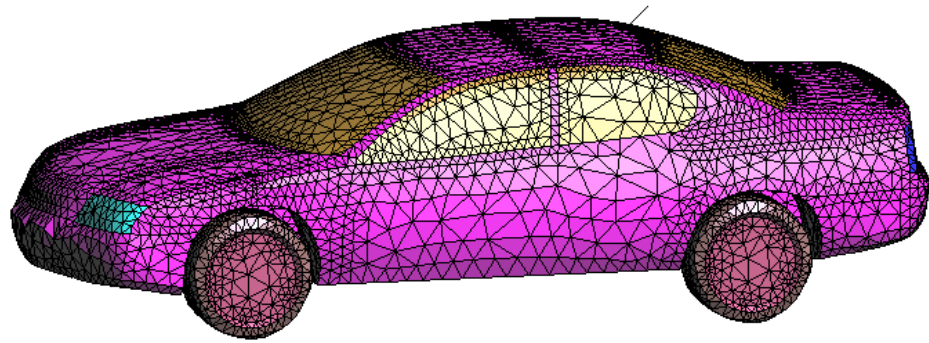
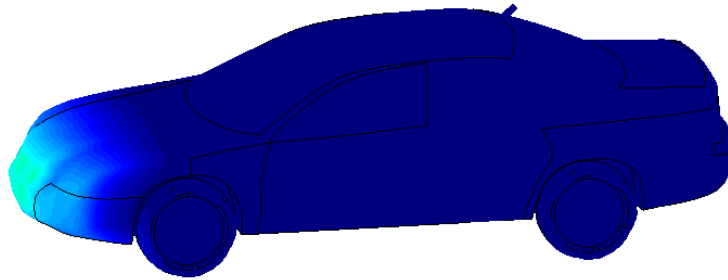
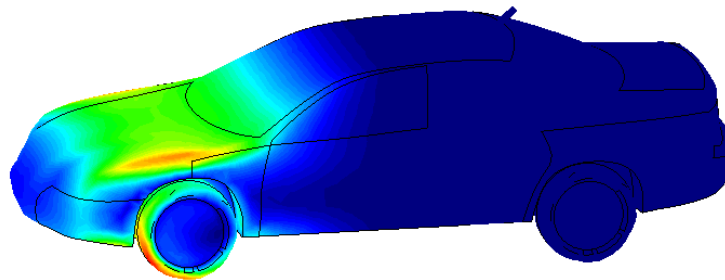


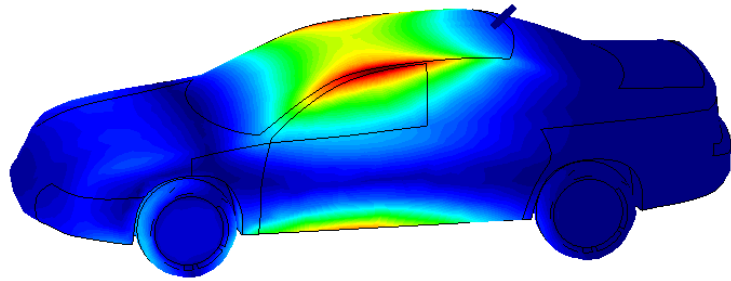
**Figure 3.9** A sedan with triangular mesh.



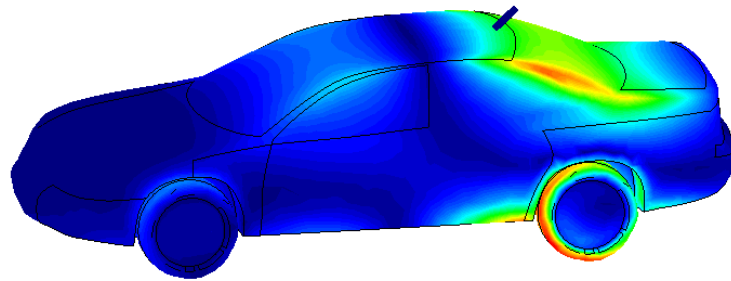
(a)  $t = 4.5 \text{ lm}$



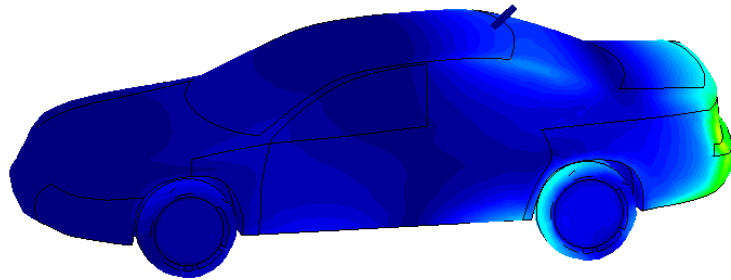
(b)  $t = 6 \text{ lm}$



(c)  $t = 7.5$  lm

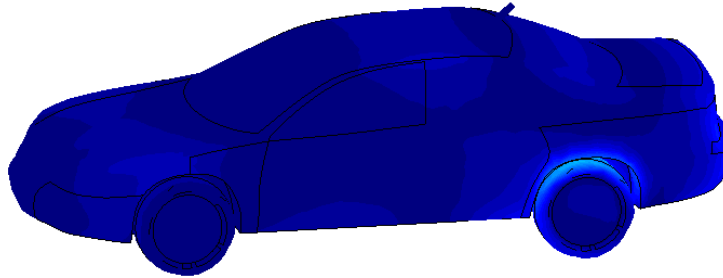


(d)  $t = 9$  lm



(e)  $t = 10.5$  lm





(f)  $t = 12 \text{ lm}$

**Figure 3.10** The current distribution at different time steps.

#### Example 3-7: A plane

In this section, a Boeing-737 aircraft with a size of  $26 \text{ m} \times 26 \text{ m} \times 11 \text{ m}$  is analyzed. The surface is discretized using 4721 triangular patches with 7327 edges, as shown in Figure 3.11. The structure is excited by a  $T$ -pulse coming from the head of the plane ( $\theta=90^\circ$  and  $\phi=0^\circ$ ). The pulse has a pulse-width of  $25 \text{ lm}$ , a time delay of  $t_0 = 17.5 \text{ lm}$ , and a bandwidth of  $50 \text{ MHz}$ . The transient current distribution on the structure from  $t = 30 \text{ lm}$  to  $t = 100 \text{ lm}$  is computed using the new MOD method and is plotted in Figure 3.12. The values of the current for all time instants have been scaled. The darkest (blue) color is defined as  $0 \text{ mA/m}$ , whereas the lightest (red) color is used for all currents larger than  $0.3 \text{ mA/m}$ .

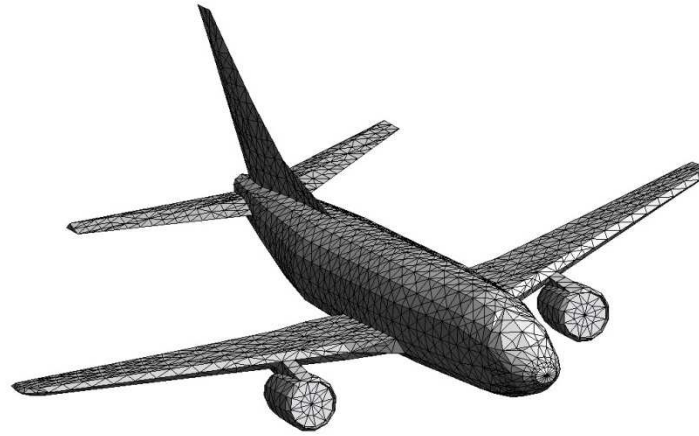
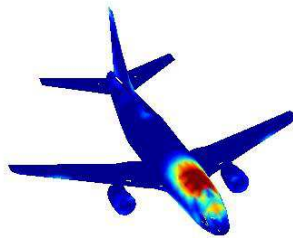
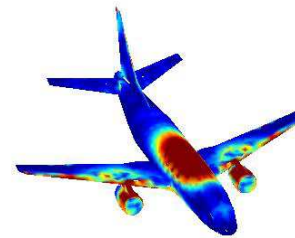


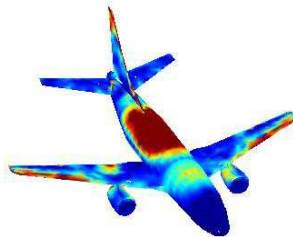
**Figure 3.11** Triangular patch model for a Boeing-737 Aircraft with a size of  $26\text{ m} \times 26\text{ m} \times 11\text{ m}$ .



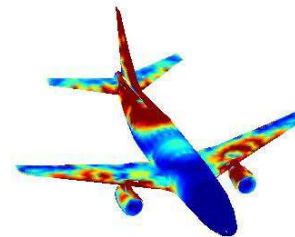
(a)  $t=30\text{ lm}$



(b)  $t=35\text{ lm}$



(c)  $t=40\text{ lm}$



(d)  $t=45\text{ lm}$

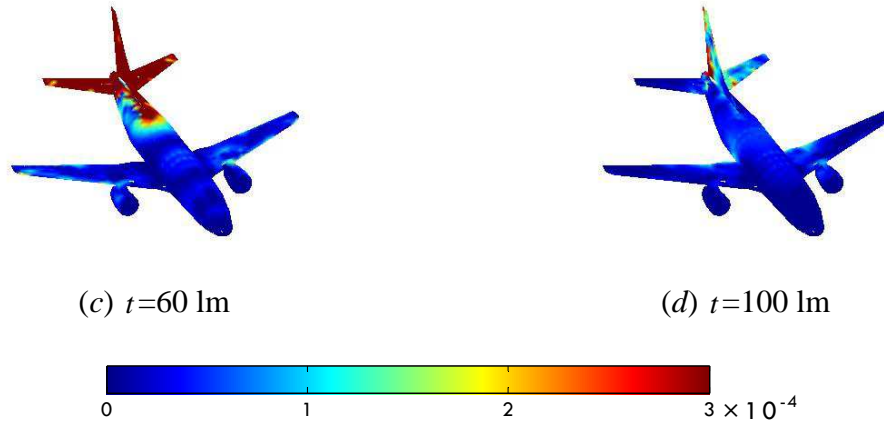


**Figure 3.12** Transient current distributions on the Boeing-737 aircraft.

From these examples, the MOD method proposed in in this chapter can be seen to speed up the computations by a factor of more than 10. The method retains all the advantages of the conventional MOD method, while the calculation time is significantly reduced. The numerical examples show that the results agree well with the solutions obtained from a frequency domain MoM and the original MOD method.



## Chapter 4.

# The Time Domain MoM Method for Dielectric Objects

For dielectric objects, the equivalent principle needs both electric and magnetic current to represent the materials in the other domain. Solving both currents requires the boundary conditions for both electric and magnetic fields.

Suppose there is a dielectric object as shown in Figure 4.1. The region of outside vacuum is called region 1 and the dielectric object is called region 2. No physical surface current exists for a real dielectric object; however, the equivalent principle allows us to remove the dielectric object and define two electric and magnetic currents on the surface so that the field in region 1 is the same as in the original problem. In the same way, one can replace the vacuum in region 1 with a dielectric and define another set of electric and magnetic currents so that the field inside region 2 is the same as in the original problem.

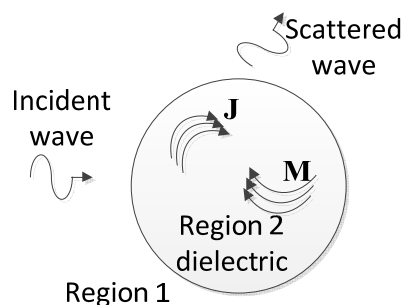


**Figure 4.1** Problem for a dielectric object.

Therefore, the boundary condition for dielectric objects is given in Eq. (4.1) and (4.2) for the case where the excitation locates in region 1

$$\left(-\mathbf{E}_\nu^s(\mathbf{J}, \mathbf{M})\right)_{\text{tan}} = \begin{cases} \left(\mathbf{E}^i\right)_{\text{tan}}, & \nu = 1 \\ 0, & \nu = 2 \end{cases} \quad (4.1)$$

$$\left(-\mathbf{H}_\nu^s(\mathbf{J}, \mathbf{M})\right)_{\text{tan}} = \begin{cases} \left(\mathbf{H}^i\right)_{\text{tan}}, & \nu = 1 \\ 0, & \nu = 2 \end{cases} \quad (4.2)$$

where  $\mathbf{E}_\nu^s(\mathbf{J}, \mathbf{M})$  and  $\mathbf{H}_\nu^s(\mathbf{J}, \mathbf{M})$  are the scattered electric and magnetic fields in region  $\nu$ . Eq. (4.1) is called the Electric Field Integral Equation (EFIE) and Eq. (4.2) is called the Magnetic Field Integral Equation (MFIE). Adding Eq. (4.1) to (4.2) gives the Combined Field Integral Equation (CFIE). In addition to these three equations, the PMCHW (Poggio, Miller, Chang, Harrington, and Wu) equation is another method for solving this problem. It adds the incident and scattered waves in two domains up on the boundary, to give the following equations

$$\left(-\mathbf{E}_1^s(\mathbf{J}, \mathbf{M})\right)_{\text{tan}} + \left(-\mathbf{E}_2^s(\mathbf{J}, \mathbf{M})\right)_{\text{tan}} = \left(\mathbf{E}^i\right)_{\text{tan}} \quad (4.3)$$

$$\left(-\mathbf{H}_1^s(\mathbf{J}, \mathbf{M})\right)_{\text{tan}} + \left(-\mathbf{H}_2^s(\mathbf{J}, \mathbf{M})\right)_{\text{tan}} = \left(\mathbf{H}^i\right)_{\text{tan}} \quad (4.4)$$

#### 4.1 Time Domain PMCHW Equation

The PMCHW equations given in Eqs. (4.3) and (4.4) can be used to handle time domain problems. Unlike the EFIE, the electric vector potential and magnetic scalar potential are also needed to formulate the scattered fields, as shown in Eqs. (4.5) and (4.6).

$$\sum_{\nu=1}^2 \left( \frac{\partial}{\partial t} \mathbf{A}_\nu(\mathbf{r}, t) + \nabla \Phi_\nu(\mathbf{r}, t) + \frac{1}{\epsilon_\nu} \nabla \times \mathbf{F}_\nu(\mathbf{r}, t) \right)_{\tan} = (\mathbf{E}^i(\mathbf{r}, t))_{\tan} \quad (4.5)$$

$$\sum_{\nu=1}^2 \left( \frac{\partial}{\partial t} \mathbf{F}_\nu(\mathbf{r}, t) + \nabla \Psi_\nu(\mathbf{r}, t) - \frac{1}{\mu_\nu} \nabla \times \mathbf{A}_\nu(\mathbf{r}, t) \right)_{\tan} = (\mathbf{H}^i(\mathbf{r}, t))_{\tan} \quad (4.6)$$

where  $\mathbf{A}$  is the magnetic vector potential,  $\Phi$  is the electric scalar potential,  $\mathbf{F}$  is the electric vector potential, and  $\Psi$  is the magnetic scalar potential.  $\nu = 1$  or  $2$  identify the regions of different materials. These potentials can be calculated by

$$\mathbf{A}_\nu(\mathbf{r}, t) = \frac{\mu_\nu}{4\pi} \int_S \frac{\mathbf{J}(\mathbf{r}', \tau_\nu)}{R} dS' \quad (4.7)$$

$$\mathbf{F}_\nu(\mathbf{r}, t) = \frac{\epsilon_\nu}{4\pi} \int_S \frac{\mathbf{M}(\mathbf{r}', \tau_\nu)}{R} dS' \quad (4.8)$$

$$\Phi_\nu(\mathbf{r}, t) = \frac{1}{4\pi\epsilon_\nu} \int_S \frac{\rho_e(\mathbf{r}', \tau_\nu)}{R} dS' \quad (4.9)$$

$$\Psi_\nu(\mathbf{r}, t) = \frac{1}{4\pi\mu_\nu} \int_S \frac{\rho_m(\mathbf{r}', \tau_\nu)}{R} dS' \quad (4.10)$$

$$\tau_\nu = t - R/c_\nu \quad (4.11)$$

where  $\mathbf{J}$  and  $\mathbf{M}$  are the electric and magnetic current, respectively, and  $\rho_e$  and  $\rho_m$  are the electric and magnetic charge density, respectively.  $R$  represents the distance between the observation point  $\mathbf{r}$  and the source point  $\mathbf{r}'$ , the retarded time is denoted by  $\tau_\nu$ , and the velocity of the electromagnetic wave propagated in the space with medium parameters ( $\epsilon_\nu$ ,  $\mu_\nu$ ) is  $c_\nu = 1/\sqrt{\epsilon_\nu\mu_\nu}$ .

The curl of the electric or magnetic vector potential can be expressed as

$$\frac{1}{\epsilon_\nu} \nabla \times \mathbf{F}_\nu(\mathbf{r}, t) = \pm \frac{1}{2} \mathbf{n} \times \mathbf{M}(\mathbf{r}, t) + \int_s \nabla \times \frac{\mathbf{M}(\mathbf{r}', \tau_\nu)}{4\pi R} dS', \quad \begin{array}{l} \text{(when } \nu = 1 \text{ it is positive and} \\ \nu = 2 \text{ is negative)} \end{array} \quad (4.12)$$

$$\frac{1}{\mu_\nu} \nabla \times \mathbf{A}_\nu(\mathbf{r}, t) = \pm \frac{1}{2} \mathbf{n} \times \mathbf{J}(\mathbf{r}, t) + \int_s \nabla \times \frac{\mathbf{J}(\mathbf{r}', \tau_\nu)}{4\pi R} dS', \quad \begin{array}{l} \text{(when } \nu = 1 \text{ it is positive and} \\ \nu = 2 \text{ is negative)} \end{array} \quad (4.13)$$

$$\nabla \times \frac{\mathbf{M}(\mathbf{r}', \tau_\nu)}{R} = \frac{1}{c_\nu} \frac{\partial}{\partial t} \mathbf{M}(\mathbf{r}', \tau_\nu) \times \frac{\hat{\mathbf{R}}}{R} + \mathbf{M}(\mathbf{r}', \tau_\nu) \times \frac{\hat{\mathbf{R}}}{R^2} \quad (4.14)$$

$$\nabla \times \frac{\mathbf{J}(\mathbf{r}', \tau_\nu)}{R} = \frac{1}{c_\nu} \frac{\partial}{\partial t} \mathbf{J}(\mathbf{r}', \tau_\nu) \times \frac{\hat{\mathbf{R}}}{R} + \mathbf{J}(\mathbf{r}', \tau_\nu) \times \frac{\hat{\mathbf{R}}}{R^2} \quad (4.15)$$

The time derivative of the potentials is handled by introducing Hertz vectors  $\mathbf{u}(\mathbf{r}, t)$  and  $\mathbf{v}(\mathbf{r}, t)$  for the electric and magnetic currents, defined by

$$\mathbf{J}(\mathbf{r}, t) = \frac{\partial}{\partial t} \mathbf{u}(\mathbf{r}, t) \quad (4.16)$$

$$\mathbf{M}(\mathbf{r}, t) = \frac{\partial}{\partial t} \mathbf{v}(\mathbf{r}, t) \quad (4.17)$$

and the relation between the Hertz vectors and the electric and magnetic charge densities are given by

$$\rho_e(\mathbf{r}, t) = -\nabla \cdot \mathbf{u}(\mathbf{r}, t) \quad (4.18)$$

$$\rho_m(\mathbf{r}, t) = -\nabla \cdot \mathbf{v}(\mathbf{r}, t) \quad (4.19)$$

Substituting Eqs. (4.7) – (4.19) into Eqs. (4.5) and (4.6), the TD-PMCHW is rewritten as



$$\sum_{\nu=1}^2 \left( \frac{\mu_{\nu}}{4\pi} \frac{\partial^2}{\partial t^2} \int_S \frac{\mathbf{u}(\mathbf{r}', \tau_{\nu})}{R} dS' - \frac{\nabla}{4\pi\epsilon_{\nu}} \int_S \frac{\nabla' \cdot \mathbf{u}(\mathbf{r}', \tau_{\nu})}{R} dS' \right. \\ \left. + \frac{1}{4\pi} \int_S \left( \frac{1}{c_{\nu}} \frac{\partial^2}{\partial t^2} \mathbf{v}(\mathbf{r}', \tau_{\nu}) \times \frac{\hat{\mathbf{R}}}{R} + \frac{\partial}{\partial t} \mathbf{v}(\mathbf{r}', \tau_{\nu}) \times \frac{\hat{\mathbf{R}}}{R^2} \right) dS' \right)_{\tan} = \left( \mathbf{E}^i(\mathbf{r}, t) \right)_{\tan} \quad (4.20)$$

$$\sum_{\nu=1}^2 \left( \frac{\epsilon_{\nu}}{4\pi} \frac{\partial^2}{\partial t^2} \int_S \frac{\mathbf{v}(\mathbf{r}', \tau_{\nu})}{R} dS' - \frac{\nabla}{4\pi\mu_{\nu}} \int_S \frac{\nabla' \cdot \mathbf{v}(\mathbf{r}', \tau_{\nu})}{R} dS' \right. \\ \left. + \frac{1}{4\pi} \int_S \left( \frac{1}{c_{\nu}} \frac{\partial^2}{\partial t^2} \mathbf{u}(\mathbf{r}', \tau_{\nu}) \times \frac{\hat{\mathbf{R}}}{R} + \frac{\partial}{\partial t} \mathbf{u}(\mathbf{r}', \tau_{\nu}) \times \frac{\hat{\mathbf{R}}}{R^2} \right) dS' \right)_{\tan} = \left( \mathbf{H}^i(\mathbf{r}, t) \right)_{\tan} \quad (4.21)$$

## 4.2 Basis Functions of the Time Domain PMCHW Equations

These unknown Hertz vectors  $\mathbf{u}(\mathbf{r}, t)$  and  $\mathbf{v}(\mathbf{r}, t)$  are spatially expanded by the RWG vector function set  $\mathbf{f}_n(\mathbf{r})$  as

$$\mathbf{u}(\mathbf{r}, t) = \sum_{n=1}^N u_n(t) \mathbf{f}_n(\mathbf{r}) \quad (4.22)$$

$$\mathbf{v}(\mathbf{r}, t) = \sum_{n=1}^N v_n(t) \mathbf{f}_n(\mathbf{r}) \quad (4.23)$$

and the transient coefficients in Eqs. (4.22) and (4.23) are further expanded by using the new temporal basis function  $\phi_j(st) - 2\phi_{j+1}(st) + \phi_{j+2}(st)$ . One obtains

$$u_n(t) = \sum_{j=0}^{\infty} u_{n,j} \left( \phi_j(st) - 2\phi_{j+1}(st) + \phi_{j+2}(st) \right) \quad (4.24)$$

$$v_n(t) = \sum_{j=0}^{\infty} v_{n,j} \left( \phi_j(st) - 2\phi_{j+1}(st) + \phi_{j+2}(st) \right) \quad (4.25)$$

Substituting Eq. (4.22) – (4.25) into Eqs. (4.26) and (4.27) results in

$$\begin{aligned}
& \sum_{\nu=1}^2 \left( \frac{\mu_{\nu}}{4\pi} \sum_{n=1}^N \int_S \frac{1}{R} \sum_{j=0}^{\infty} u_{n,j} \frac{s^2}{4} (\phi_j(s\tau_{\nu}) + 2\phi_{j+1}(s\tau_{\nu}) + \phi_{j+2}(s\tau_{\nu})) \mathbf{f}_n(\mathbf{r}') dS' \right. \\
& - \frac{1}{4\pi\epsilon_{\nu}} \nabla \sum_{n=1}^N \int_S \frac{1}{R} \sum_{j=0}^{\infty} u_{n,j} (\phi_j(s\tau_{\nu}) - 2\phi_{j+1}(s\tau_{\nu}) + \phi_{j+2}(s\tau_{\nu})) \nabla' \cdot \mathbf{f}_n(\mathbf{r}') dS' \\
& + \frac{1}{4\pi} \int_S \left( \frac{1}{c_{\nu}} \frac{s^2}{4} \sum_{n=1}^N \sum_{j=0}^{\infty} v_{n,j} [\phi_j(s\tau_{\nu}) + 2\phi_{j+1}(s\tau_{\nu}) + \phi_{j+2}(s\tau_{\nu})] \mathbf{f}_n(\mathbf{r}') \times \frac{\hat{\mathbf{R}}}{R} \right) dS' \Bigg)_{\tan} \\
& + \frac{1}{4\pi} \int_S \left( \frac{s}{2} \sum_{n=1}^N \sum_{j=0}^{\infty} v_{n,j} [\phi_j(s\tau_{\nu}) - \phi_{j+2}(s\tau_{\nu})] \mathbf{f}_n(\mathbf{r}') \times \frac{\hat{\mathbf{R}}}{R^2} \right) dS' \Bigg)_{\tan} \\
& = (\mathbf{E}^i(\mathbf{r}, t))_{\tan} \tag{4.26}
\end{aligned}$$

and

$$\begin{aligned}
& \sum_{\nu=1}^2 \left( \frac{\epsilon_{\nu}}{4\pi} \sum_{n=1}^N \int_S \frac{1}{R} \sum_{j=0}^{\infty} v_{n,j} \frac{s^2}{4} (\phi_j(st) + 2\phi_{j+1}(st) + \phi_{j+2}(st)) \mathbf{f}_n(\mathbf{r}') dS' \right. \\
& - \frac{1}{4\pi\mu_{\nu}} \nabla \sum_{n=1}^N \int_S \frac{1}{R} \sum_{j=0}^{\infty} v_{n,j} (\phi_j(st) - 2\phi_{j+1}(st) + \phi_{j+2}(st)) \nabla' \cdot \mathbf{f}_n(\mathbf{r}') dS' \\
& + \frac{1}{4\pi} \int_S \left( \frac{1}{c_{\nu}} \frac{s^2}{4} \sum_{n=1}^N \sum_{j=0}^{\infty} u_{n,j} [\phi_j(s\tau_{\nu}) + 2\phi_{j+1}(s\tau_{\nu}) + \phi_{j+2}(s\tau_{\nu})] \mathbf{f}_n(\mathbf{r}') \times \frac{\hat{\mathbf{R}}}{R} \right) dS' \Bigg)_{\tan}
\end{aligned}$$

$$\begin{aligned}
& + \frac{1}{4\pi} \int_S \left( \frac{s}{2} \sum_{n=1}^N \sum_{j=0}^{\infty} u_{n,j} [\phi_j(s\tau_v) - \phi_{j+2}(s\tau_v)] \mathbf{f}_n(\mathbf{r}') \times \frac{\hat{\mathbf{R}}}{R^2} \right) dS' \Bigg|_{\tan} \\
& = \left( \mathbf{H}^i(\mathbf{r}, t) \right)_{\tan}
\end{aligned} \tag{4.27}$$

### 4.3 Testing of the Time Domain PMCHW Equations

Following the testing procedures described in Section 2.4 for applying the temporal testing first and then the spatial testing, one obtains

$$\begin{aligned}
& \sum_{v=1}^2 \left( \frac{\mu_v s^2}{4} \sum_{n=1}^N \sum_{j=0}^i u_{n,j} \left( A_{mnij}^v + 2A_{mni,j+1}^v + A_{mni,j+2}^v \right) \right. \\
& \quad + \frac{1}{\epsilon_v} \sum_{n=1}^N \sum_{j=0}^i u_{n,j} \left( B_{mnij}^v - 2B_{mni,j+1}^v + B_{mni,j+2}^v \right) \\
& \quad + \frac{1}{c_v} \frac{s^2}{4} \sum_{n=1}^N \sum_{j=0}^i v_{n,j} \left( C_{mnij}^v + 2C_{mni,j+1}^v + C_{mni,j+2}^v \right) \\
& \quad \left. + \frac{s}{2} \sum_{n=1}^N \sum_{j=0}^i v_{n,j} \left( D_{mnij}^v - D_{mni,j+2}^v \right) \right) = \Omega_{m,i}^E
\end{aligned} \tag{4.28}$$

and

$$\begin{aligned}
& \sum_{v=1}^2 \left( \frac{\epsilon_v s^2}{4} \sum_{n=1}^N \sum_{j=0}^i v_{n,j} \left( A_{mnij}^v + 2A_{mni,j+1}^v + A_{mni,j+2}^v \right) \right. \\
& \quad + \frac{1}{\mu_v} \sum_{n=1}^N \sum_{j=0}^i v_{n,j} \left( B_{mnij}^v - 2B_{mni,j+1}^v + B_{mni,j+2}^v \right) \\
& \quad \left. + \frac{1}{c_v} \frac{s^2}{4} \sum_{n=1}^N \sum_{j=0}^i u_{n,j} \left( C_{mnij}^v + 2C_{mni,j+1}^v + C_{mni,j+2}^v \right) \right)
\end{aligned}$$

$$+\frac{s}{2}\sum_{n=1}^N\sum_{j=0}^i u_{n,j}\left(D_{mnij}^v-D_{mni,j+2}^v\right)=\Omega_{m,i}^H \quad (4.29)$$

The integrals in Eqs. (4.28) and (4.29) are given by

$$A_{mnij}^v=\int_S\mathbf{f}_m(\mathbf{r})\cdot\int_S\frac{1}{4\pi R}I_{ij}(t_{d,v})\mathbf{f}_n(\mathbf{r}')dS'dS \quad (4.30)$$

$$B_{mnij}^v=\int_S\nabla\cdot\mathbf{f}_m(\mathbf{r})\int_S\frac{1}{4\pi R}I_{ij}(t_{d,v})\nabla'\cdot\mathbf{f}_n(\mathbf{r}')dS'dS \quad (4.31)$$

$$C_{mnij}^v=\int_S\mathbf{f}_m(\mathbf{r})\cdot\int_S\frac{1}{4\pi}\frac{1}{c_v}I_{ij}\left(s\frac{R}{c_v}\right)\mathbf{f}_n(\mathbf{r}')\times\frac{\hat{\mathbf{R}}}{R}dS'dS \quad (4.32)$$

$$D_{mnij}^v=\int_S\mathbf{f}_m(\mathbf{r})\cdot\int_S\frac{1}{4\pi}\frac{1}{c_v}I_{ij}\left(s\frac{R}{c_v}\right)\mathbf{f}_n(\mathbf{r}')\times\frac{\hat{\mathbf{R}}}{R^2}dS'dS \quad (4.33)$$

$$\alpha_{mn}^v=A_{mnij}^v\Big|_{j=i}=\int_S\mathbf{f}_m(\mathbf{r})\cdot\int_S\frac{1}{4\pi R}e^{(-t_{d,v}/2)}\mathbf{f}_n(\mathbf{r}')dS'dS \quad (4.34)$$

$$\beta_{mn}^v=B_{mnij}^v\Big|_{j=i}=\int_S\nabla\cdot\mathbf{f}_m(\mathbf{r})\int_S\frac{1}{4\pi R}e^{(-t_{d,v}/2)}\nabla'\cdot\mathbf{f}_n(\mathbf{r}')dS'dS \quad (4.35)$$

$$\gamma_{mn}^v=C_{mnij}^v\Big|_{j=i}=\int_S\mathbf{f}_m(\mathbf{r})\cdot\int_S\frac{1}{4\pi}e^{\left(\frac{-sR}{2c_v}\right)}\mathbf{f}_n(\mathbf{r}')\times\frac{\hat{\mathbf{R}}}{R}dS'dS \quad (4.36)$$

$$\chi_{mn}^v=D_{mnij}^v\Big|_{j=i}=\int_S\mathbf{f}_m(\mathbf{r})\cdot\int_S\frac{1}{4\pi}e^{\left(\frac{-sR}{2c_v}\right)}\mathbf{f}_n(\mathbf{r}')\times\frac{\hat{\mathbf{R}}}{R^2}dS'dS \quad (4.37)$$

$$\Omega_{m,i}^E=\int_S\mathbf{f}_m(\mathbf{r})\cdot\mathbf{V}_i^E(\mathbf{r})dS \quad (4.38)$$

$$\Omega_{m,i}^H=\int_S\mathbf{f}_m(\mathbf{r})\cdot\mathbf{V}_i^H(\mathbf{r})dS \quad (4.39)$$

$$t_{d,v}=sR/c_v \quad (4.40)$$

Transforming Eqs. (4.28) and (4.29) into a matrix form, the TD-PMCHW formulations are expressed as

$$\begin{bmatrix} [Z_{mn}^{E1}] & [Z_{mn}^{H1}] \\ [Z_{mn}^{E2}] & [Z_{mn}^{H2}] \end{bmatrix} \begin{bmatrix} [u_{n,i}] \\ [v_{n,i}] \end{bmatrix} = \begin{bmatrix} [V_{m,i}^E] \\ [V_{m,i}^H] \end{bmatrix} \quad (4.41)$$

where

$$Z_{mn}^{E1} = \sum_{\nu=1}^2 \left[ \frac{\mu_{\nu} s^2}{4} \alpha_{mn}^{\nu} + \frac{1}{\varepsilon_{\nu}} \beta_{mn}^{\nu} \right] \quad (4.42)$$

$$Z_{mn}^{H1} = \sum_{\nu=1}^2 \left[ \frac{1}{c_{\nu}} \frac{s^2}{4} \gamma_{mn}^{\nu} + \frac{s}{2} \chi_{mn}^{\nu} \right] \quad (4.43)$$

$$Z_{mn}^{E2} = \sum_{\nu=1}^2 \left[ \frac{1}{c_{\nu}} \frac{s^2}{4} \gamma_{mn}^{\nu} + \frac{s}{2} \chi_{mn}^{\nu} \right] \quad (4.44)$$

$$Z_{mn}^{H2} = \sum_{\nu=1}^2 \left[ \frac{\varepsilon_{\nu} s^2}{4} \alpha_{mn}^{\nu} + \frac{1}{\mu_{\nu}} \beta_{mn}^{\nu} \right] \quad (4.45)$$

$$\begin{aligned} V_m^E = \Omega_{m,i}^E - \sum_{\nu=1}^2 & \left( \frac{\mu_{\nu} s^2}{4} \sum_{n=1}^N \sum_{j=0}^{i-1} u_{n,j} \left( A_{mnij}^{\nu} + 2A_{mni,j+1}^{\nu} + A_{mni,j+2}^{\nu} \right) \right. \\ & + \frac{1}{\varepsilon_{\nu}} \sum_{n=1}^N \sum_{j=0}^{i-1} u_{n,j} \left( B_{mnij}^{\nu} - 2B_{mni,j+1}^{\nu} + B_{mni,j+2}^{\nu} \right) \\ & + \frac{1}{c_{\nu}} \frac{s^2}{4} \sum_{n=1}^N \sum_{j=0}^{i-1} v_{n,j} \left( C_{mnij}^{\nu} + 2C_{mni,j+1}^{\nu} + C_{mni,j+2}^{\nu} \right) \\ & \left. + \frac{s}{2} \sum_{n=1}^N \sum_{j=0}^{i-1} v_{n,j} \left( D_{mnij}^{\nu} - D_{mni,j+2}^{\nu} \right) \right) \end{aligned} \quad (4.46)$$

$$\begin{aligned}
V_m^H &= \Omega_{m,i}^H - \sum_{\nu=1}^2 \left( \frac{\epsilon_\nu s^2}{4} \sum_{n=1}^N \sum_{j=0}^{i-1} v_{n,j} \left( A_{mni}^\nu + 2A_{mni,j+1}^\nu + A_{mni,j+2}^\nu \right) \right. \\
&\quad + \frac{1}{\mu_\nu} \sum_{n=1}^N \sum_{j=0}^{i-1} v_{n,j} \left( B_{mni}^\nu - 2B_{mni,j+1}^\nu + B_{mni,j+2}^\nu \right) \\
&\quad + \frac{1}{c_\nu} \frac{s^2}{4} \sum_{n=1}^N \sum_{j=0}^{i-1} u_{n,j} \left( C_{mni}^\nu + 2C_{mni,j+1}^\nu + C_{mni,j+2}^\nu \right) \\
&\quad \left. + \frac{s}{2} \sum_{n=1}^N \sum_{j=0}^{i-1} u_{n,j} \left( D_{mni}^\nu - D_{mni,j+2}^\nu \right) \right)
\end{aligned} \tag{4.47}$$

Finally, the computational efficiency can further be improved by using the new formulations. Eqs. (4.46) and (4.47) are written as

$$V_m^E = \Omega_{m,i}^E - \sum_{\nu=1}^2 \sum_{n=1}^N K_{mni}^\nu \tag{4.48}$$

$$V_m^H = \Omega_{m,i}^H - \sum_{\nu=1}^2 \sum_{n=1}^N L_{mni}^\nu \tag{4.49}$$

where

$$\begin{aligned}
K_{mni}^\nu &= \sum_{j=0}^{i-1} \left( \frac{\mu_\nu s^2}{4} u_{n,j} \left( A_{mni}^\nu + 2A_{mni,j+1}^\nu + A_{mni,j+2}^\nu \right) \right. \\
&\quad + \frac{1}{\epsilon_\nu} u_{n,j} \left( B_{mni}^\nu - 2B_{mni,j+1}^\nu + B_{mni,j+2}^\nu \right) \\
&\quad + \frac{1}{c_\nu} \frac{s^2}{4} v_{n,j} \left( C_{mni}^\nu + 2C_{mni,j+1}^\nu + C_{mni,j+2}^\nu \right) \\
&\quad \left. + \frac{s}{2} v_{n,j} \left( D_{mni}^\nu - D_{mni,j+2}^\nu \right) \right)
\end{aligned} \tag{4.50}$$

$$\begin{aligned}
H_{mni}^v = \sum_{j=0}^{i-1} & \left( \frac{\epsilon_v s^2}{4} v_{n,j} \left( A_{mnij}^v + 2A_{mni,j+1}^v + A_{mni,j+2}^v \right) \right. \\
& + \frac{1}{\mu_v} v_{n,j} \left( B_{mnij}^v - 2B_{mni,j+1}^v + B_{mni,j+2}^v \right) \\
& + \frac{1}{c_v} \frac{s^2}{4} u_{n,j} \left( C_{mnij}^v + 2C_{mni,j+1}^v + C_{mni,j+2}^v \right) \\
& \left. + \frac{s}{2} u_{n,j} \left( D_{mnij}^v - D_{mni,j+2}^v \right) \right)
\end{aligned} \tag{4.51}$$

#### 4.4 Numerical Examples

##### Example 4-1: A Dielectric Sphere

A dielectric sphere with a radius of 0.1 m, relative permittivity  $\epsilon_r = 1$ , and relative permeability  $\mu_r = 0.5$  is modeled by triangular patches containing 84 edges and 56 patches. The incident wave exciting the structure is a  $\phi$ -polarized  $T$ -pulse with a duration of 10 lm, starting at 4 lm, and arrives from the direction of  $\theta = 0^\circ$  and  $\phi = 0^\circ$ . It has a bandwidth of 120 MHz. Figure 9.28 plots the scattered far field along the direction of  $\theta = 180^\circ$  and  $\phi = 0^\circ$ , as computed by the new MOD method. The computed result agrees well with the frequency domain solution.

##### Example 4-2: A Dielectric Cylinder

A dielectric cylinder with a radius of 0.1 m and a height of 0.2 m is radiated with a  $\phi$ -polarized  $T$ -pulse with a duration of 10 lm, starting at 4 lm, and coming from the direction of  $\theta = 0^\circ$  and  $\phi = 0^\circ$ . It has a relative permittivity  $\epsilon_r = -2$  and permeability  $\mu_r = -1$ . It has a bandwidth of 120 MHz. The structure is discretized by triangular patches containing 246 edges and 164 patches. The scattered far field along the direction

$\theta = 180^\circ$  and  $\phi = 0^\circ$  is computed using the new MOD method. The results are plotted in Figure 4.3 along with the IDFT of the frequency domain solution. The two results agree well with each other.

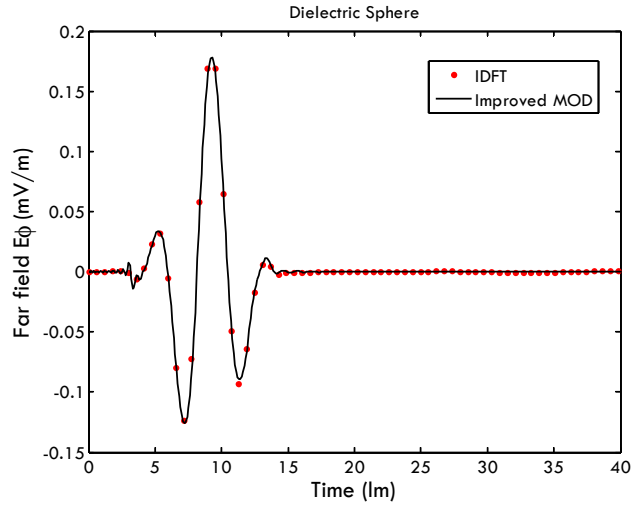


**Figure 4.2** Transient scattered far field from a dielectric sphere of  $\epsilon_r = 1$  and  $\mu_r = 0.5$ .

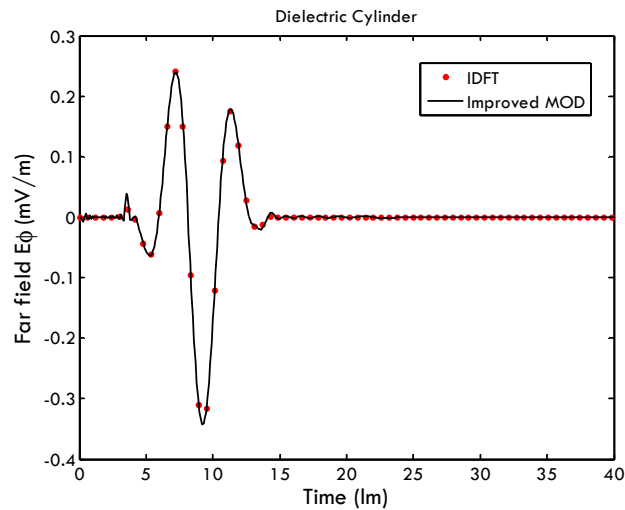


**Figure 4.3** Transient scattered far field from a dielectric cylinder of  $\epsilon_r = -2$  and  $\mu_r = -1$ .



#### Example 4-3: Structures with Different Relative Permittivity

The dielectric sphere of Example 18 is studied further using different materials with a relative permeability of  $\mu_r = 1$  and relative permittivity of  $\epsilon_r = 0.5$  or 10. The structure is excited with a  $\phi$ -polarized  $T$ -pulse starting at 4 lm and is incident from  $\theta = 0^\circ$  and  $\phi = 0^\circ$ . Two versions of the  $T$ -pulse are considered, with pulse durations of 10 lm and 20 lm. These correspond to a bandwidth of 120 MHz and 60 MHz, respectively. Figure 9.30 plots the scattered far field along the direction  $\theta = 180^\circ$  and  $\phi = 0^\circ$  using the new MOD method. Both results for  $\epsilon_r = 0.5$  and  $\epsilon_r = 10$  agree well with the frequency domain solutions.

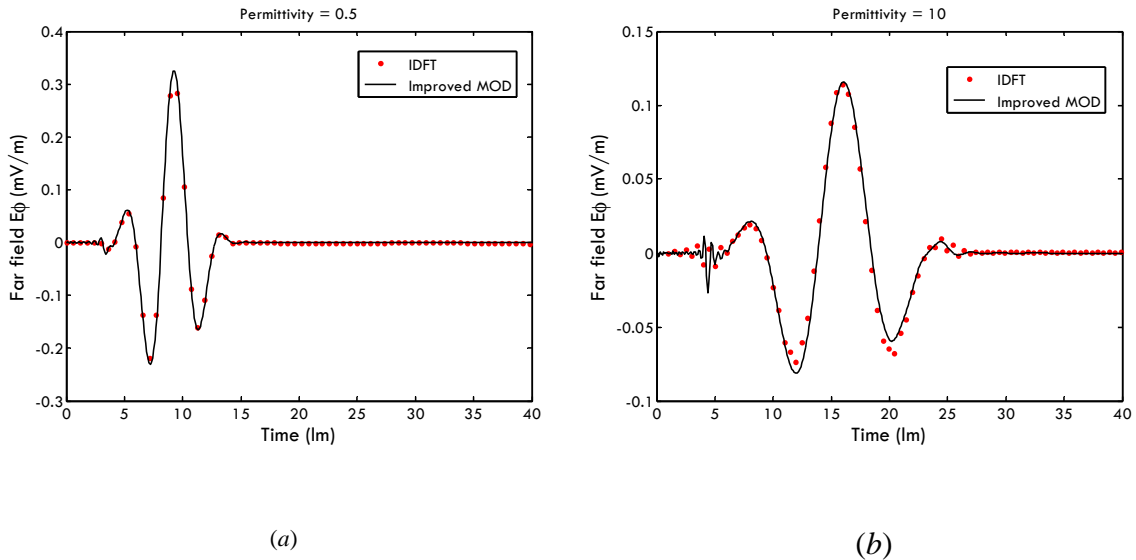


**Figure 4.4** Transient scattered far field from a dielectric sphere with  $\mu_r = 1$ :

(a)  $\epsilon_r = 0.5$ . (b)  $\epsilon_r = 10$ .

#### Example 4-4: Structures with Different Relative Permeability

The same dielectric sphere of the previous example is considered with different material parameters. The sphere has a relative permittivity  $\epsilon_r = 2$ , but it can have a

different relative permeability of  $\mu_r = 1$  or 2. The structure is excited with a  $T$ -pulse with the same parameters used in Example 17. Figure 9.31 plots the scattered far field along the direction of  $\theta = 180^\circ$  and  $\phi = 0^\circ$  computed by the improved MOD method. Both results for  $\mu_r = 1$  and  $\mu_r = 2$  agree well with the frequency domain solutions.

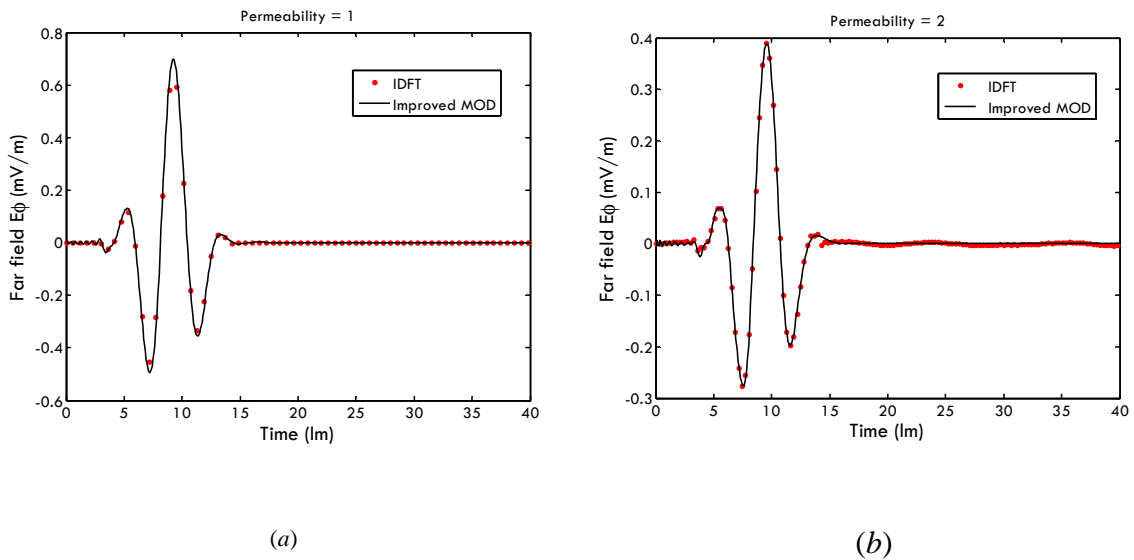


**Figure 4.5** Transient scattered far field for a dielectric sphere with  $\epsilon_r = 2$ :

(a)  $\mu_r = 1$ . (b)  $\mu_r = 2$ .

The MOD approach has been presented to solve the time domain PMCHW equations to analyze the scattering from three-dimensional arbitrarily shaped dielectric structures. The agreement is good between the solutions obtained using the proposed methods and the IDFT of the frequency domain solution.

## Chapter 5.

### Parallelization of the Time Domain MoM Code

This section introduces how to parallelize the marching-on-in-degree (MOD) time domain method of moment (MoM) code.

The major operations for a serial MOD time domain MoM code, based on the theories in Chapter 3 and 4, are to fill a matrix equation and to solve that matrix equation. These two steps are the most time consuming steps. Other operations, such as calculating the far field or near field, take much less time than these two. Therefore, this chapter describes how to parallelize these two major steps.

The message passing interface (MPI) [26] is a widely used library for parallel computing. It is a language-independent communication protocol and it is standardized and portable, so the same code can be easily compiled on different operation systems and cluster setups.

In addition to MPI, I also used the ScaLAPACK (Scalable Linear Algebra PACKage) library.[27] This is a library that provides high-performance linear algebra routines that support MPI protocol. The use of ScaLAPACK allowed me to fill and solve the matrix equation efficiently.

#### 5.1 Parallelization Architecture of the Time Domain MoM

The MPI is a distributed memory system; the major difference between it and a shared memory system is that each CPU in MPI controls its own memory and the whole

memory of the cluster or computer is distributed into several parts, as shown in Figure 5.1. The use of a distributed memory system provides two major advantages. First, some of the clusters do not have one global memory; shared memory has difficulties in these types of cases. Second, a distributed memory system makes programming robust when different CPUs attempt to read from and write to the same memory unit at the same time, which often happens when solving a matrix equation. [28]

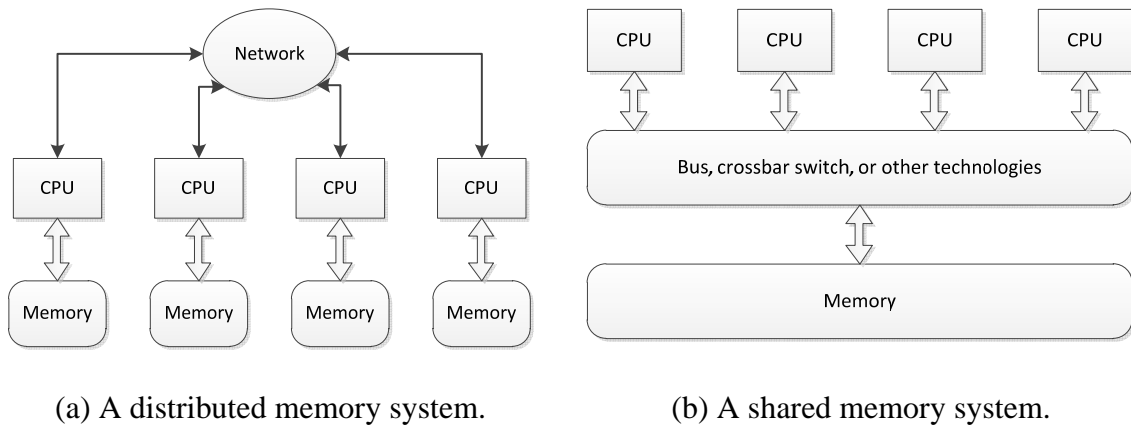


**Figure 5.1** The difference between a distributed memory system and a shared memory system.

## 5.2 Matrix Filling

When using MPI technology, the matrix needs to be distributed into different CPU processes, and how the matrix is distributed affects the efficiency of the code. ScaLAPACK routines use block partitioned algorithms to reduce data movements. It partitions the matrix into many small blocks and distributes those blocks into all the CPU processes. [27]

The difference between serial and parallel matrix filling is how the matrix is distributed into all the CPU cores. Serial code has only one working CPU core and that

core owns all the matrix elements, while in parallel code, each CPU core owns part of the matrix elements. The process to fill the values of the matrix elements is the same for serial and parallel code, while solving the matrix needs some communication between CPUs.

Load balance is a measurement of the balance of the computation. If all the processes start and stop simultaneously, the computation has a good load balance. On the other hand, if some processes finish their jobs faster than others, they need to wait for others to finish and this wastes CPU resources. ScaLAPACK therefore uses a block cyclic distribution to achieve a good load balance. It divides  $P$  processes into a  $P=P_r \times P_c$  process grid and distributes the matrix on this grid. The following are three examples that review the relationship of load balance between the process grid and block size.

For example, consider a  $9 \times 9$  matrix and the process grid and block size given in Table 5.1.

**Table 5.1.** Examples for ScaLAPACK distributing the matrix for different process grids and block sizes.

Examples	Number of CPU processes	Process grid	Block size
Example 1	6	$P_r = 2, P_c = 3$	$2 \times 2$
Example 2	4	$P_r = 2, P_c = 2$	$2 \times 2$
Example 3	4	$P_r = 2, P_c = 2$	$3 \times 3$

Example 1 has 6 CPU cores and they are allocated into a  $2 \times 3$  grid. The first step is to partition the matrix into many blocks with a block size of  $2 \times 2$ . The blocks are then cylindrically allocated into the  $2 \times 3$  process grid, as shown in Figure 5.2. Finally, the data of the matrix are stored in different CPU processes.

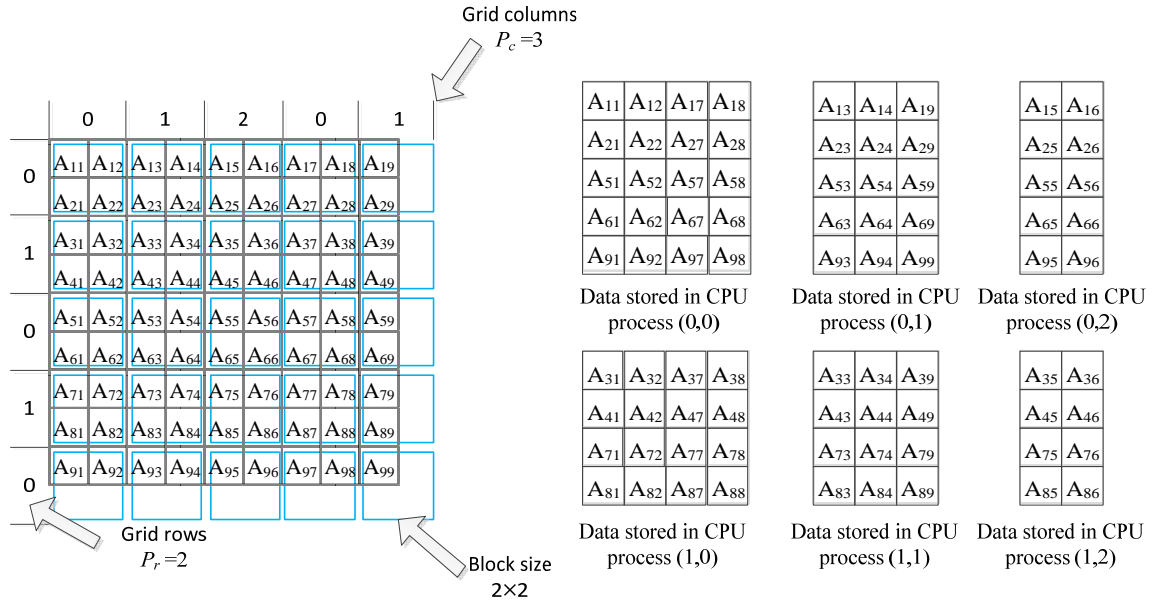


**Figure 5.2** The distribution of matrix in Example 1.

Example 2 has 4 CPU cores and they are allocated into a  $2 \times 2$  grid. As in Example 1, the first step is to partition the matrix into many  $2 \times 2$  blocks and then to cylindrically allocate the blocks into the  $2 \times 2$  process grid, as shown in Figure 5.3. A comparison with Example 1 reveals that the load balance is better than in Example 1. Many simulations also show that when the number of CPU processes is a power of two, the calculation is faster than for the cases where it is not.

Example 3 has the same number of CPU cores and process grids as Example 2. The difference is the block size, which is  $3 \times 3$ . The blocks are cylindrically allocated into the  $2 \times 2$  process grid, as shown in Figure 5.4. A comparison to Example 2 shows that reducing the block size can improve the load balance. However, a large block size can reduce the data movement in the memory and improve the performance. Therefore, a balance is needed between the load balance and data movement.

In the parallel time domain code, each CPU process needs to determine which matrix elements are stored in its memory, using the block cyclic method. Once this is known, then the process to calculate the values of the matrix elements is the same as a serial code.

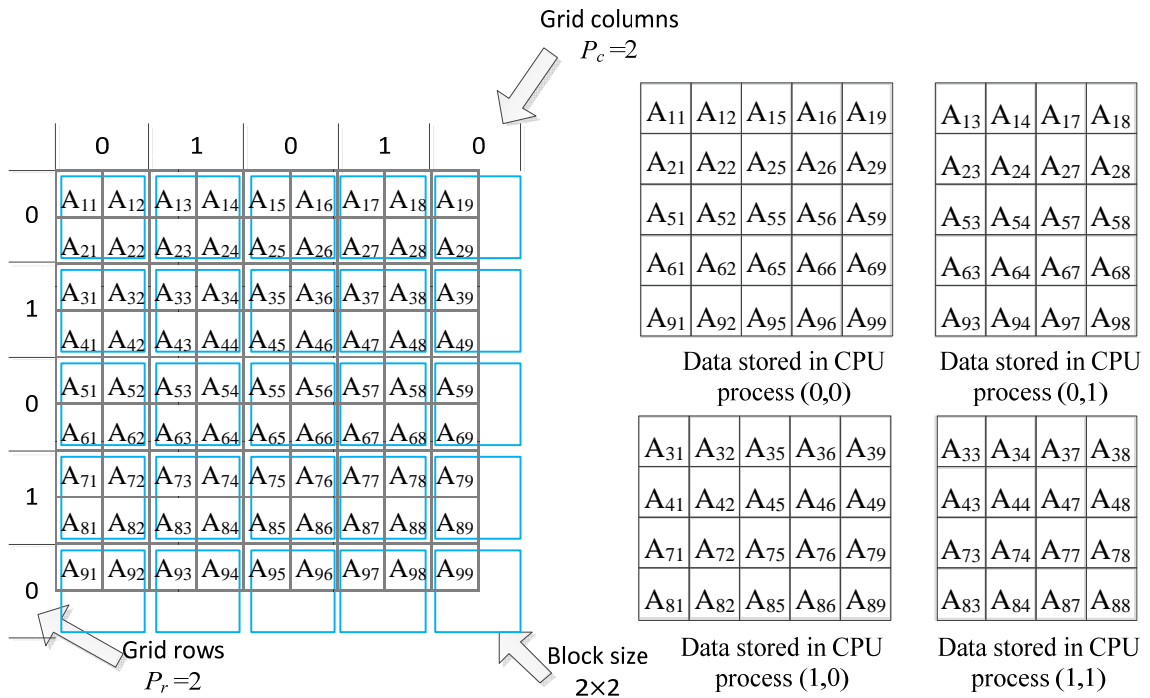


Figure 5.3 The distribution of matrix in Example 2.

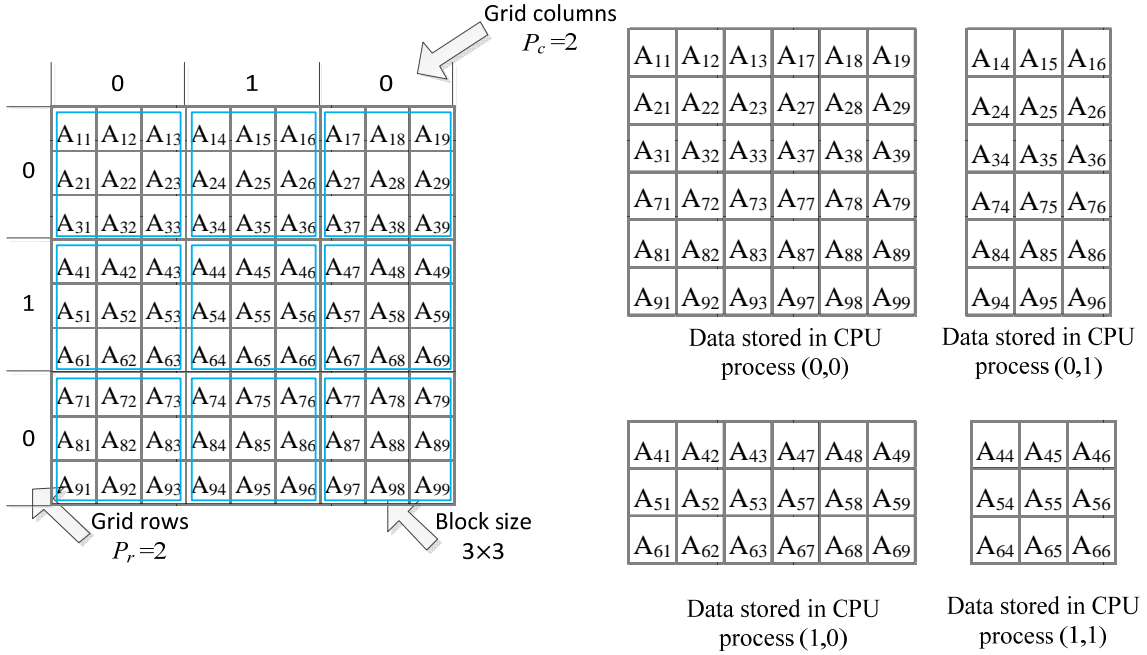


Figure 5.4 The distribution of matrix in Example 3.

In method of moment, a matrix equation needs to be filled in the form of Eq. (5.1), in which  $\mathbf{Z}$  and  $\mathbf{V}$  are computed from the structure and the excitation,  $\mathbf{I}$ , is the unknown current or potential to be solved. The way to store the  $N \times N$   $\mathbf{Z}$  matrix is already shown above. The vectors  $\mathbf{I}$  and  $\mathbf{V}$  can be treat as an  $N \times 1$  matrix and stored in the same way.

$$[\mathbf{Z}]_{N \times N} [\mathbf{I}]_{N \times 1} = [\mathbf{V}]_{N \times 1} \quad (5.1)$$

### 5.3 Solving the Matrix Equation

In my code, the matrix equation is solved by LU decomposition. Unlike the Gaussian elimination method or iterative methods, when the vector  $\mathbf{V}$  is changed and  $\mathbf{Z}$  is unchanged, the LU decomposition does not need to be repeated and the same  $\mathbf{L}$  and  $\mathbf{U}$  matrix can be reused. This is very useful for marching-on-in-degree method because for



each different degree, the matrix  $\mathbf{Z}$  is always the same; the only thing that changes is the vector  $\mathbf{V}$ .

ScaLAPACK provides an LU decomposition subroutine for solving the matrix equation in parallel. This algorithm is based on the block operation mention above. If a matrix equation as shown in Eq.(5.1) exists, the matrix  $\mathbf{Z}$  can be decomposed into two multiplication matrixes, as shown Eq. (5.2), where  $\mathbf{L}$  is a lower triangular matrix and  $\mathbf{U}$  is an upper triangular matrix. LU decomposition for matrix elements is discussed in many materials, but the same idea also works for blocks. For Example 3, in Figure 5.4, I can divide the  $9 \times 9$  matrix into nine  $3 \times 3$  submatrixes. The LU decomposition can then be done with submatrixes, as shown Eq. (5.3), in which  $\mathbf{Z}_{ij}$ ,  $\mathbf{L}_{ij}$ , and  $\mathbf{U}_{ij}$  are submatrixes divided by blocks, as shown in Figure 5.4.

$$[\mathbf{Z}]_{N \times N} = [\mathbf{L}]_{N \times N} [\mathbf{U}]_{N \times N} \quad (5.2)$$

$$\begin{bmatrix} \mathbf{Z}_{11} & \mathbf{Z}_{12} & \mathbf{Z}_{13} \\ \mathbf{Z}_{21} & \mathbf{Z}_{22} & \mathbf{Z}_{23} \\ \mathbf{Z}_{31} & \mathbf{Z}_{32} & \mathbf{Z}_{33} \end{bmatrix}_{9 \times 9} = \begin{bmatrix} \mathbf{L}_{11} & \mathbf{0} & \mathbf{0} \\ \mathbf{L}_{21} & \mathbf{L}_{22} & \mathbf{0} \\ \mathbf{L}_{31} & \mathbf{L}_{32} & \mathbf{L}_{33} \end{bmatrix}_{9 \times 9} \begin{bmatrix} \mathbf{U}_{11} & \mathbf{U}_{12} & \mathbf{U}_{13} \\ \mathbf{0} & \mathbf{U}_{22} & \mathbf{U}_{23} \\ \mathbf{0} & \mathbf{0} & \mathbf{U}_{33} \end{bmatrix}_{9 \times 9} \quad (5.3)$$

The LU decomposition is a recursive algorithm. This decomposition can be first applied for the elements of the submatrix  $\mathbf{Z}_{11}$  to obtain its LU decomposition of  $\mathbf{L}_{11}$  and  $\mathbf{U}_{11}$ . The submatrix of  $\mathbf{L}_{12}$  and  $\mathbf{L}_{13}$  in the first column of the  $\mathbf{L}$  matrix can then be obtained by inverting the  $\mathbf{U}_{11}$  from Eq. (5.4). Inversion of  $\mathbf{L}_{11}$  can also obtain  $\mathbf{U}_{12}$  and  $\mathbf{U}_{13}$  in the first row of the  $\mathbf{U}$  matrix. After the submatrixes of  $\mathbf{L}$  and  $\mathbf{U}$  of the first column or row are known, then the submatrixes of the second column or row can be calculated from Eq. (5.4). This then continues for the next column and row in a recursive way.

$$\begin{bmatrix} \mathbf{Z}_{11} & \mathbf{Z}_{12} & \mathbf{Z}_{13} \\ \mathbf{Z}_{21} & \mathbf{Z}_{22} & \mathbf{Z}_{23} \\ \mathbf{Z}_{31} & \mathbf{Z}_{32} & \mathbf{Z}_{33} \end{bmatrix} = \begin{bmatrix} \mathbf{L}_{11}\mathbf{U}_{11} & \mathbf{L}_{11}\mathbf{U}_{12} & \mathbf{L}_{11}\mathbf{U}_{13} \\ \mathbf{L}_{21}\mathbf{U}_{11} & \mathbf{L}_{21}\mathbf{U}_{12} + \mathbf{L}_{22}\mathbf{U}_{22} & \mathbf{L}_{21}\mathbf{U}_{13} + \mathbf{L}_{22}\mathbf{U}_{23} \\ \mathbf{L}_{31}\mathbf{U}_{11} & \mathbf{L}_{31}\mathbf{U}_{12} + \mathbf{L}_{31}\mathbf{U}_{22} & \mathbf{L}_{31}\mathbf{U}_{13} + \mathbf{L}_{32}\mathbf{U}_{23} + \mathbf{L}_{33}\mathbf{U}_{33} \end{bmatrix} \quad (5.4)$$

Solving the parallel LU decomposition requires that the CPU cores communicate with each other because they need the results for the previous rows or columns. Therefore, perfect load balance cannot occur when waiting for the data from other CPU cores. For example, when one of the CPU cores is computing the  $\mathbf{L}_{11}$  and  $\mathbf{U}_{11}$ , other CPU cores are idle because all the other operations rely on the value of these two matrixes. The communication also takes time and reduces the speed of simulation. ScaLAPACK is optimized to improve the load balance in the way it stores the matrix in memory and reduces the communication.

#### 5.4 Numerical Examples for the Parallelization

In this section, some numerical examples are provided to illustrate the performance of the parallel time domain code. The first two examples have the time domain results computed from different platforms and are compared with the IDFT result from the frequency domain code. They show the accuracy of the parallel code from different platforms. The third and fourth examples are simulated with different numbers of CPU cores. They show the time reduction for parallelization and the efficiency change. The fifth example is the parallel code for handling large vehicles. It shows that the parallel time domain code is able to handle complex objects. The sixth example is a simulation with a dielectric.

In Example 1, I compared the far field of the parallel time domain result with the IDFT result from a frequency domain EM simulator HOBBIES to show the accuracy of

the parallel code. I simulated a sphere with a radius of 1 meter, where the incident wave comes from the  $-z$  direction with polarization of  $x$  direction. I calculated the  $x$  component of the scattered far field at the  $+z$  direction and compared the result to the frequency domain IDFT result. The sphere is discretized into 14,738 triangular patches and results in 22,107 RWG unknowns. The excitation is a T-pulse with a bandwidth of 200 MHz. The parallel time domain code was run on two different computers. The first computer is a cluster with 10 compute nodes and 20 CPU cores. It has a Linux operating system with Intel MPI. The second computer is a desktop with 4 CPU cores. It has a Windows operating system with MPICH2 MPI. The results are plotted in Figure 5.5. The parallel time domain code run on different computers gave the exactly same results and they agree well with the frequency domain result.

In Example 2, the object is the same as in the first example. The excitation pulse is changed to a T-pulse with a bandwidth of 400 MHz. The higher frequency requires a finer mesh. In this example, the sphere is discretized into 39,810 triangular patches and resulting in 59,715 unknowns. The incident and scattered direction are the same as the previous example. The parallel time domain results from different computers are compared with the IDFT result from the frequency domain solver HOBBIES. The results are plotted in Figure 5.6. As with the previous result, the parallel time domain results are identical and they match well with the frequency domain result.

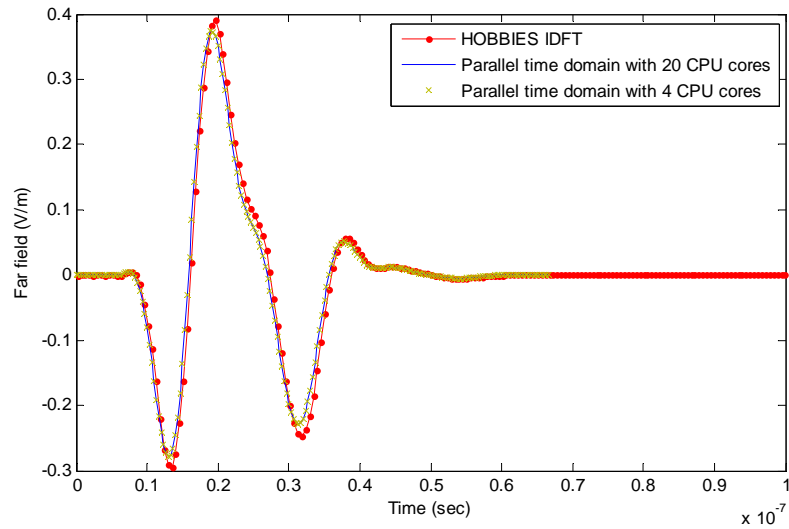


**Figure 5.5.** The far field comparison of the time and frequency domain results for the first numerical example.

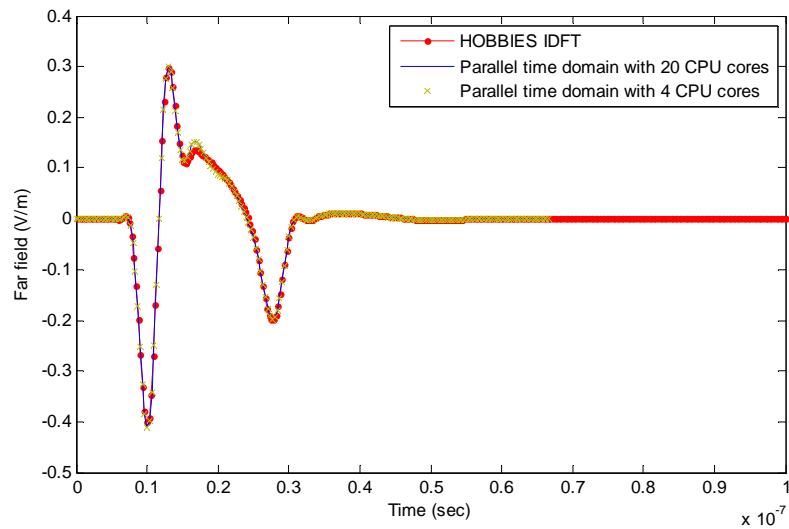


**Figure 5.6** The far field comparison of the time and frequency domain results for the second numerical example.

Example 3 shows the parallel efficiency of the code. I still used a sphere with radius of 1 meter, which was discretized into 1440 triangular patches and 2160 unknowns.

A plane wave with a bandwidth of 180 MHz comes from  $-z$  direction. I ran this project on a Linux cluster with different number of CPU cores and compared the efficiency. Parallel efficiency is a measurement of the quality of the parallelization and is defined in Eq. (5.5). The computation time and parallel efficiency are listed in Table 5.2. I can see that the parallel efficiency decreases as I use more CPU cores. This is because, in the LU decomposition, different CPU cores cannot be perfectly load balanced and they also need some communication time. As the number of CPU cores increases, more communication time is needed and the load balance decreases. Although the efficiency is reduced, using more CPU cores is still faster.

$$\text{Parallel efficiency} = \frac{\text{Time used of 1 CPU core}}{p \times (\text{Time used of } p \text{ CPU core})} \quad (5.5)$$

**Table 5.2.** Comparison of the parallel time domain code for different number of CPU cores for a 2160-unknown problem.

Number of CPU cores	Total time of the simulation (sec)	Parallel efficiency
1	531.42	100%
2	270.68	98.16%
4	141.27	94.04%
8	77.05	86.21%
16	44.87	74.02%

Example 4 is similar to the third one. The only difference is that I used a finer mesh and a greater number of unknowns. In this example, I discretized the sphere into 3966 triangular patches and 5949 unknowns. The computation time and parallel efficiency are listed in Table 5.3. When compared to the previous example, I can see that the parallel efficiency is improved. Because there are more unknowns in this example,

the load balance is improved and the ratio of communication time comparing to the calculation time is also reduced. This comparison is also plotted in Figure 5.7.

**Table 5.3.** Comparison of the parallel time domain code for different number of CPU cores for a 5949-unknown problem.

Number of CPU cores	Total time of the simulation (sec)	Parallel efficiency
1	4007.2	100%
2	2009.0	99.73%
4	1013.6	98.84%
8	525.14	95.38%
16	281.63	88.93%

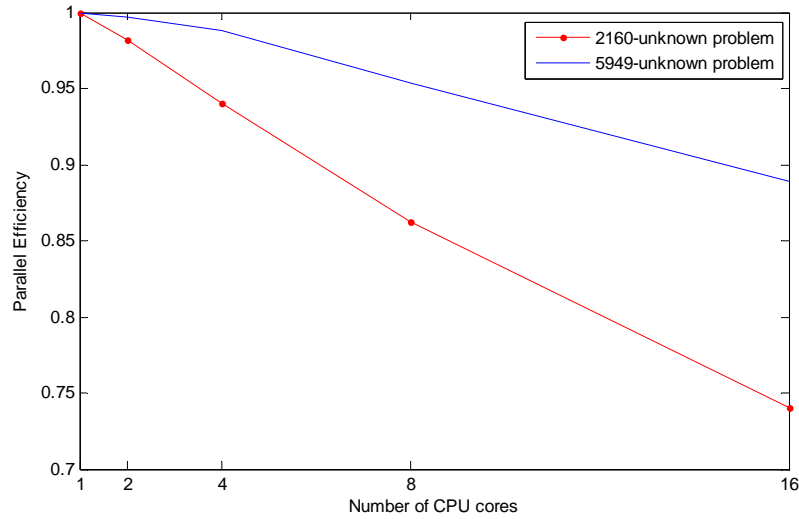


**Figure 5.7** The comparison of parallel efficiency for different number of unknowns

Example 5 is a Chevrolet Impala sedan with a monopole antenna on its roof, as shown in Figure 5.8. The size of the car is 5.09 m  $\times$  1.85 m  $\times$  1.50 m and the monopole is 0.21 m long. The monopole is excited by a generator with a Gaussian pulse voltage in the form of Eq. (5.6), in which  $t_0 = 10$  nanoseconds,  $\sigma = 2$  nanoseconds, and the bandwidth is 300 MHz. The  $z$  component of the far field to the  $-x$  direction, which is to the front of the car, is computed. I simplified the problem in this example by assuming that the whole vehicle is made of a perfect conductor. The vehicle is discretized into 15,300 triangular

patches and 22,952 unknowns. It was run on a Linux cluster with 32 CPU cores and the result is compared to the IDFT result from the frequency domain solver HOBBIES, as shown in Figure 5.9. The results match well.

$$V(t) = \exp\left(-\frac{(t-t_0)^2}{2\sigma^2}\right) \quad (5.6)$$

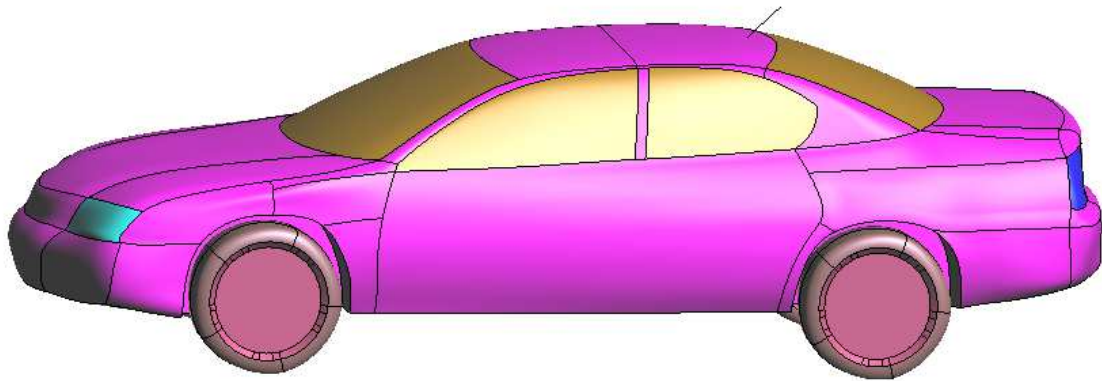


**Figure 5.8** A sedan with a monopole antenna on the roof.

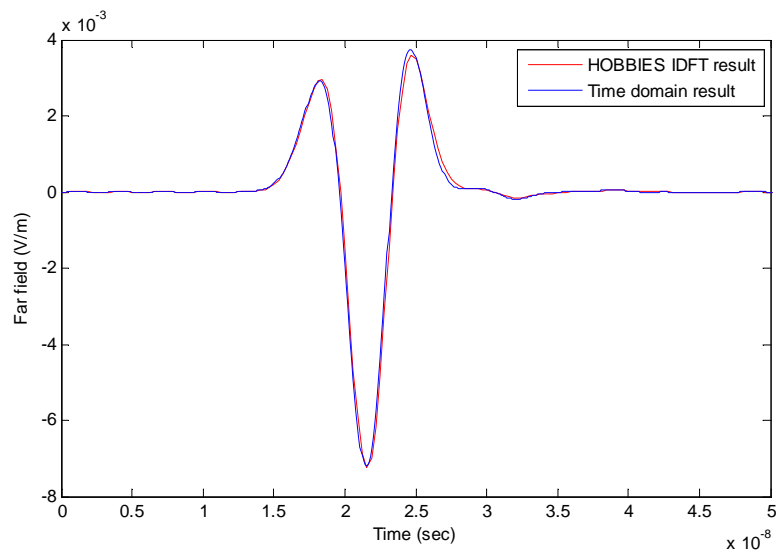


**Figure 5.9** Comparison of the far field result in time and frequency domain.

Example 6 is a dipole inside a dielectric sphere. The dipole is located at the center of the dielectric sphere and is placed along the  $z$  direction, as shown in Figure 5.10. The dipole is 0.1 meter long and the radius of the sphere is 0.5 meter. The dielectric constant of the sphere is  $\varepsilon = 2$ . The source is at the center of the dipole and provides a Gaussian pulse voltage, as shown in Eq. (5.6), in which  $t_0 = 10$  nanoseconds,  $\sigma = 2$  nanoseconds, and the bandwidth is 300 MHz. The sphere is discretized into 2128 triangular patches and the dipole is divided into 4 subsections. There is a total of 6390 unknowns. The  $z$  component of the far field to the  $+x$  direction is computed and is compared with an IDFT result from the frequency domain solver HOBBIES, as shown in Figure 5.11. This simulation was run on a Linux cluster with 20 CPU cores.

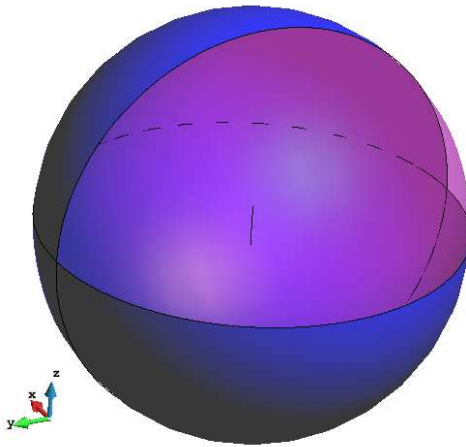


**Figure 5.10** A dipole inside a dielectric sphere.



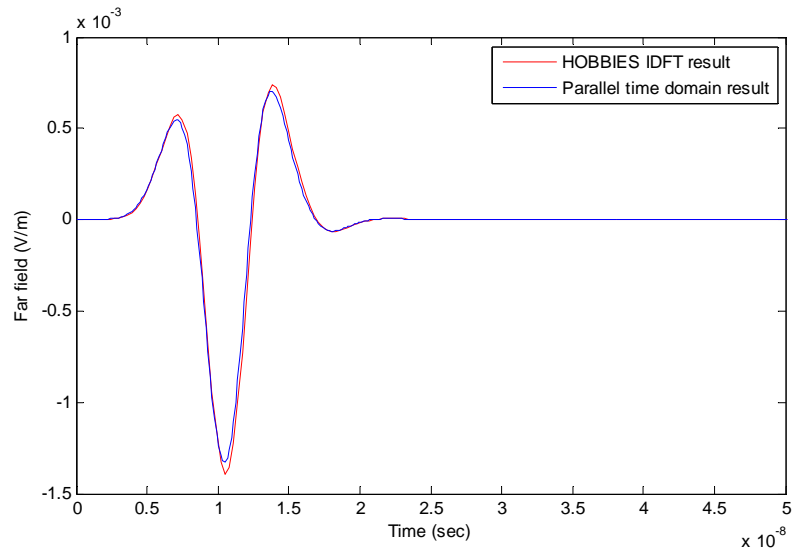


**Figure 5.11** Comparison the far field results in the time and frequency domain.

Parallelization is an accurate and efficient way of solving the time domain MoM problems of large scale. MPI and ScaLAPACK are used to solve the MoM problems. Numerical examples show that this parallelization method is efficient and accurate.



## **Chapter 6.**

# **A Hybrid Method of Moment and Physical Optics Method**

The method of moment (MoM) is a widely used technique for solving electromagnetic problems. However, as the size of the problem increases, the matrix size and the computation time increase as the square and cube of the unknown numbers, respectively. Therefore, substantial resources are needed to compute large objects and this is not affordable for many applications.

In many cases, these large objects are metallic and their surfaces are relatively smooth, so hybridization of MoM with asymptotic techniques is a reasonable approach.[33][34] The small objects are analyzed by MoM while the large and smooth surfaces are analyzed by asymptotic methods. Compared with the ray-based methods, the current-based physical optics (PO) method is preferred because the MoM is also a current-based method.[35][36] Many researchers have already used hybrid MoM-PO in frequency domain problems. [35]-[37]

In this chapter, I extend the hybrid MoM-PO method to the time domain MoM.

First, the problem is divided into two regions. One is the MoM region and the other is the PO region. The currents in the MoM region can be solved by electric field integral equations (EFIE) by assuming that the PO current is known. The PO current can

then be analyzed with the known MoM current. With this new PO current, the original MoM current can be updated. By repeating this iteration, a final result can be obtained.

Numerical examples are provided at the end of the chapter to verify the accuracy and the efficiency of this hybrid method. The numerical result shows that this iteration method converges very rapidly.

### 6.1 Solving the Current in the MoM Region by EFIE

Suppose that the current in the PO region is already known; the current in the MoM region can then be solved by EFIE. The boundary condition on the perfect electric conductor (PEC) MoM surface forces the tangential electric field to be zero, as shown in Eq. (6.1).

$$\left[-\mathbf{E}^{MoM}(\mathbf{r}, t)\right]_{\tan} = \left[\mathbf{E}^{incident}(\mathbf{r}, t) + \mathbf{E}^{PO}(\mathbf{r}, t)\right]_{\tan} \quad (6.1)$$

where  $\mathbf{E}^{incident}(\mathbf{r}, t)$ ,  $\mathbf{E}^{MoM}(\mathbf{r}, t)$ , and  $\mathbf{E}^{PO}(\mathbf{r}, t)$  denote the incident wave, the scattered wave from the MoM region, and the scattered wave from the PO region, respectively. The subscript *tan* implies the tangential components. The scattered wave can be obtained from the magnetic vector potential  $\mathbf{A}(\mathbf{r}, t)$  and the electric scalar potential  $\Phi(\mathbf{r}, t)$  as introduced in Chapter 2. and is expressed as (6.3).

$$\mathbf{E}^{MoM}(\mathbf{r}, t) = -\frac{\partial}{\partial t} \mathbf{A}^{MoM}(\mathbf{r}, t) - \nabla \Phi^{MoM}(\mathbf{r}, t) \quad (6.2)$$

$$\mathbf{E}^{PO}(\mathbf{r}, t) = -\frac{\partial}{\partial t} \mathbf{A}^{PO}(\mathbf{r}, t) - \nabla \Phi^{PO}(\mathbf{r}, t) \quad (6.3)$$

where  $\mathbf{A}$  and  $\Phi$  are the magnetic vector and the electric scalar potential, respectively.

As in the previous chapters, these two potentials can be expressed in current and charge density and then simplify by applying the Hertz vector potential  $\mathbf{u}(\mathbf{r}, t)$ . Similar to Eq. (2.7), the Eq. (6.1) can be changed to

$$\begin{aligned} & \left( \frac{\mu}{4\pi} \frac{\partial^2}{\partial t^2} \int_{S^{MoM}} \frac{\mathbf{u}^{MoM}(\mathbf{r}', \tau)}{R} dS' - \frac{\nabla}{4\pi\epsilon} \int_{S^{MoM}} \frac{\nabla' \cdot \mathbf{u}^{MoM}(\mathbf{r}', \tau)}{R} dS' \right)_{\tan} \\ & = \left( \mathbf{E}^i(\mathbf{r}, t) \right)_{\tan} - \left( \frac{\mu}{4\pi} \frac{\partial^2}{\partial t^2} \int_{S^{PO}} \frac{\mathbf{u}^{PO}(\mathbf{r}', \tau)}{R} dS' - \frac{\nabla}{4\pi\epsilon} \int_{S^{PO}} \frac{\nabla' \cdot \mathbf{u}^{PO}(\mathbf{r}', \tau)}{R} dS' \right)_{\tan} \end{aligned} \quad (6.4)$$

The Hertz potential  $\mathbf{u}(\mathbf{r}, t)$  is then expanded using spatial and temporal basis functions.

$$\mathbf{u}(\mathbf{r}, t) = \sum_{n=1}^N u_n(t) \mathbf{f}_n(\mathbf{r}) \quad (6.5)$$

$$u_n(t) = \sum_{j=0}^{\infty} u_{n,j} (\phi_j(st) - 2\phi_{j+1}(st) + \phi_{j+2}(st)) \quad (6.6)$$

where  $\mathbf{f}_n(\mathbf{r})$  is the spatial basis function, and  $\phi_j(st)$  is associated Laguerre function.

By substituting Eq. (6.5) and (6.6) into Eq. (6.4), the scattered waves from the MoM and PO region in Eq. (1) are then expressed in terms of these basis functions as

$$\left[ \begin{aligned} & \frac{\mu}{4\pi} \frac{s^2}{4} \sum_{n=1}^{N_{MoM}} \int_S \frac{\sum_{j=0}^{\infty} \phi_j(s\tau) [u_{n,j}^{MoM} + 2u_{n,j-1}^{MoM} + u_{n,j-2}^{MoM}] \mathbf{f}_n^{MoM}(\mathbf{r}')}{R} dS' - \\ & \frac{1}{4\pi\epsilon} \nabla \sum_{n=1}^{N_{MoM}} \int_S \frac{\sum_{j=0}^{\infty} \phi_j(s\tau) [u_{n,j}^{MoM} - 2u_{n,j-1}^{MoM} + u_{n,j-2}^{MoM}] \nabla' \cdot \mathbf{f}_n^{MoM}(\mathbf{r}')}{R} dS' \end{aligned} \right]_{\tan}$$

$$\begin{aligned}
& \mathbf{E}^i(\mathbf{r}, t) - \\
= & \left[ \begin{aligned} & \frac{\mu}{4\pi} \frac{s^2}{4} \sum_{n=1}^{N_{PO}} \int_S \frac{\sum_{j=0}^{\infty} \phi_j(s\tau) [u_{n,j}^{PO} + 2u_{n,j-1}^{PO} + u_{n,j-2}^{PO}] \mathbf{f}_n^{PO}(\mathbf{r}')}{R} dS' + \\ & \frac{1}{4\pi\epsilon} \nabla \sum_{n=1}^{N_{PO}} \int_S \frac{\sum_{j=0}^{\infty} \phi_j(s\tau) [u_{n,j}^{PO} - 2u_{n,j-1}^{PO} + u_{n,j-2}^{PO}] \nabla' \cdot \mathbf{f}_n^{PO}(\mathbf{r}')}{R} dS' \end{aligned} \right]_{\tan} \quad (6.7)
\end{aligned}$$

where  $N_{MoM}$  and  $N_{PO}$  are the number of spatial basis number.

Temporal testing is then applied by inner production with  $\phi_i(st)$  and spatial testing is then applied by inner production with  $\mathbf{f}_m^{MoM}(\mathbf{r})$ . One can obtain Eq. (6.8)

$$\begin{aligned}
& \left[ \begin{aligned} & \frac{\mu s^2}{4} \sum_{n=1}^{N_{MoM}} \sum_{j=0}^i a_{mnij}^{MoM} [u_{n,j}^{MoM} + 2u_{n,j-1}^{MoM} + u_{n,j-2}^{MoM}] \\ & + \frac{1}{\epsilon} \sum_{n=1}^{N_{MoM}} \sum_{j=0}^i b_{mnij}^{MoM} [u_{n,j}^{MoM} - 2u_{n,j-1}^{MoM} + u_{n,j-2}^{MoM}] \end{aligned} \right] = \\
& \left[ \begin{aligned} & \Omega_{m,i}^{E\_incident} - \frac{\mu s^2}{4} \sum_{n=1}^{N_{PO}} \sum_{j=0}^i a_{mnij}^{PO} [u_{n,j}^{PO} + 2u_{n,j-1}^{PO} + u_{n,j-2}^{PO}] \\ & - \frac{1}{\epsilon} \sum_{n=1}^{N_{PO}} \sum_{j=0}^i b_{mnij}^{PO} [u_{n,j}^{PO} - 2u_{n,j-1}^{PO} + u_{n,j-2}^{PO}] \end{aligned} \right] \quad (6.8)
\end{aligned}$$

where

$$a_{mnij}^{MoM} = \int_S \mathbf{f}_m^{MoM}(\mathbf{r}) \cdot \int_{S'} \frac{I_{ij}(sR/c)}{4\pi R} \mathbf{f}_n^{MoM}(\mathbf{r}') dS' dS \quad (6.9)$$

$$b_{mnij}^{MoM} = \int_S \nabla \cdot \mathbf{f}_m^{MoM}(\mathbf{r}) \int_{S'} \frac{I_{ij}(sR/c)}{4\pi R} \nabla' \cdot \mathbf{f}_n^{MoM}(\mathbf{r}') dS' dS \quad (6.10)$$

$$a_{mnij}^{PO} = \int_S \mathbf{f}_m^{MoM}(\mathbf{r}) \cdot \int_{S'} \frac{I_{ij}(sR/c)}{4\pi R} \mathbf{f}_n^{PO}(\mathbf{r}') dS' dS \quad (6.11)$$

$$b_{mnij}^{PO} = \int_S \nabla \cdot \mathbf{f}_m^{MoM}(\mathbf{r}) \int_{S'} \frac{I_{ij}(sR/c)}{4\pi R} \nabla' \cdot \mathbf{f}_n^{PO}(\mathbf{r}') dS' dS \quad (6.12)$$

$$\Omega_{m,i}^{E\_incident} = \int_S \mathbf{f}_m^{MoM}(\mathbf{r}) \cdot \mathbf{V}_E^{incident}(\mathbf{r}) dS \quad (6.13)$$

$$\mathbf{V}_E^{incident}(\mathbf{r}) = \int_0^\infty \phi_i(st) \mathbf{E}^{incident}(\mathbf{r}, t) d(st) \quad (6.14)$$

$$I_{ij}(sR/c) = \int_{sR/c}^\infty \phi_i(st) \phi_j(st - sR/c) d(st) = \begin{cases} 0 & j > i \\ e^{(-sR/(2c))} & j = i \\ e^{(-sR/(2c))} (L_{i-j}(sR/c) - L_{i-j-1}(sR/c)) & j < i \end{cases} \quad (6.15)$$

In Eq. (6.8), the upper limit of the summation over  $j$  in the  $a_{mnij}$  and  $b_{mnij}$  terms is replaced by  $i$  instead of  $\infty$  because the integral  $I_{ij}(sR/c)$  equals 0 when  $j > i$ .

Finally, the above equations can be written in a form that is amenable to the MOD method by moving all the terms associated with  $c_{n,i}^{MoM}$  to the left hand side and the terms associated with  $u_{n,j}^{MoM}$  ( $j < i$ ) to the right hand side. Once the coefficients  $u_{n,j}^{MoM}$  ( $j=0,1,2,\dots,i-1$ ) are evaluated, the unknown coefficient of the next degree  $u_{n,i}^{MoM}$  can easily be accomplished, as shown in Eq. (6.16). Once the unknown in the PO rations and the unknown less than  $i$ -th degree in the MoM region are known, the unknown of degree  $i$  in the MoM region can be computed with this equation.

$$\begin{aligned}
& \left[ \begin{aligned} & \frac{\mu S^2}{4} \sum_{n=1}^{N_{MoM}} a_{mnii}^{MoM} [u_{n,j}^{MoM} + 2u_{n,j-1}^{MoM} + u_{n,j-2}^{MoM}] \\ & + \frac{1}{\epsilon} \sum_{n=1}^{N_{MoM}} b_{mnii}^{MoM} [u_{n,j}^{MoM} - 2u_{n,j-1}^{MoM} + u_{n,j-2}^{MoM}] \end{aligned} \right] = \\
& \left[ \begin{aligned} & \Omega_{m,i}^{E\_incident} - \frac{\mu S^2}{4} \sum_{n=1}^{N_{PO}} \sum_{j=0}^i a_{mnij}^{PO} [u_{n,j}^{PO} + 2u_{n,j-1}^{PO} + u_{n,j-2}^{PO}] \\ & - \frac{1}{\epsilon} \sum_{n=1}^{N_{PO}} \sum_{j=0}^i b_{mnij}^{PO} [u_{n,j}^{PO} - 2u_{n,j-1}^{PO} + u_{n,j-2}^{PO}] \end{aligned} \right] \tag{6.16} \\
& - \left[ \begin{aligned} & \frac{\mu S^2}{4} \sum_{n=1}^{N_{MoM}} \sum_{j=0}^{i-1} a_{mnij}^{MoM} [u_{n,j}^{MoM} + 2u_{n,j-1}^{MoM} + u_{n,j-2}^{MoM}] \\ & + \frac{1}{\epsilon} \sum_{n=1}^{N_{MoM}} \sum_{j=0}^{i-1} b_{mnij}^{MoM} [u_{n,j}^{MoM} - 2u_{n,j-1}^{MoM} + u_{n,j-2}^{MoM}] \end{aligned} \right]
\end{aligned}$$

## 6.2 Solving the Current in the PO Region

If the current in the MoM region is already known, the current over the PEC PO region is given by the boundary condition of Eq. (6.17). In the PO region, the mutual interaction with PO current at other positions is neglected. The total magnetic field can be substituted by two times of the wave incident to the PO surface at the lit region  $S_{lit}$  and 0 in the shadowed region  $S_{shadow}$ .

$$\mathbf{J}^{PO}(\mathbf{r}, t) = \hat{\mathbf{n}} \times \mathbf{H}(\mathbf{r}, t) \tag{6.17}$$

$$\mathbf{J}^{PO}(\mathbf{r}, t) = \begin{cases} 2\hat{\mathbf{n}} \times (\mathbf{H}^{incident}(\mathbf{r}, t) + \mathbf{H}^{MoM}(\mathbf{r}, t)) & \mathbf{r} \in S_{lit} \\ 0 & \mathbf{r} \in S_{shadow} \end{cases} \tag{6.18}$$

where  $\mathbf{H}^{incident}$  is the incident magnetic field and the  $\mathbf{H}^{MoM}$  is the scattered field from the MoM current.



As in the previous chapters, Eq. (6.18) can be analyzed with Hertz vector potential.

$$\begin{aligned} & \sum_{n=1}^{N_{PO}} \sum_{j=0}^{\infty} \frac{s}{2} \phi_j(st) [u_{n,j}^{PO} - u_{n,j-2}^{PO}] \mathbf{f}_n^{PO}(\mathbf{r}) = \\ & 2\hat{\mathbf{n}} \times \left( \mathbf{H}^{incident}(\mathbf{r}, t) + \int_S \nabla \times \frac{\mathbf{J}^{MoM}(\mathbf{r}', \tau)}{4\pi R} dS \right) \end{aligned} \quad (6.19)$$

The curl in Eq. (6.19) can be analyzed by Eq. (6.20). [38]

$$\nabla \times \frac{\mathbf{J}(\mathbf{r}', \tau)}{R} = \frac{1}{c} \frac{\partial}{\partial t} \mathbf{J}(\mathbf{r}', \tau) \times \frac{\hat{\mathbf{R}}}{R} + \mathbf{J}(\mathbf{r}', \tau) \times \frac{\hat{\mathbf{R}}}{R^2} \quad (6.20)$$

The equation then becomes

$$\begin{aligned} & \sum_{n=1}^{N_{PO}} \sum_{j=0}^{\infty} \frac{s}{2} \phi_j(st) [u_{n,j}^{PO} - u_{n,j-2}^{PO}] \mathbf{f}_n^{PO}(\mathbf{r}) = 2\hat{\mathbf{n}} \times \mathbf{H}^{incident}(\mathbf{r}, t) + \\ & 2\hat{\mathbf{n}} \times \sum_{n=1}^{N_{MoM}} \int_S \left( \frac{1}{c} \frac{s^2}{4} \sum_{j=0}^{\infty} \phi_j(s\tau) [u_{n,j}^{MoM} + 2u_{n,j-1}^{MoM} + u_{n,j-2}^{MoM}] \mathbf{f}_n^{MoM}(\mathbf{r}) \times \frac{\hat{\mathbf{R}}}{4\pi R} + \right. \\ & \left. \sum_{j=0}^{\infty} \frac{s}{2} \phi_j(s\tau) [u_{n,j}^{MoM} - u_{n,j-2}^{MoM}] \mathbf{f}_n^{MoM}(\mathbf{r}) \times \frac{\hat{\mathbf{R}}}{4\pi R^2} \right) dS' \end{aligned} \quad (6.21)$$

The temporal testing is applied by inner production with  $\phi_i(st)$  and then the spatial testing is applied by inner production with  $\mathbf{f}_m^{PO}(\mathbf{r})$ . For the reason that no mutual interaction is assumed to occur in the PO region, the inner product of the two different spatial basis functions is zero. One can obtain Eq. (6.22).

$$\frac{S}{2}[u_{n,i}^{PO} - u_{n,i-2}^{PO}]\Gamma_n = 2\Omega_{n,i}^{H\_incident} + 2\sum_{m=1}^N \left( \frac{1}{c} \frac{S^2}{4} \sum_{j=0}^i c_{mnij}^{PO} [u_{m,j}^{MoM} + 2u_{m,j-1}^{MoM} + u_{m,j-2}^{MoM}] + \sum_{j=0}^i \frac{S}{2} d_{mnij}^{PO} [u_{m,j}^{MoM} - u_{m,j-2}^{MoM}] \right) \quad (6.22)$$

where

$$c_{mnij}^{PO} = \int_S \mathbf{f}_m^{PO}(\mathbf{r}) \cdot \int_{S'} \frac{I_{ij}(sR/c)}{4\pi R} \hat{\mathbf{n}} \times \mathbf{f}_n^{MoM}(\mathbf{r}') \times \hat{\mathbf{R}} dS' dS \quad (6.23)$$

$$c_{mnij}^{PO} = \int_S \mathbf{f}_m^{PO}(\mathbf{r}) \cdot \int_{S'} \frac{I_{ij}(sR/c)}{4\pi R} \hat{\mathbf{n}} \times \mathbf{f}_n^{MoM}(\mathbf{r}') \times \hat{\mathbf{R}} dS' dS \quad (6.24)$$

$$d_{mnij}^{PO} = \int_S \mathbf{f}_m^{PO}(\mathbf{r}) \cdot \int_{S'} \frac{I_{ij}(sR/c)}{4\pi R^2} \hat{\mathbf{n}} \times \mathbf{f}_n^{MoM}(\mathbf{r}') \times \hat{\mathbf{R}} dS' dS \quad (6.25)$$

$$\Omega_{n,i}^{H\_incident} = \int_S \mathbf{f}_n^{PO}(\mathbf{r}) \cdot \hat{\mathbf{n}} \times \mathbf{V}_H^{incident}(\mathbf{r}) dS \quad (6.26)$$

$$\mathbf{V}_H^{incident}(\mathbf{r}) = \int_0^\infty \phi_i(st) \mathbf{H}^{incident}(\mathbf{r}, t) d(st) \quad (6.27)$$

$$\Gamma_n = \int_S |\mathbf{f}_n^{PO}(\mathbf{r})|^2 dS \quad (6.28)$$

The Eq. (6.22) can also be solved by a MOD method. After the coefficients  $u_{n,j}^{PO}$  ( $j=0,1,2,\dots,i-1$ ) are calculated, the unknown coefficient of the next degree  $u_{n,j}^{PO}$  can easily be obtained without solving matrix equations.

### 6.3 Solve the Hybrid MoM-PO Problem Iteratively

The hybrid MoM-PO problem can be analyzed by an iterative method.

1. First let the initial guess of the PO unknown coefficients to be zero.

$$u_{n,i}^{PO(0)} = 0$$

2. The MoM unknown coefficients of the  $k$ -th iteration  $u_{n,i}^{MoM(k)}$  can be evaluated by substituting the PO coefficients of last iteration  $u_{n,i}^{PO(k-1)}$  into Eq. (6.16).

3. The PO unknown coefficients of the  $k$ -th iteration  $u_{n,i}^{PO(k)}$  can be evaluated by substituting the MoM coefficients of last iteration  $u_{n,i}^{MoM(k)}$  into Eq. (6.22).

4. If not converged, goto step 2.

These steps can also be expressed by Eq. (6.29) and Figure 6.1.

$$\mathbf{E}_{(0)}^{PO}(\mathbf{r}, t) = 0 \quad (6.29)\text{-a}$$

$$\left[ -\mathbf{E}_{(1)}^{MoM}(\mathbf{r}, t) \right]_{\tan} = \left[ \mathbf{E}^{incident}(\mathbf{r}, t) + \mathbf{E}_{(0)}^{PO}(\mathbf{r}, t) \right]_{\tan} \quad (6.29)\text{-b}$$

$$\left[ -\mathbf{E}_{(1)}^{PO}(\mathbf{r}, t) \right]_{\tan} = \left[ \mathbf{E}^{incident}(\mathbf{r}, t) + \mathbf{E}_{(1)}^{MoM}(\mathbf{r}, t) \right]_{\tan} \quad (6.29)\text{-c}$$

$$\left[ -\mathbf{E}_{(2)}^{MoM}(\mathbf{r}, t) \right]_{\tan} = \left[ \mathbf{E}^{incident}(\mathbf{r}, t) + \mathbf{E}_{(1)}^{PO}(\mathbf{r}, t) \right]_{\tan} \quad (6.29)\text{-d}$$

$$\left[ -\mathbf{E}_{(2)}^{PO}(\mathbf{r}, t) \right]_{\tan} = \left[ \mathbf{E}^{incident}(\mathbf{r}, t) + \mathbf{E}_{(2)}^{MoM}(\mathbf{r}, t) \right]_{\tan} \quad (6.29)\text{-e}$$

...

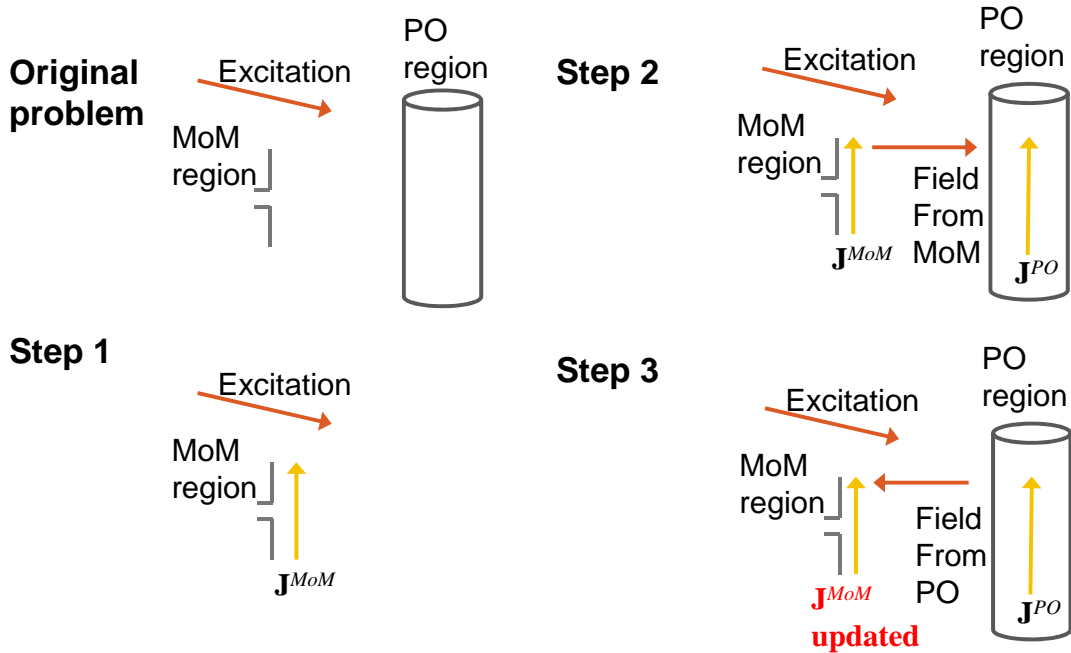


**Figure 6.1.** The iterative method for analyzing a hybrid MoM-PO problem.

## 6.4 Numerical Examples

Numerical examples are presented to illustrate the versatility of this method. In this section, all the structures are excited using a T-pulse, which was introduced in Section 3.6.1. A T-pulse is a strictly time-limited pulse with most of its energy concentrated in a narrow band. Hence, the waveform by definition is causal.

Example 1 deals with the transient electromagnetic radiation from a 1 meter long dipole and a PEC circular plate with a 3 meter radius placed 2 meters away, as shown in Figure 6.2. The axis of the dipole is placed along the  $x$ -axis. The dipole is divided into 10 subsections and a piecewise triangular basis function is applied, which is expressed as  $\mathbf{f}_n^\pm(\mathbf{r}) = \pm \mathbf{l}_n^\pm / \Delta l_n^\pm$  ( $\mathbf{r} \in L_n^\pm$ ). [39] The PEC plate is divided into 3292 triangles and 4813 RWG basis functions are applied. The dipole is divided into an MoM region and the plate

is divided into a PO region. The duration of the T-pulse that the dipole radiates is 7 lm, as shown in Figure 6.3. The unit lm is a light-meter, which is 3.33 nanoseconds, and equals the time taken by light to travel one meter. Most of the energy is concentrated in the frequency band from 0 to 150 MHz, and only less than 0.0003% of the energy is outside this band, as shown in Figure 6.4. The voltage is fed at the center of the dipole, the highest Laguerre degree is chosen as 150, and the scaling factor  $s = 10^9$ .

The far field at the direction of  $\theta = \varphi = 0^\circ$  is plotted in Figure 6.5 and the direction of  $\theta = 90^\circ, \varphi = 0^\circ$  is plotted in Figure 6.6. The numbers of iterations are one to five, respectively. Figure 6.5 shows that the backscattered far field of an MoM-PO with only one iteration differs significantly from the MoM method but the rest of them agree well with the results generated by only the MoM technique. In Figure 6.6, which is the front scattered far field, the MoM-PO results do not agree well with the MoM result. The convergence of this method is measured by defining a variable  $\Delta^{(k)}$  to measure the change of the coefficients in the  $k$ -th iteration in Eq. (6.30). The values of  $\Delta^{(k)}$  in all iterations are listed in Table 6.1. The rate of convergence is so very fast that the numerical results are identical in the 4-th and 5-th iteration in a double precision program. Compared to the MoM method, this method has advantages both in computation time and memory by reducing the size of the matrix. These differences are listed in Table 6.2, and this particular problem shows that the computation time is reduced by 209 times and the memory used is reduced by 100 times.

$$\Delta^{(k)} = \frac{\sum_{n,j} |c_{n,j}^{PO(k)} - c_{n,j}^{PO(k-1)}|^2 + \sum_{n,j} |c_{n,j}^{MoM(k)} - c_{n,j}^{MoM(k-1)}|^2}{\sum_{n,j} |c_{n,j}^{PO(k)}|^2 + \sum_{n,j} |c_{n,j}^{MoM(k)}|^2} \quad (6.30)$$

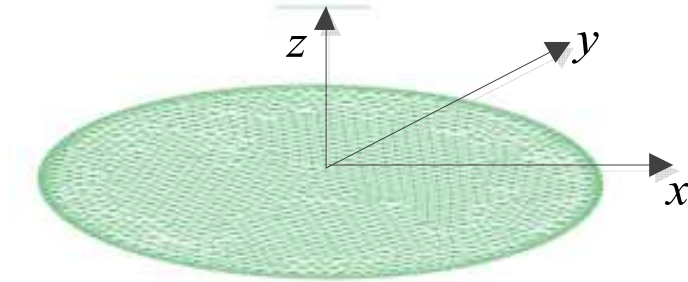


**Figure 6.2.** A dipole and a plate reflector

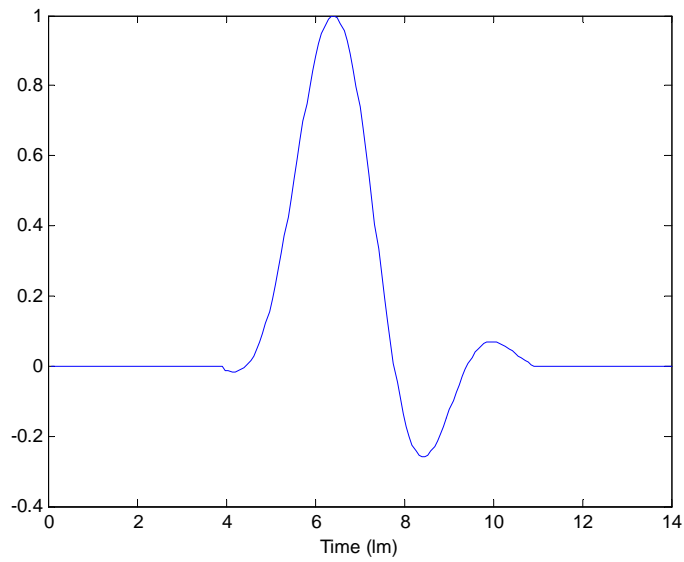


**Figure 6.3.** The T-pulse fed into the dipole

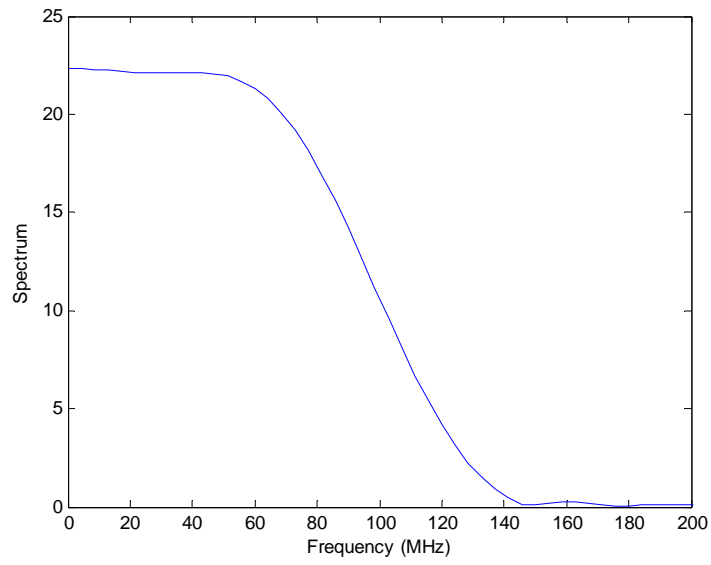


**Figure 6.4.** The spectrum of the T-pulse fed into the dipole

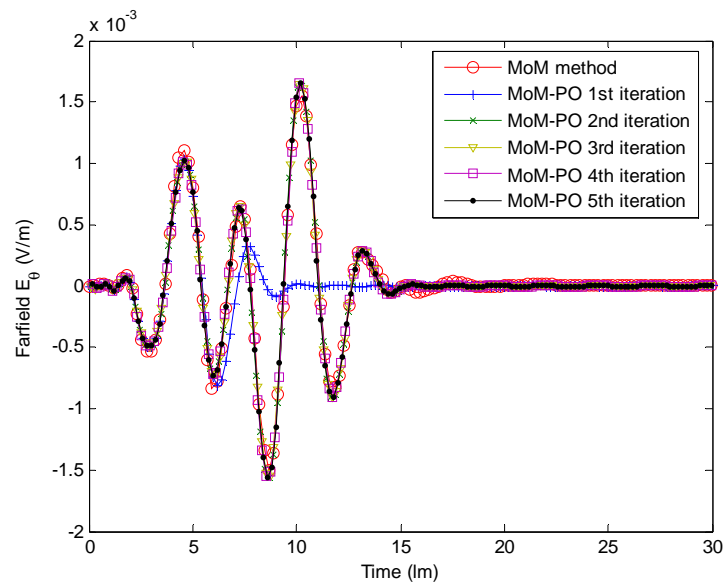


**Figure 6.5.** The far field radiated at the direction of direction of  $\theta = \varphi = 0^\circ$ .

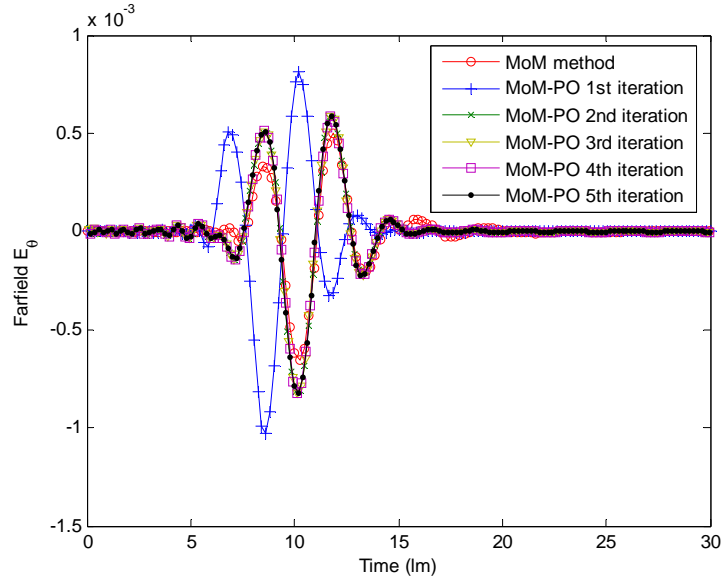


**Figure 6.6.** The far field radiated at the direction of direction of  $\theta = 90^\circ, \varphi = 0^\circ$ .

**Table 6.1.** Convergence test of different iterations.

Iteration $k$	$\Delta^{(k)}$
1	---
2	0.6701
3	1.5757e-008
4	3.9437e-015
5	0.0000e+000

**Table 6.2.** Reduction in memory usage and computation time.

Iteration $k$	MoM	MoM-PO
MoM unknown number	4822	9
PO unknown number	0	4813
Memory used	904 MB	9 MB
Computation time	3.19 days	22 min (5 iterations)

Example 2 deals with a Boeing 737 plane with a dimension of  $26 \text{ m} \times 26 \text{ m} \times 11 \text{ m}$ . A  $z$ -polarized 0.1 meter dipole is mounted on top of the plane. Its center is located at



(-5, 0, 3.4), as shown in Figure 6.7. The MoM region contains only this dipole with 5 unknowns and the PO region contains the body of the plane with 7327 unknowns. A T-pulse with duration of 10 ns and a bandwidth of 100MHz is radiated by the dipole. The voltage is fed at the center of the dipole, the highest Laguerre degree is chosen as 100, and the scaling factor  $s = 10^9$ . The current over the surface of the plane is plotted in Figure 6.8. The values of the current for all the time instants have been scaled. The darkest (blue) color is defined as 0 A/m while the lightest (red) color is used for all currents larger than  $2 \times 10^{-6}$  A/m. The current is seen to move from the front to the rear in these figures.

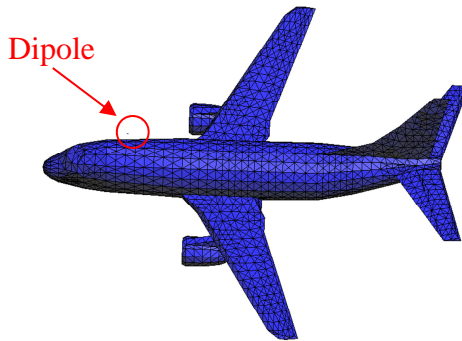
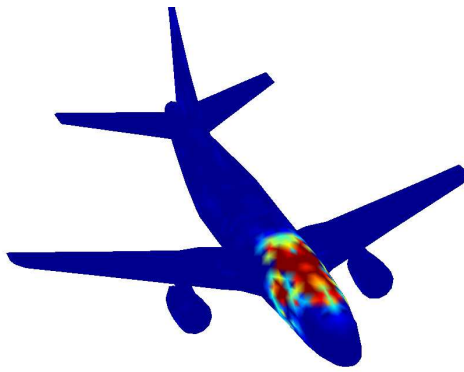


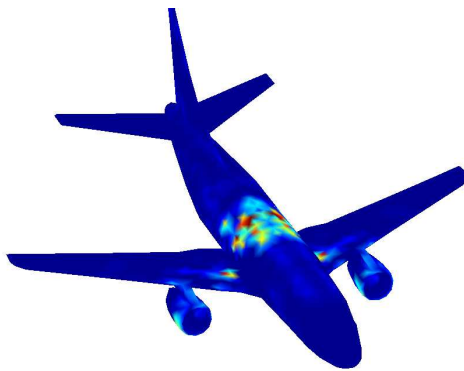
**Figure 6.7.** A dipole over a Boeing 737 plane



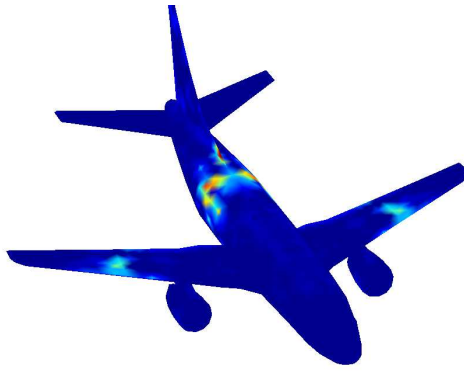
(a)  $t = 10 \text{ lm}$



(b)  $t = 14 \text{ lm}$



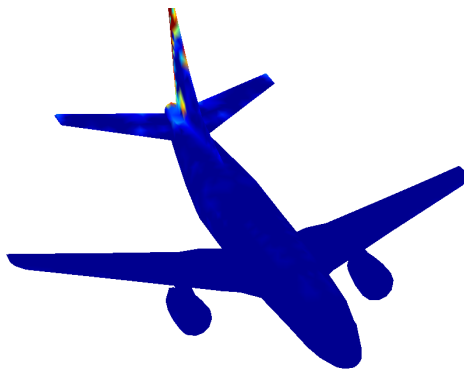
(c)  $t = 18 \text{ lm}$



(d)  $t = 22 \text{ lm}$



(e)  $t = 26 \text{ lm}$



(f)  $t = 30 \text{ lm}$

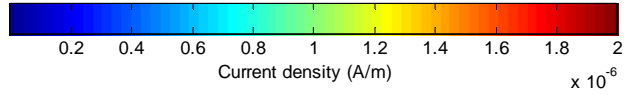


**Figure 6.8.** Transient current density distribution on the Boeing aircraft.

## 6.5 Conclusion

A hybrid MoM-PO method in the time domain is presented for transient analysis of electromagnetic scattering from electrically large structures. This hybrid method is computationally efficient as only a very few iterations are required for the numerical convergence of the results. Sample numerical results are presented to illustrate the versatility of this method.

## Appendix A.

### The Laguerre Function and Related Integrals

The definition and properties of Laguerre polynomials are listed in this appendix.

*Definition:*

Consider the following set of functions [29],

$$L_j(t) = \frac{e^t}{j!} \frac{d^j}{dt^j} (t^j e^{-t}), \quad 0 \leq t < \infty, \quad j = 0, 1, 2, \dots \quad (\text{A.1})$$

These are the Laguerre polynomials of degree  $j$ . They are causal; i.e., they are defined for  $t \geq 0$ . They can be computed through a stable recursive procedure and obtained as

$$L_0(t) = 1 \quad (\text{A.2})$$

$$L_1(t) = 1 - t \quad (\text{A.3})$$

$$L_j(t) = \frac{1}{j} \left( (2j-1-t)L_{j-1}(t) - (j-1)L_{j-2}(t) \right) \quad (\text{A.4})$$

Some main properties that are used in the temporal procedures are briefly described in the following.

*Orthogonality:*

The Laguerre functions are orthogonal as

$$\int_0^{\infty} e^{-t} L_i(t) L_j(t) dt = \delta_{ij} = \begin{cases} 1, & i = j \\ 0, & i \neq j \end{cases} \quad (\text{A.5})$$

*Laguerre Transform:*

A causal time-dependent function  $f(t)$  for  $t \geq 0$  can be expanded as

$$f(t) = \sum_{j=0}^{\infty} f_j \phi_j(t) \quad (\text{A.6})$$

where  $\phi_j(t)$  is the associated Laguerre function defined in Eq. (2.17). Based on the orthogonal property given by Eq. (A.5), the multiplication of the function  $f(t)$  with  $\phi_j(t)$  and integrating from zero to infinity, yields

$$\int_0^{\infty} \phi_i(t) f(t) dt = f_i \quad (\text{A.7})$$

The expression in Eq. (A.7) is called the Laguerre transform.

*Derivative:*

Using the Laguerre transform, an analytic representation for the time derivative of the function  $f(t)$  can be obtained as

$$\int_0^{\infty} \phi_i(t) \frac{d}{dt} f(t) dt = \frac{1}{2} f_i + \sum_{k=0}^{i-1} f_k \quad (\text{A.8})$$

where  $f(0) = 0$  is assumed and  $\phi_i(\infty) = 0$  is used.

Using the relation Eqs. (A.5)-(A.8), the derivative of the function  $f(t)$  can be expanded as

$$\frac{d}{dt} f(t) = \sum_{j=0}^{\infty} \left( \frac{1}{2} f_j + \sum_{k=0}^{j-1} f_k \right) \phi_j(t) \quad (\text{A.9})$$

Similarly, the result for the second derivative of the function  $f(t)$  is given as

$$\frac{d^2}{dt^2} f(t) = \sum_{j=0}^{\infty} \left[ \left( \frac{1}{4} f_j + \sum_{k=0}^{j-1} (j-k) f_k \right) \right] \phi_j(t) \quad (\text{A.10})$$

*Integral:*

Consider an integral given as

$$I_{ij}(y) = \int_0^{\infty} \phi_i(x) \phi_j(x-y) dx \quad (\text{A.11})$$

Through a change of variable  $z = x - y$ , and substituting the expression of  $\phi_j(t)$  given by Eq. (2.17), Eq. (A.11) yields

$$I_{ij}(y) = e^{-y/2} \int_{-y}^{\infty} e^{-z} L_i(z+y) L_j(z) dz \quad (\text{A.12})$$

Using the properties of Laguerre polynomials of Eqs. (8.971) and (8.974) in [29], one obtains

$$L_i(z+y) = \sum_{k=0}^i L_k(z) (L_{i-k}(y) - L_{i-k-1}(y)) \quad (\text{A.13})$$

Substituting Eq. (A.13) into Eq. (A.12), one obtains

$$I_{ij}(y) = e^{-y/2} \sum_{k=0}^i (L_{i-k}(y) - L_{i-k-1}(y)) \int_{-y}^{\infty} e^{-z} L_k(z) L_j(z) dz \quad (\text{A.14})$$

Because the Laguerre polynomial is defined for  $z \geq 0$ , the lower limit of the integral in Eq. (A.14) may be changed from  $-y$  to zero. Moreover, Eq. (A.14) can be computed by using the orthogonal property given by Eq. (A.5) and yields the integral of associated Laguerre functions as

$$\int_0^{\infty} \phi_i(x) \phi_j(x-y) dx = \begin{cases} e^{-y/2} (L_{i-j}(y) - L_{i-j-1}(y)), & j \leq i \\ 0, & j > i \end{cases} \quad (\text{A.15})$$



## Appendix B. The Singularity of the Surface Integrals

In the spatial integral, the Green's function has singular values when the distance is zero. For the wires, the current is assumed to distribute at the surface and the integral is performed along the axis to avoid singularity. However, for patches, a solution must be found to solve the integral of the singular points.

In the EFIE, the integrals that involve singularities are given by Eqs. (2.26) – (2.29) and they are rewritten here as Eqs. (B.1) – (B.4).

$$A_{mij} = \int_S \mathbf{f}_m(\mathbf{r}) \cdot \int_{S'} \frac{I_{ij}(sR/c)}{4\pi R} \mathbf{f}_n(\mathbf{r}') dS' dS \quad i \neq j \quad (\text{B.1})$$

$$B_{mij} = \int_S \nabla \cdot \mathbf{f}_m(\mathbf{r}) \int_{S'} \frac{I_{ij}(sR/c)}{4\pi R} \nabla' \cdot \mathbf{f}_n(\mathbf{r}') dS' dS \quad i \neq j \quad (\text{B.2})$$

$$\alpha_{mn} = \int_S \mathbf{f}_m(\mathbf{r}) \cdot \int_{S'} \frac{e^{(-sR/(2c))}}{4\pi R} \mathbf{f}_n(\mathbf{r}') dS' dS \quad (\text{B.3})$$

$$\beta_{mn} = \int_S \nabla \cdot \mathbf{f}_m(\mathbf{r}) \int_{S'} \frac{e^{(-sR/(2c))}}{4\pi R} \nabla' \cdot \mathbf{f}_n(\mathbf{r}') dS' dS \quad (\text{B.4})$$

For the first two integrals (B.1) and (B.2), their integral kernel can be expressed as

$$\frac{I_{ij}(sR/c)}{R} = \frac{e^{\frac{sR}{2c}} \left[ L_{i-j}(sR/c) - L_{i-j-1}(sR/c) \right]}{R}. \quad (\text{B.5})$$

When  $R$  approaches zero, the limit can be obtained by applying L'Hôpital's rule.

$$\lim_{R \rightarrow 0} \frac{I_{ij}(sR/c)}{R} = \frac{\partial}{\partial R} \left( e^{\frac{sR}{2c}} \left[ L_{i-j}(sR/c) - L_{i-j-1}(sR/c) \right] \right) = -\frac{s}{c}. \quad (\text{B.6})$$

Therefore, the integral of this integral kernel does not contain any singularity and the computation is straightforward.

For the term of next two equations (B.3) – (B.4), the kernel of the integrals is  $e^{(-sR/(2c))} / R$ , which can be expressed by two terms, as shown in Eq. (B.7). The second term has no singularities and can be analyzed by L'Hôpital's rule.

$$\frac{e^{(-sR/(2c))}}{R} = \frac{1}{R} + \frac{e^{(-sR/(2c))} - 1}{R} \quad (\text{B.7})$$

For the first term, this results in two integrals

$$I_1 = \int_S \mathbf{f}_m(\mathbf{r}) \cdot \int_{S'} \frac{\mathbf{f}_n(\mathbf{r}')}{4\pi R} dS' dS \quad (\text{B.8})$$

$$I_2 = \int_S \nabla_r \cdot \mathbf{f}_m(\mathbf{r}) \int_{S'} \frac{1}{4\pi R} \nabla_{r'} \cdot \mathbf{f}_n(\mathbf{r}') dS' dS \quad (\text{B.9})$$

The  $\nabla_r \cdot \mathbf{f}_m(\mathbf{r})$  and  $\nabla_{r'} \cdot \mathbf{f}_n(\mathbf{r}')$  are constants in the RWG basis, as shown in Eq.

(2.15). The second integral that needs to be handled is  $I_b(\mathbf{r}) = \int_{S'} \frac{1}{R} dS'$ . It can be

analytically calculated as shown in Dr. S. M. Rao's thesis [2].

In the  $I_1$  term, the integral that needs to be handled is  $\mathbf{I}_a(\mathbf{r}) = \int_{S'} \frac{\mathbf{f}_n(\mathbf{r}')}{R} dS'$ . Let a triangle be defined in the form in Figure B.1.

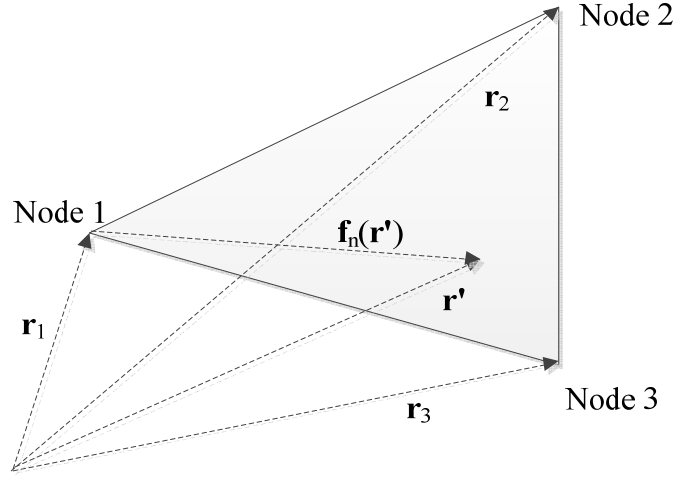


**Figure B.1** Geometric of the RWG basis function.

The basis  $\mathbf{f}_n(\mathbf{r}')$  is a difference between two vectors,  $\mathbf{f}_n(\mathbf{r}') = \mathbf{r}' - \mathbf{r}_1$ . The  $\mathbf{r}'$  can also be expressed in terms of the vector of the nodes of the triangle.

$$\mathbf{r}' = (1 - \xi - \eta)\mathbf{r}_1 + \xi\mathbf{r}_2 + \eta\mathbf{r}_3, \quad 0 < \xi < 1, 0 < \eta < 1, 0 < (1 - \xi - \eta) < 1 \quad (\text{B.10})$$

Therefore, the integral of  $\mathbf{I}_a(\mathbf{r})$  can be calculated.

$$\begin{aligned} \mathbf{I}_a(\mathbf{r}) &= \int_{S'} \frac{\mathbf{F}_n(\mathbf{r}')}{R} dS' \\ &= \int_{S'} \frac{(-\xi - \eta)\mathbf{r}_1 + \xi\mathbf{r}_2 + \eta\mathbf{r}_3}{R} dS' \\ &= (\mathbf{r}_2 - \mathbf{r}_1) \int_{S'} \frac{\xi}{R} dS' + (\mathbf{r}_3 - \mathbf{r}_1) \int_{S'} \frac{\eta}{R} dS' \end{aligned} \quad (\text{B.11})$$

The integral of  $\int_{S'} \frac{\xi}{R} dS'$  and  $\int_{S'} \frac{\eta}{R} dS'$  can be handled analytically in [2]. The final integral is

$$\underbrace{\int_S \mathbf{F}_m(\mathbf{r}) \cdot \underbrace{\int_{S'} \frac{\mathbf{F}_n(\mathbf{r}')}{R} dS'}_{\text{calculate analytically}}}_{\text{calculate numerically}} dS \quad (\text{B.12})$$

For the PMCHW equations, the integrals involve singularities are given in Eqs. (4.32),(4.33), (4.36), and (4.37). They are now rewritten here.

$$C_{mnij}^v = \int_S \mathbf{f}_m(\mathbf{r}) \cdot \int_S \frac{1}{4\pi} I_{ij}\left(s \frac{R}{c_v}\right) \mathbf{f}_n(\mathbf{r}') \times \frac{\hat{\mathbf{R}}}{R} dS' dS \quad (\text{B.13})$$

$$D_{mnij}^v = \int_S \mathbf{f}_m(\mathbf{r}) \cdot \int_S \frac{1}{4\pi} I_{ij}\left(s \frac{R}{c_v}\right) \mathbf{f}_n(\mathbf{r}') \times \frac{\hat{\mathbf{R}}}{R^2} dS' dS \quad (\text{B.14})$$

$$\gamma_{mn}^v = C_{mnij}^v \Big|_{j=i} = \int_S \mathbf{f}_m(\mathbf{r}) \cdot \int_S \frac{1}{4\pi} e^{\left(-\frac{sR}{2c_v}\right)} \mathbf{f}_n(\mathbf{r}') \times \frac{\hat{\mathbf{R}}}{R} dS' dS \quad (\text{B.15})$$

$$\chi_{mn}^v = D_{mnij}^v \Big|_{j=i} = \int_S \mathbf{f}_m(\mathbf{r}) \cdot \int_S \frac{1}{4\pi} e^{\left(-\frac{sR}{2c_v}\right)} \mathbf{f}_n(\mathbf{r}') \times \frac{\hat{\mathbf{R}}}{R^2} dS' dS \quad (\text{B.16})$$

For the RWG basis function, when  $\mathbf{f}_m(\mathbf{r})$  and  $\mathbf{f}_n(\mathbf{r}')$  are on the same triangular patch,  $\mathbf{f}_m(\mathbf{r}) \cdot (\mathbf{f}_n(\mathbf{r}') \times \hat{\mathbf{R}}) = 0$ .

# Appendix C. The Choice of Scaling Factor

## C.1 Introduction

In the marching-on-in-degree time domain method of moment, the transient responses are expanded by a finite number of associated Laguerre functions. There is an error associated with truncating the associated Laguerre function series beyond that which is necessary for the solution process. This error is related to the scaling factor used in the argument of the associated Laguerre functions that actually approximate the unknown temporal variations. In this section, a least upper bound of this error is deduced. Based on this bound, one can obtain an optimum scaling factor to minimize this error so that it is guaranteed to be below a certain bound.

The associated Laguerre function is defined as

$$\phi_k(st) = e^{-\frac{st}{2}} L_k(st) \quad (\text{C.1})$$

where  $s$  is a scaling factor and  $L_k(st)$  is the Laguerre polynomial of the  $k$ -th degree. The scaling factor  $s$  is needed because the duration of a transient process usually depends on the type of problem and it can vary widely from nanoseconds to several hundreds of nanoseconds. If no scaling factor is incorporated, the value of the associated Laguerre function is very close to  $L_k(0)$  and it is not suitable for expansion of the transient responses.

Theoretically speaking, any time domain function can be expanded using the associated Laguerre functions with a set of infinite degrees. However, for practical

reasons, one can only use a finite number of degrees to expand a function, as illustrated by

$$f(t) \approx \sum_{k=0}^{n-1} c_k \phi_k(st) \quad (\text{C.2})$$

where  $f(t)$  is an arbitrary transient function and  $c_k$  is the coefficient for degree  $k$ . Making a finite sum with  $n$  terms instead of infinite terms results in an approximation error. This error is related to two factors: one is related to the highest degree  $n-1$  used and the other is the scaling factor  $s$ .

In control areas, researchers also use Laguerre polynomials to expand their transient signals of interest. Several papers have been presented related to the optimum choice for the value of the scaling factor [30]–[32]. However, the Laguerre functions they used in the control area are different from the associated Laguerre functions that have been used in the computational electromagnetics; thus, their conclusions cannot be applied to my work.

This section shows that the error resulting from an inappropriate choice of the scaling factor has a least upper bound and this bound is a function of the scaling factor. Therefore, appropriate choice of the scaling factor can minimize the least upper bound of the error.

## **C.2 Development of the Least Upper Bound**

The development of the least upper bound can be achieved by the following steps:

1. Find a second order differential equation that is satisfied by the associated Laguerre functions used in time domain MoM.

2. Introduce two lemmas needed for finding the upper bound.

3. Obtain an upper bound using the lemmas of the previous step.

4. Show that the upper bound is the least upper bound.

First of all, a second order differential equation must be found that the associated Laguerre function  $\phi_k(st)$  satisfies. The Laguerre polynomials used in this thesis satisfy the following differential equation: [19]

$$st \frac{\partial^2}{\partial(st)^2} L_k(st) + (1-st) \frac{\partial}{\partial(st)} L_k(st) + k L_k(st) = 0 \quad (C.3)$$

From the definition in Eq. (C.1), the first and second derivative of the associated Laguerre function is given by

$$\frac{\partial}{\partial(st)} \phi_k(st) = -\frac{e^{-\frac{st}{2}}}{2} L_k(st) + e^{-\frac{st}{2}} \frac{\partial}{\partial(st)} L_k(st) \quad (C.4)$$

$$\frac{\partial^2}{\partial(st)^2} \phi_k(st) = \frac{e^{-\frac{st}{2}}}{4} L_k(st) - e^{-\frac{st}{2}} \frac{\partial}{\partial(st)} L_k(st) + e^{-\frac{st}{2}} \frac{\partial^2}{\partial(st)^2} L_k(st) \quad (C.5)$$

Adding Eq. (C.4) to Eq. (C.5) and multiplying by  $st$  yields

$$\begin{aligned}
& st \frac{\partial^2}{\partial(st)^2} \phi_k(st) + \frac{\partial}{\partial(st)} \phi_k(st) \\
&= e^{-\frac{st}{2}} \left( st \frac{\partial^2}{\partial(st)^2} L_k(st) + (1-st) \frac{\partial}{\partial(st)} L_k(st) \right) + \frac{st}{4} e^{-\frac{st}{2}} L_k(st) - \frac{1}{2} e^{-\frac{st}{2}} L_k(st)
\end{aligned} \tag{C.6}$$

Observe that the terms in the large brackets are the first two terms of Eq. (C.3), and by applying Eq. (C.3) to Eq. (C.6), one obtains

$$st \frac{\partial^2}{\partial(st)^2} \phi_k(st) + \frac{\partial}{\partial(st)} \phi_k(st) = \left( -k + \frac{st}{4} - \frac{1}{2} \right) \phi_k(st) \tag{C.7}$$

Eq. (C.7) displays the differential equation satisfied by the associated Laguerre functions used in the marching-on-in-degree solution procedure.

By changing  $\frac{\partial}{\partial(st)}$  into  $\frac{1}{s} \frac{\partial}{\partial t}$  in Eq. (C.7), one obtains

$$t \frac{\partial^2}{\partial t^2} \phi_k(st) + \frac{\partial}{\partial t} \phi_k(st) - \frac{s^2 t}{4} \phi_k(st) = s \left( -k - \frac{1}{2} \right) \phi_k(st) \tag{C.8}$$

Eq. (C.8) is a second order differential equation that the associated Laguerre functions satisfy.

In the next step, two lemmas are given. Let

$$f(t) = \sum_{k=0}^{\infty} c_k \phi_k(st) \tag{C.9}$$

Define two measures  $m_1$  and  $m_2$ , given by



$$m_1 = \frac{1}{\|f\|^2} \int_0^\infty t f^2(t) dt \quad (\text{C.10})$$

$$m_2 = \frac{1}{\|f\|^2} \int_0^\infty t \left( \frac{d}{dt} f(t) \right)^2 dt \quad (\text{C.11})$$

in which,  $\|f\|^2 = \int_0^\infty f^2(t) dt = \frac{1}{s} \sum_{k=0}^\infty c_k^2$ .

Definition of **Lemma 1**: For a function  $\|f\|^2 < +\infty$ ,

$$\frac{s^2}{4} m_1 + m_2 = \frac{1}{\|f\|^2} \sum_{k=0}^\infty c_k^2 \left( k + \frac{1}{2} \right) \quad (\text{C.12})$$

**Proof of Lemma 1:**

$$\begin{aligned} \int_0^{+\infty} t \left( \frac{\partial}{\partial t} f(t) \right)^2 dt &= \int_0^{+\infty} t \frac{\partial}{\partial t} f(t) df(t) \\ &= t \left( \frac{\partial}{\partial t} f(t) \right) f(t) \Big|_0^{+\infty} - \int_0^{+\infty} f(t) d \left( t \frac{\partial}{\partial t} f(t) \right) \\ &= - \int_0^{+\infty} f(t) \left( \frac{\partial}{\partial t} f(t) + t \frac{\partial^2}{\partial t^2} f(t) \right) dt \end{aligned} \quad (\text{C.13})$$

Expand  $f(t)$  using the associated Laguerre functions by applying Eq. (C.9) and then apply the relationship of the second order differential equation given by Eq. (C.8), resulting in:

$$\begin{aligned}
\int_0^{+\infty} t \left( \frac{\partial}{\partial t} f(t) \right)^2 dt &= - \int_0^{+\infty} f(t) \sum_{k=0}^{\infty} c_k \left( \frac{\partial}{\partial t} \phi_k(st) + t \frac{\partial^2}{\partial t^2} \phi_k(st) \right) dt \\
&= -s \int_0^{+\infty} f(t) \sum_{k=0}^{\infty} c_k \left( -k + \frac{st}{4} - \frac{1}{2} \right) \phi_k(st) dt
\end{aligned} \tag{C.14}$$

Then  $\frac{s^2}{4} m_1 + m_2$  can be evaluated from Eq. (C.14) and using the orthogonal

property of the associated Laguerre functions result in:

$$\begin{aligned}
\frac{s^2}{4} m_1 + m_2 &= \frac{1}{\|f\|^2} \int_0^{+\infty} \frac{s^2 t f^2(t)}{4} + t \left( \frac{d}{dt} f(t) \right)^2 dt \\
&= \frac{1}{\|f\|^2} \int_0^{+\infty} f(t) \sum_{k=0}^{\infty} c_k s \left( k + \frac{1}{2} \right) \phi_k(st) dt \\
&= \frac{1}{\|f\|^2} \sum_{k=0}^{\infty} c_k^2 \left( k + \frac{1}{2} \right)
\end{aligned} \tag{C.15}$$

End of the proof of **Lemma 1**.

For the function expanded by the associated Laguerre functions with degrees lower than  $n$ , the error  $\varepsilon_n^2$  is defined as

$$\varepsilon_n^2 = \frac{1}{\|f\|^2} \int_0^{\infty} \left( f(t) - \sum_{k=0}^{n-1} c_k \phi_k(st) \right)^2 dt = \frac{1}{s \|f\|^2} \sum_{k=n}^{\infty} c_k^2 \tag{C.16}$$

From the conclusion of Lemma 1, another conclusion given by Lemma 2 can be obtained as follows.

**Definition of Lemma 2:** For the functions belonging to the set

$$C = \left\{ \begin{array}{l} f : \frac{1}{\|f\|^2} \int_0^\infty t f^2(t) dt = m_1, \\ \frac{1}{\|f\|^2} \int_0^\infty t \left( \frac{d}{dt} f(t) \right)^2 dt = m_2 \end{array} \right\}, \quad (\text{C.17})$$

$$\max_{f \in C} \varepsilon_n^2 \leq \frac{s^2 m_1 + 4m_2 - 2s}{4sn} \quad (\text{C.18})$$

Proof of **Lemma 2**:

From the conclusions of Lemma 1, one has

$$\sum_{k=0}^{\infty} c_k^2 \left( k + \frac{1}{2} \right) = \|f\|^2 \left( \frac{s^2}{4} m_1 + m_2 \right) \quad (\text{C.19})$$

$$n \sum_{k=n}^{\infty} c_k^2 \leq \|f\|^2 \left( \frac{s^2}{4} m_1 + m_2 \right) - \frac{1}{2} \sum_{k=0}^{\infty} c_k^2 \quad (\text{C.20})$$

$$n \sum_{k=n}^{\infty} c_k^2 \leq \|f\|^2 \left( \frac{s^2}{4} m_1 + m_2 - \frac{s}{2} \right) \quad (\text{C.21})$$

Therefore, when  $\|f\|^2 \neq 0$ , using Eq. (C.21) the error is given by

$$\varepsilon_n^2 = \frac{1}{s \|f\|^2} \sum_{k=n}^{\infty} c_k^2 \leq \frac{s^2 m_1 + 4m_2 - 2s}{4sn} \quad (\text{C.22})$$

End of the proof of **Lemma 2**.

The upper bound of the error is then given by Lemma 2. The final step is to show that this upper bound is the least upper bound. This can be verified by finding a function

that can reach this upper bound. Therefore, this is the least upper bound. One can find such a function  $f(t)$  defined by

$$f(t) = c_0 \phi_0(st) + c_n \phi_n(st) \quad (\text{C.23})$$

$$c_0^2 + c_n^2 = 1 \quad (\text{C.24})$$

Let  $f(t)$  be expanded by the associated Laguerre functions with degrees lower than  $n$ . So the expansion of  $f(t)$  misses the second term and result in an error given by

$$\mathcal{E}_n^2 = c_n^2 \quad (\text{C.25})$$

The measure  $m_1$  is then given by

$$m_1 = \frac{1}{\|f\|^2} \int_0^\infty t f^2(t) dt = \frac{c_n^2}{s} (2n+1) + \frac{c_0^2}{s} \quad (\text{C.26})$$

Proof of Eq. (C.26):

Substituting the definition of  $f(t)$  in Eq. (C.23) to  $m_1$ .

$$\begin{aligned} m_1 &= \frac{1}{\|f\|^2} \int_0^\infty t f^2(t) dt \\ &= s \int_0^\infty t c_n^2 \phi_n^2(st) dt + s \int_0^\infty t c_0^2 \phi_0^2(st) dt \\ &\quad + 2s \int_0^\infty t c_0 c_n \phi_0(st) \phi_n(st) dt \end{aligned} \quad (\text{C.27})$$

The first term in Eq. (C.27) is evaluated by

$$\begin{aligned}
s \int_0^\infty t c_n^2 \phi_n^2(st) dt &= \frac{c_n^2}{s} \int_0^\infty s t e^{-st} \left( L_n(st) \right)^2 d(st) \\
&= \frac{c_n^2}{s} \int_0^\infty x e^{-x} \left( L_n^{(1)}(x) - L_{n-1}^{(1)}(x) \right)^2 dx \\
&= \frac{c_n^2}{s} \int_0^\infty x e^{-x} \left( L_n^{(1)}(x) \right)^2 dx + \frac{c_n^2}{s} \int_0^\infty x e^{-x} \left( L_{n-1}^{(1)}(x) \right)^2 dx \\
&= \frac{c_n^2}{s} (2n+1)
\end{aligned} \tag{C.28}$$

where  $L_n^{(1)}(x)$  is called the generalized Laguerre polynomial or associated Laguerre polynomial. The second term of Eq. (C.27) can be evaluated using a similar method.

$$s \int_0^\infty t c_0^2 \phi_0^2(st) dt = \frac{c_0^2}{s} \tag{C.29}$$

Orthogonality can be applied to find the last term of Eq. (C.27).

$$\begin{aligned}
s \int_0^\infty t c_0 c_n \phi_0(st) \phi_n(st) dt &= \frac{c_0 c_n}{s} \int_0^\infty e^{-st} s t L_n(st) d(st) \\
&= \frac{c_0 c_n}{s} \int_0^\infty e^{-st} (1 - (1-st)) L_n(st) d(st) \\
&= \frac{c_0 c_n}{s} \int_0^\infty e^{-st} \left( L_0(st) - L_1(st) \right) L_n(st) d(st) \\
&= 0
\end{aligned} \tag{C.30}$$

Substitute Eq. (C.28), (C.29), and (C.30) into Eq. (C.27), and the result presented in Eq. (C.26) can be obtained.

End of proof of in Eq. (C.26).

Applying Lemma 1,  $m_2$  is given by

$$\frac{s^2}{4}m_1 + m_2 = s\left(\frac{1}{2}c_0^2 + \frac{2n+1}{2}c_n^2\right) \quad (\text{C.31})$$

Change  $c_0^2$  and  $c_n^2$  in terms of  $\varepsilon_n^2$  by applying Eq. (C.23), (C.24), and (C.25) to (C.26) and (C.31). This results in

$$\varepsilon_n^2 = \frac{s^2m_1 + 4m_2 - 2s}{4sn} \quad (\text{C.32})$$

Eq. (C.32) indicates that the error for the function  $f(t)$  can reach the upper bound given by Lemma 2. Therefore, this upper bound is the least upper bound.

### **C.3 Optimum Scaling Factor in Sense of the Least Upper Bound**

In the previous section, the least upper bound of the error for expanding a function with a finite number of associated Laguerre functions is obtained. This bound is a function of the scaling factor  $s$  and depends on the highest degree  $n$  of the expansion. Therefore, the error can be reduced in two ways: one is to increase the degree of the expansion and the other is to choose the scaling factor properly to reduce the bound of the error. This is achieved by taking the derivative of the right-hand side of Eq. (C.18) with respect to  $s$  and equating that to zero. Under this condition, the value for the optimum scaling factor is given by

$$s_{opt} = \sqrt{4m_2 / m_1} \quad (\text{C.33})$$

The least upper bound of the error can be minimized.

Please note that this optimum scaling factor is in the sense of minimizing the least upper bound of the error. It does not give the minimum error, but provides a guideline on

how to choose the scaling factor for an arbitrary transient function and guarantees that the error is not larger than a bound. The numerical examples show that although the optimum scaling factor does not guarantee a minimum error for all the degrees, the errors are not very large compared to the other scaling factors and converge to zero quite rapidly. The error of the optimum scaling factor is acceptable and what is more important, for an arbitrary transient function, a scientific method exists to calculate it and the error is guaranteed to be less than this bound.

#### C.4 Examples

The first example illustrates that the upper bound can be reached and it is the least upper bound. This example also shows that the optimum scaling is only in the sense of obtaining a minimum least upper bound but not the least error.

Example 1: For a function  $f(t) = \phi_5(s_0 t) - \phi_{20}(s_0 t)$ , in which  $s_0 = 10^9$ , the optimum scaling factor  $s$  to expand this function is  $s_{\text{opt}} = 9.9093 \times 10^8$ . Figure C.1 plots the least upper bound when  $s = s_{\text{opt}}$  and the associated errors when using different scaling factor  $s$ . As shown in the figure, the error of  $s = s_{\text{opt}}$  is not greater than the least upper bound and it reaches the bound for one particular degree while all other scaling factors have some error greater than this bound. This verifies that the bound in this example is the least upper bound and that  $s_{\text{opt}}$  is the optimum scaling factor. The figure also shows that when  $10 < n < 20$ , other scaling factors can obtain a smaller error. Therefore, the optimum scaling here is only in the sense of minimizing the least upper bound but does not guarantee that it can reach the least error for any degree.

The next example applies the optimum scaling factor to a Gaussian pulse, which is widely used in time domain analyses. This example displays the errors associated with different scaling factors and the optimum scaling factor that can reduce the error to zero at an acceptable rate.

Example 2: Here a Gaussian pulse is defined by

$$f(t) = \exp\left(-\frac{(t-\mu)^2}{2\sigma^2}\right) \quad (\text{C.34})$$

where  $\mu = 20$  nanoseconds and  $\sigma = 2$  nanoseconds. The optimum scaling factor found by this method is  $s_{\text{opt}} = 7.0680 \times 10^8$ . In Figure C.2, the errors associated with different scaling factors are plotted. This figure shows that the error of the optimum scaling factor decreases very fast and converges to zero around an order of 80. Although some other scaling factors converge faster than this, the optimum scaling factor does converge at an acceptable rate.



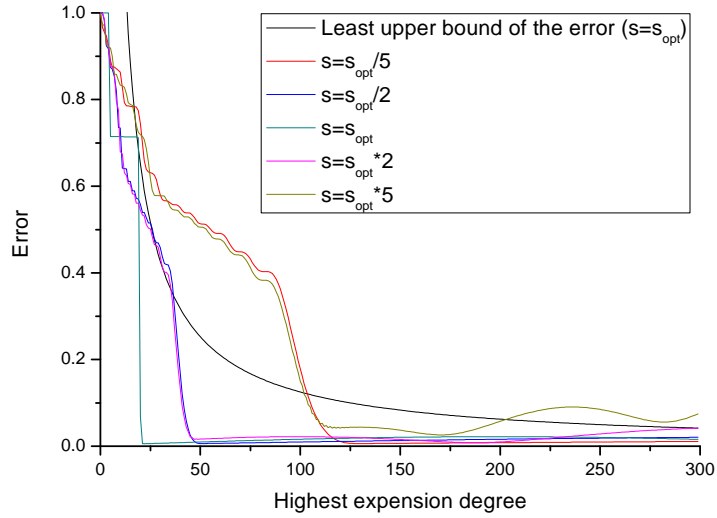


**Figure C.1** The least upper bound and the error for different scaling factor for the pulse given in Example 1

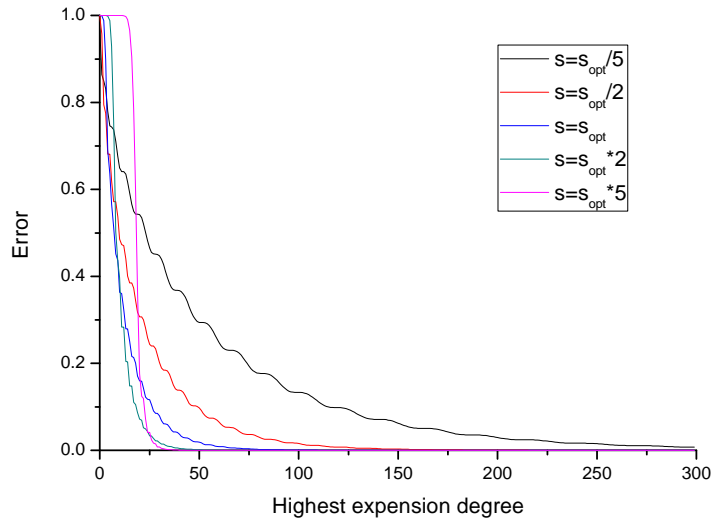


**Figure C.2** The error for different scaling factor for the pulse shown in Example 2.

### C.5 Conclusion

Expanding a function with associated Laguerre functions gives rise to an error that results from using a finite number of degrees. This error depends on the scaling

factor and the highest degree of the basis function. This appendix showed how to find an optimum scaling factor so that the least upper bound of this error is minimized for an arbitrary function. Therefore, the error is smaller than a bound that decreases when the highest degree increases. Although it does not guarantee that the error is minimum for every degree by comparing to other scaling factors, numerical examples show that the error is acceptable and converges to zero very rapidly.

# Appendix D. Numerical Accuracy for MOD

## Integrals

### D.1 Introduction

The Marching-on-in-degree (MOD) solver based on a Galerkin implementation of the MoM reveals that the matrix to be inverted contains integrals that are similar to the ones encountered in a frequency domain MoM solver using the same basis functions. The error in the evaluation of the matrix elements involving these integrals is also observed to be larger in the time domain than those involved in the frequency domain MoM solvers. The objective of this appendix is to explain this dichotomy and how to improve upon the accuracy when using the triangular patch basis functions (RWG) for both the time and the frequency domain techniques. When the distance between the two triangular patches involved in the evaluation of the matrix elements are close to each other, or when the degree of the Laguerre polynomial in a MOD method is high, the integral accuracy is compromised and the number of sampling points to evaluate the integrals needs to be increased.

In the MOD method, the unknown variables, such as the current or the potential functions related to the integral equation associated with the problem of interest, are expanded by a set of both spatial and temporal basis functions. The spatial basis functions are generally chosen as the piecewise triangle (RWG) functions, whereas the temporal basis functions are chosen as the associated Laguerre functions in this thesis. In a Galerkin time domain methodology in the MoM context, the time variable is analytically

integrated out. Consequently, the final equations that are used in the computations contain only the spatial variables. In this context, the expressions for the matrix elements look very similar to the expressions used in a frequency domain MoM problem using the same triangular patch basis. The interesting feature is that even though the expressions for the matrix elements over the spatial basis functions are similar both in the time and in the frequency domain, the Green's functions involved are different. Due to a difference in the Green's functions, the matrix elements for the time domain problem need to be evaluated more accurately than its frequency domain counterpart, using an increased number of quadrature sampling points for integration.

## D.2 Difference in Greens' Function Terms

In the MOD method, the spatial integrals involved in the evaluation of the expressions for the matrix elements are in the form of Eqs. (2.28) and (2.29). These two equations are represented here.

$$A_{mnab}^{TD} = \frac{1}{4\pi} \int_S \mathbf{f}_m(\mathbf{r}) \cdot \int_S \frac{1}{R} I_{ab}(sR/c) \mathbf{f}_n(\mathbf{r}') dS' dS \quad (\text{D.1})$$

$$B_{mnab}^{TD} = \frac{1}{4\pi} \int_S \nabla \cdot \mathbf{f}_m(\mathbf{r}) \int_S \frac{1}{R} I_{ab}(sR/c) \nabla' \cdot \mathbf{f}_n(\mathbf{r}') dS' dS \quad (\text{D.2})$$

In the frequency domain MoM [2][38], the spatial integrals are defined in the form of

$$A_{mn}^{FD} = \frac{1}{4\pi} \int_S \mathbf{f}_m(\mathbf{r}) \cdot \int_S \frac{1}{R} e^{-jkR} \mathbf{f}_n(\mathbf{r}') dS' dS \quad (\text{D.3})$$

$$B_{mn}^{FD} = \frac{1}{4\pi} \int_S \nabla \cdot \mathbf{f}_m(\mathbf{r}) \int_S \frac{1}{R} e^{-jkR} \nabla' \cdot \mathbf{f}_n(\mathbf{r}') dS' dS \quad (\text{D.4})$$

where  $j$  is the imaginary unit and  $k$  is the wave number.

The equations of Eqs. (D.1) – (D.4) differ only in the Green's function. For the MOD method, the Green's function is  $G_{TD} = I_{ab}(sR/c)/R$  and for the frequency domain method it is  $G_{FD} = e^{-jkR}/R$ .

The derivatives of these two Green's functions with respect to  $R$  can be obtained as

$$\frac{\partial G_{TD}}{\partial R} = -\frac{1}{R^2} I_{ab}(sR/c) + \frac{-s}{2cR} e^{(-sR/(2c))} \left( L_{a-b}(sR/c) + L_{a-b-1}(sR/c) \right) \quad (b < a) \quad (\text{D.5})$$

$$\frac{\partial G_{FD}}{\partial R} = -\frac{1}{R^2} e^{-jkR} - \frac{jk}{R} e^{-jkR} \quad (\text{D.6})$$

The ratio between the spatial derivatives of the Green's functions with respect to the Green's functions are also calculated as

$$\left| \frac{\partial G_{TD}}{\partial R} / G_{TD} \right| = \left| \frac{1}{R} + \frac{s}{2c} \frac{L_{a-b}(sR/c) + L_{a-b-1}(sR/c)}{L_{a-b}(sR/c) - L_{a-b-1}(sR/c)} \right| \quad (\text{D.7})$$

$$\left| \frac{\partial G_{FD}}{\partial R} / G_{FD} \right| = \sqrt{\frac{1}{R^2} + k^2} \quad (\text{D.8})$$

Eq. (D.8) is a monotonically decaying function with respect to the spatial variables and it does not have any singularities in the domain  $R \in (0, +\infty)$ . However, for Eq. (D.7), the denominator term  $L_{a-b}(sR/c) - L_{a-b-1}(sR/c)$  does have zeroes in the

domain  $R \in (0, +\infty)$  when  $b < a$ . Therefore, Eq. (D.7) has some singularities in this region.

Consider a very small error  $\Delta R$  associated with the evaluation of the spatial variable  $R$ , and that the result is in an error in the value of the Green's function,  $\Delta G_{TD}$ . The error  $\Delta G_{TD}$  is given by

$$\Delta G_{TD/FD} = \Delta R \times \frac{\partial G_{TD/FD}}{\partial R} \quad (\text{D.9})$$

The corresponding relative error is given by

$$\left| \frac{\Delta G_{TD/FD}}{G_{TD/FD}} \right| = \Delta R \times \left| \frac{\partial G_{TD/FD}}{\partial R} / G_{TD/FD} \right| \quad (\text{D.10})$$

When the value of  $R$  is such that the denominator of (D.7) is close to zero, the Green's function has a pole. A very small error in  $R$  can then result in a large relative error in the value of the Green's function. In conclusion, the Green's function encountered in the MOD method is more sensitive to the error in the evaluation of  $R$ . Generally, the integrals encountered in (D.1) – (D.4) for both time domain and frequency domain problems cannot be handled analytically for most of patches and a numerical technique needs to be employed to evaluate them over the surfaces involved. In the time domain, the functions associated with the integrals have singularities; therefore, more sampling points need to be used in the evaluation of the integrals than in the frequency domain. Consequently, in the evaluation of the integrals in Eq. (D.1) and (D.2), one needs more sampling points in the evaluation of the Green's function than in the frequency domain in order to maintain similar accuracy in the final results.

A plot of the two Green's functions for time and frequency domain is displayed in Figure D.1 and Figure D.2. For the time domain Green's function in Figure D.1,  $s$  is chosen as  $5 \times 10^9$  and the degree ( $a - b$ ) is 50 and 150, respectively, which are common values for most practical problems. For the frequency domain Green's function in Figure D.2,  $k$  is chosen as  $2\pi$ . Figure D.1 and Figure D.2 show that the time domain Green's function in Figure D.1 oscillates more than the frequency domain one, especially when  $R$  is small or the degree ( $a - b$ ) is high. Therefore, when  $R$  has a small error, the time domain Green's function gives a larger computational error than the other when using the same number of sample points to evaluate the integrals. Numerical examples in the evaluation of Eqs. (D.1) – (D.4) are used to illustrate the same point.

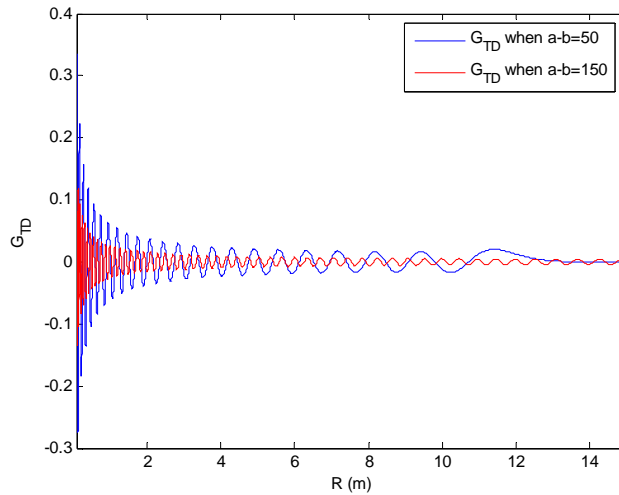


**Figure D.1** The time domain Green's function  $G_{TD}$ .

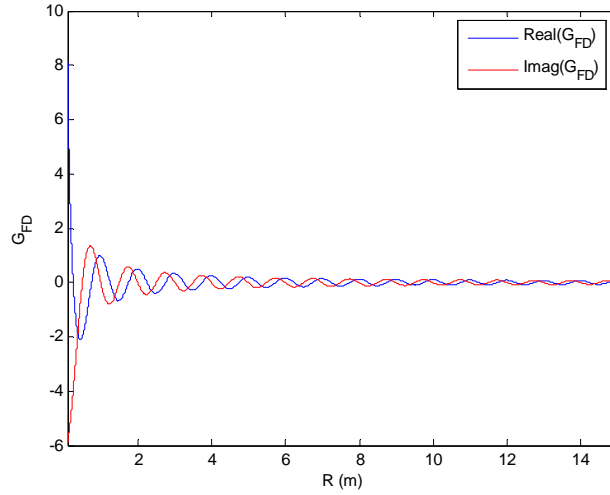


**Figure D.2** The frequency domain Green's function  $G_{FD}$ .

### D.3 Examples

In this thesis, both the time and frequency domain integrals are carried out using the Gaussian quadrature rules for a triangular region [40] using the RWG basis functions. The number of sampling points is varied from 1 to 79 in the evaluation of the integrals encountered in Eqs. (D.1) – (D.4).

Example 1 considers two triangular spatial basis functions parallel to each other, as shown in Figure D.3. For the time domain Green's function,  $s$  is chosen as  $5 \times 10^9$  and  $a - b = 50$ . For the frequency domain Green's function,  $k$  is chosen to be  $2\pi$ . The integral values in the evaluation of the expressions in Eqs. (D.1) and (D.3) are listed in Table D.1 and Table D.2. Both expressions converge when one increases the number of the sampling quadrature points. Because the exact values for the integrals are not known a priori, the results obtained by using 79 points are considered to be the ones closest to the accurate values. The relative error at this value is plotted in Figure D.4. The relative error is defined as



$$Error(n) = \frac{|A_{mn}^{TD/FD}(79) - A_{mn}^{TD/FD}(n)|}{|A_{mn}^{TD/FD}(79)|} \quad (D.11)$$

where  $A_{mn}^{TD/FD}(n)$  is the time or frequency domain integral in Eqs. (D.1) and (D.3) computed with  $n$  sampling points, and the operator  $|\bullet|$  is the absolute value of the function. Figure D.4 shows that when one uses 7 sampling points, which is a very common case for these computations, the frequency domain integral can have an error of less than 1% while the error in the time domain is around 10%. A similar phenomenon also appears in the evaluation of the integrals of  $B_{mnab}^{TD}$  and  $B_{mn}^{FD}$  in the Eqs. (D.2) and (D.4); their relative errors are plotted in Figure D.5. In this figure, when the number of sampling points is chosen as 7, the frequency domain integrals has an error of around 0.1% while the time domain expressions provide a relative error of about 10%.

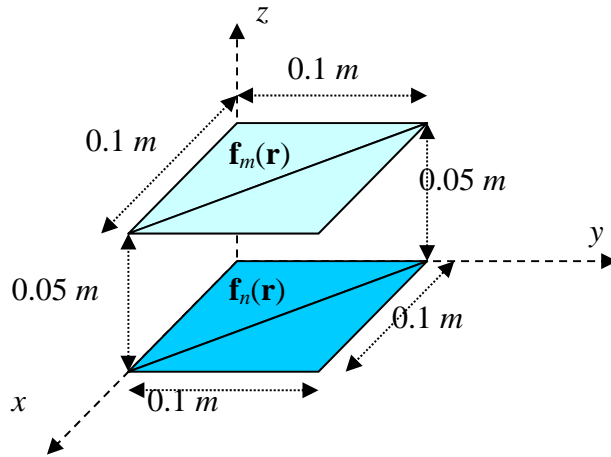


**Figure D.3** Orientation of the two basis functions for Example 1

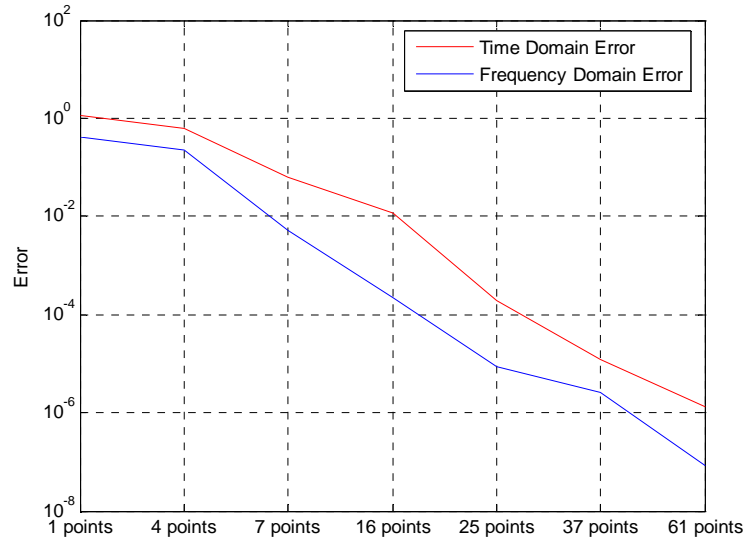


**Figure D.4** Relative error in the evaluation of  $A_{mn}^{TD}$  and  $A_{mn}^{FD}$  for Example 1.

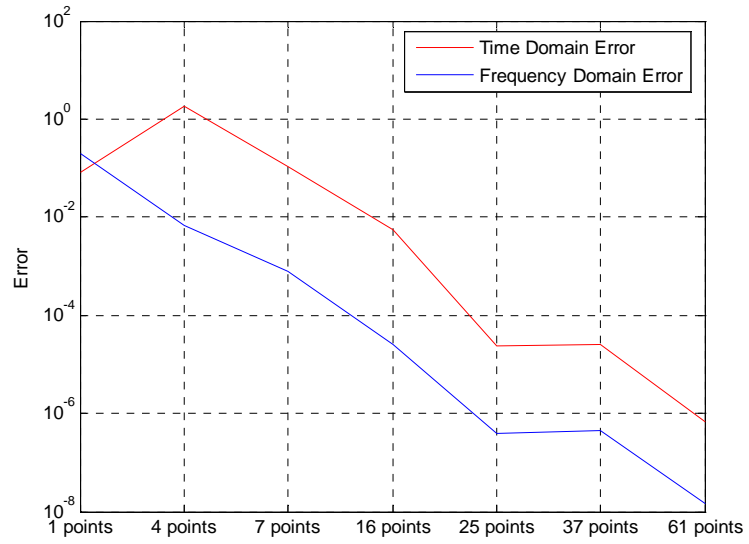


**Figure D.5** Relative error in the evaluation of  $B_{mn}^{TD}$  and  $B_{mn}^{FD}$  for Example 1.

TABLE D.1. Numerical error for time domain integrals

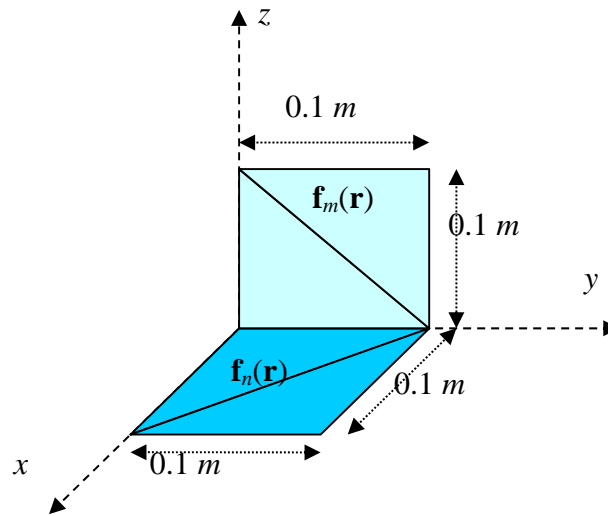
Sampling points	$A_{mnab}^{TD}$
1	1.196862990017365E-006
4	-9.185507229096584E-008
7	-1.415802785348749E-007
16	-1.520710249941450E-007
25	-1.503210213166758E-007
37	-1.502934135708395E-007
61	-1.502913746203929E-007
79	-1.502915693675874E-007

TABLE D.2. Numerical error for frequency domain integrals

Sampling points	$A_{mn}^{FD}$
1	0.1026460570347953E-04– $j$ 0.1601586946542305E-06
4	0.7931528008435943E-05– $j$ 0.1788829860551588E-06
7	0.6072444309197887E-05– $j$ 0.1781290363986577E-06
16	0.6105805417065320E-05– $j$ 0.1781298635103971E-06
25	0.6104483239659091E-05– $j$ 0.1781298635107554E-06
37	0.6104447874541564E-05– $j$ 0.1781298635107529E-06
61	0.6104432328759541E-05– $j$ 0.1781298635107444E-06
79	0.6104431829695501E-05– $j$ 0.1781298635106877E-06

Example 2 uses two triangular patch basis functions that are perpendicular to each other, as shown in Figure D.6. The parameters of  $s$ ,  $k$ ,  $a$ , and  $b$  are the same as in Example 1. The relative error in the evaluations for the quantities  $A_{mnab}^{TD}$  and  $A_{mn}^{FD}$  are listed in Table D.3 and Table D.4. The relative errors of  $A_{mnab}^{TD}$  and  $A_{mn}^{FD}$  are plotted in Figure D.7 and the relative errors of  $B_{mnab}^{TD}$  and  $B_{mn}^{FD}$  are plotted in Figure D.8. Figure D.7 and Figure D.8 show that the errors are much larger than the ones from Example 1. This is because the Green's function varies over a larger value when  $R$  is small, as shown in the Figure D.1 and Figure D.2. In the first example,  $R$  is greater than 0.05m, but in this example, some of the values of  $R$  are close to zero. As implied in Figure D.1 and Figure

D.2, the error in the evaluation of the Green's function is more sensitive to the error in the evaluation of  $R$  for both time and frequency domain cases. In order to get an accurate value for the integral, more sampling points are needed. Figure D.7 and Figure D.8 show that if only 7 sampling points are used in the time domain solver, the errors are around 110% and 60%, respectively. These errors are so large that the results of the solver are unreliable and more sampling points are necessary.



**Figure D.6** The two basis functions for Example 2.

TABLE D.3. Numerical error for time domain integrals

Sampling points	$A_{mab}^{TD}$
1	3.761504994513267E-007
4	-1.152579677805389E-006
7	9.593733385070720E-008
16	-1.317525027949061E-007
25	-9.084526029380924E-008
37	-8.595394401284385E-008
61	-7.911876314641855E-008
79	-7.616760175651086E-008

TABLE D.4. Numerical error for frequency domain integrals

Sampling points	$A_{mn}^{FD}$
1	0.8504782549007540E-05-j0.1596313625583668E-06
4	0.1563952782733322E-04-j0.1788662643803946E-06
7	0.1418624593893488E-04-j0.1784863698059096E-06
16	0.1489178854301966E-04-j0.1784867859716771E-06
25	0.1345273330446101E-04-j0.1784867859718516E-06
37	0.1300656612436935E-04-j0.1784867859718702E-06
61	0.1282336903240997E-04-j0.1784867859718813E-06
79	0.1269753806813858E-04-j0.1784867859718796E-06

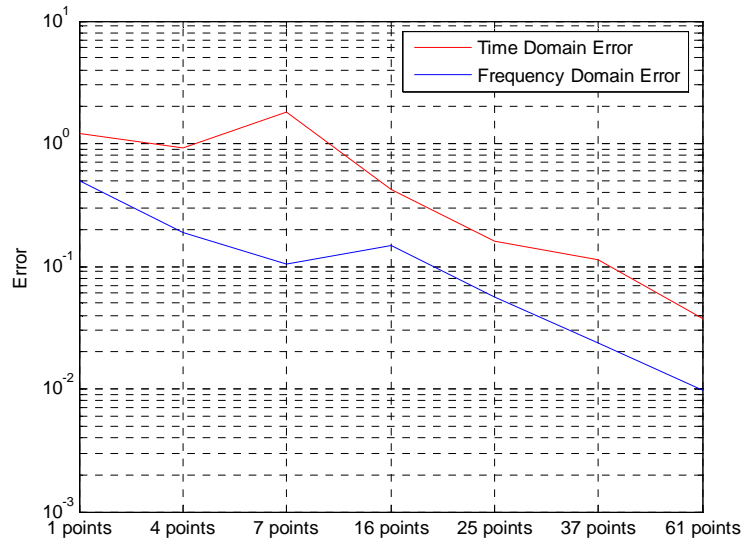
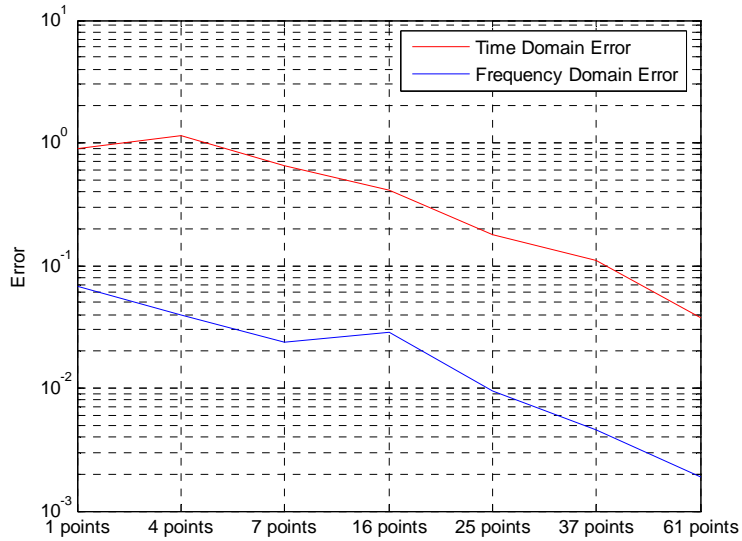
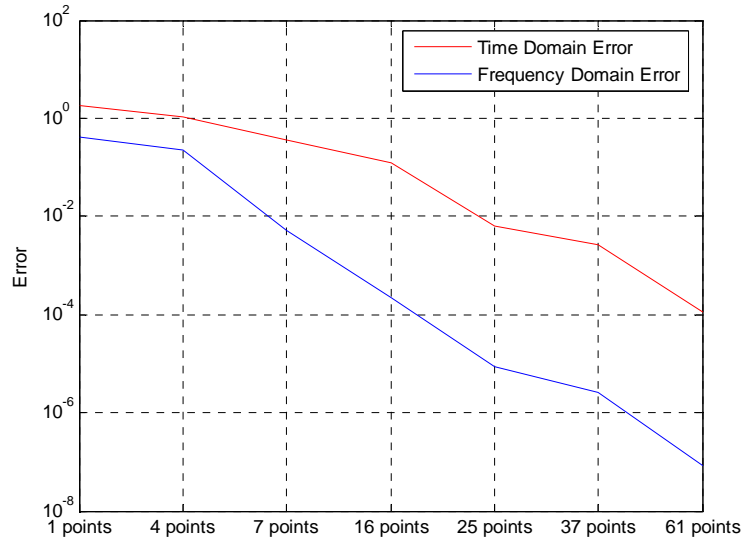


Figure D.7 Relative error in the evaluation of  $A_{mab}^{TD}$  and  $A_{mn}^{FD}$  in Example 2.



**Figure D.8** Relative error in the evaluation of  $B_{mnab}^{TD}$  and  $B_{mn}^{FD}$  in Example 2

Example 3 is the same as Example 1 except that the degree of  $(a - b)$  is changed to 150. All other parameters are the same. The relative errors in the evaluation of  $A_{mnab}^{TD}$  and  $A_{mn}^{FD}$  are plotted in Figure D.9 and the relative errors in the evaluation of  $B_{mnab}^{TD}$  and  $B_{mn}^{FD}$  are plotted in Figure D.10. Comparing these two figures with Figure D.4 and Figure D.5, one can see that as the degree increases, the errors associated with the integrals associated with the time domain Green's function also increase. This is because the time domain Green's function varies more rapidly as the degree gets larger, as seen in Figure D.1. If the number of sampling points is not increased for higher degrees, the error is larger when one uses the marching-on-in-degree solution procedure.



**Figure D.9** Relative error in the evaluation of  $A_{mnab}^{TD}$  and  $A_{mn}^{FD}$  in Example 3.

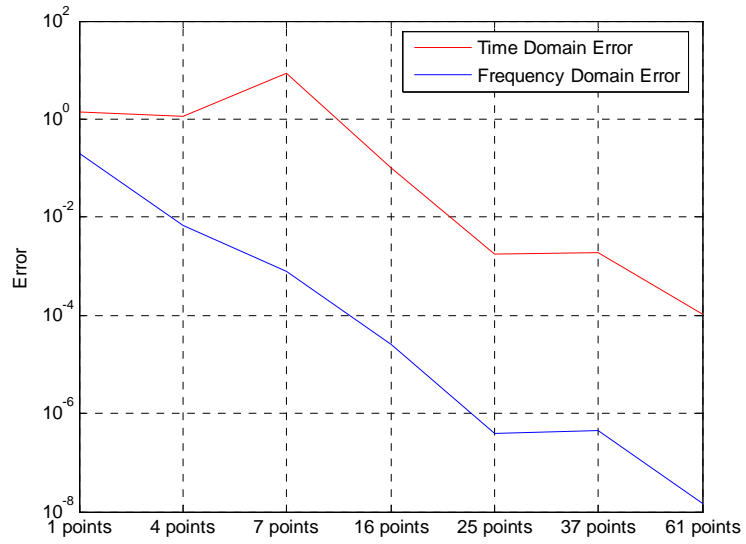


**Figure D.10** Relative error in the evaluation of  $B_{mnab}^{TD}$  and  $B_{mn}^{FD}$  in Example 3

## D.4 Conclusion

Compared to the error associated with a frequency domain solver, the error associated with the evaluation of the matrix elements in a marching-on-in-degree time domain solver is more sensitive to the error in the evaluation of  $R$ . This is because the Green's function varies faster with respect to  $R$ . Therefore, one needs more sampling points in the numerical evaluation of the integrals in order to obtain an accurate result. If one uses the same number of sampling points as used in a frequency domain solver, the errors is much larger. This is especially important when two triangular patches are close in distance to each other or when the degree of the associated Laguerre polynomials is large.



## References

- [1]. R. F. Harrington, *Field Computation by Moment Method*, 1968 :MacMillan
- [2]. S. M. Rao, *Electromagnetic Scattering and Radiation of Arbitrarily-Shaped Surfaces by Triangular Patch Modeling*, PhD Dissertation, University Mississippi, Aug. 1980.
- [3]. S. M. Rao and D. R. Wilton, "Transient scattering by conducting surfaces of arbitrary shape," *IEEE Trans. Antennas Propagat.*, vol. 39, pp.56 -61 1991.
- [4]. S. M. Rao, *Time Domain Electromagnetics*, 1999, Academic.
- [5]. D. S. Weile, G. Pisharody, N. W. Chen, B. Shanker, and E. Michielssen, "A novel scheme for the solution of the time-domain integral equations of electromagnetics," *IEEE Trans. Antennas Propag.* vol 52, pp. 283–295, 2004
- [6]. P. Wang, M. Y. Xia, J. M. Jin and L. Z. Zhou, "Time domain integral equation solvers using quadratic b-spline temporal basis functions," *Microwave and Optical Tech. Letter*, Vol. 49, No. 5, pp.1154-1159, May 2007.
- [7]. D. A. Vechinski and S. M. Rao, "A stable procedure to calculate the transient scattering by conducting surfaces of arbitrary shape," *IEEE Trans. Antennas Propag.*, Vol. 40, pp. 661–665, 1992.
- [8]. A. Sadigh and E. Arvas, "Treating the instabilities in marching-on in time method from a different perspective," *IEEE Trans. Antennas Propag.*, Vol. 41, pp. 1695–1702, 1993.
- [9]. F. P. Andriulli, H. Bagci, F. Vipiana, G. Vecchi, and E. Michielssen, "Analysis and regularization of the TD-EFIE low-frequency breakdown," *IEEE Trans. Antennas*

- Propagat.*, vol. 57, pp. 2034-2-46, 2009.
- [10]. F. P. Andriulli, H. Bagci, F. Vipiana, G. Vecchi, and E. Michielssen, "A marching-on-in-time hierarchical scheme for the time domain electric field integral equation," *IEEE Trans. Antennas Propagat.*, vol. 55, pp. 3734-3738, 2007.
- [11]. H. Bagci, A. E. Yilmaz, Jian-Ming Jin, and E. Michielssen, "Fast and rigorous analysis of EMC/EMI phenomena on electrically large and complex structures loaded with coaxial cables," *IEEE Trans. Electromagn. Comp.*, vol. 49, pp. 361-381, 2007.
- [12]. A. E. Yilmaz, J. M. Jin, and E. Michielssen, "Analysis of low-frequency electromagnetic transients by an extended time-domain adaptive integral method," *IEEE Trans. Adv. Pack.*, vol. 30, pp. 301-312, 2007.
- [13]. H. Bagci, A. E. Yilmaz, V. Lomakin, and E. Michielssen, "Fast solution of mixed-potential timedomain integral equations for half-space environments," *IEEE Trans. Geosci. Remote Sensing*, vol. 43, no. 2, pp. 269-279, 2005.
- [14]. R. A. Wildman, G. Pisharody, D. S. Weile, S. Balasubramaniam, and E. Michielssen, "An accurate scheme for the solution of the time-domain integral equations of electromagnetics using higher order vector bases and bandlimited extrapolation," *IEEE Trans. Antennas Propagat.*, vol. 52, pp. 2973-2984, 2004.
- [15]. B. H. Jung, T. K. Sarkar, Y.-S. Chung, and Z. Ji, "An accurate and stable solution for transient scattering and radiation from wire structures," *Microwave Opt. Technol. Lett.*, Vol. 34, pp. 354-359, 2002.
- [16]. Z. Ji, T. K. Sarkar, B. H. Jung, Y.-S. Chung, M. Salazar-Palma, and M. Yuan, "A stable solution of time domain electric field integral equation for thin-wire antennas

- using the laguerre polynomials,” *IEEE Trans. Antennas Propag.*, Vol. 52, No. 10, pp. 2641–2649, Oct. 2004.
- [17]. Z. Ji, T. K. Sarkar, B. H. Jung, M. Yuan, and M. Salazar-Palma, “Solving time domain electric field integral equation without the time variable,” *IEEE Trans. Antennas Propag.*, Vol. 54, No. 1, pp. 258–262, Jan. 2006.
- [18]. A. D. Poularikas, *The Transforms and Applications Handbook*, Piscataway, NJ: IEEE Press, 1996.
- [19]. N. N. Lebedev, *Special Functions and Their Applications*, Englewood Cliffs, NJ, Prentice-Hall. 1963.
- [20]. Z. Mei, Y. Zhang, T. K. Sarkar, and B. H. Jung, A. Garcia-Lamperez, M. Salazar-Palma, "An improved marching-on-in-degree method using a new temporal basis," *IEEE Trans. Antennas Propag.*, vol.59, no.12, pp.4643,4650, Dec. 2011.
- [21]. B. G. Mikhailenko, “Spectral laguerre method for the approximate solution of time dependent problems,” *Applied Mathematics Letters*, Vol. 12, pp. 105-110, 1999.
- [22]. Y. Hua and T. K. Sarkar, "Design of optimum discrete finite duration orthogonal Nyquist signals," *IEEE Trans. on Acoust, Speech Signal Process.*, Vol. 36, pp. 606–608, 1988.
- [23]. T. K. Sarkar, M. Salazar-Palma, and M. C. Wicks, *Wavelet Applications in Engineering Electromagnetics*, Artech House, Norwood, Mass. 2002.
- [24]. Z. Mei, T. K. Sarkar, and M. Salazar-Palma, “The Design of an Ultrawideband T-Pulse With a Linear Phase Fitting the FCC Mask,” *IEEE Trans. Antennas Propag.*, vol.59, no.4, pp.1432,1436, April 2011
- [25]. S. H. Yeung, Z. Mei, T. K. Sarkar, and M. Salazar-Palma, “An ultrawideband T-

- pulse fitting the FCC mask using a multiobjective genetic algorithm,” *Microwave and Wireless Components Letters, IEEE* , vol.22, no.12, pp.615,617, Dec. 2012.
- [26]. Blaise Barney, *Message Passing Interface (MPI)*, Available at: <https://computing.llnl.gov/tutorials/mpi/>.
- [27]. Netlib Repository at UTK and ORNL, *The ScaLAPACK Project*. Available at: <http://www.netlib.org/scalapack/>.
- [28]. T. J. Fountain , *Parallel Computing: Principles and Practice*, Cambridge University Press, 2006
- [29]. A. D. Poularikas, *The Transforms and Applications Handbook*, IEEE Press, 1996.
- [30]. T. W. Parks, “Choice of time scale in Laguerre approximations using signal measurements,” *IEEE Trans. Automat. Contr.*, vol. 16, pp. 511, Oct. 1971.
- [31]. G. J. Clowes, “Choice of the optimal time-scaling factor for linear system approximations using orthonormal Laguerre functions,” *IEEE Trans. Automat. Contr.*, Vol. AC-10, pp.487 - 489, Oct. 1965.
- [32]. L. Wang and W. Cluett, “Optimal choice of time-scaling factor for linear system approximations using Laguerre models,” *IEEE Trans. Autom. Control*, Vol. 39, pp.1463, Jul 1994.
- [33]. D. P. Bouche, F. A. Molinet, and R. Mittra, “Asymptotic and hybrid techniques for electromagnetic scattering,” *Proc. IEEE*, vol. 81, no. 12, pp. 1658-1684, Dec. 1993.
- [34]. G. A. Thiele, “Overview of selected hybrid methods in radiating system analysis,” *Proc. IEEE*, vol. 80, no. I, pp. 67-78, Jan. 1992.
- [35]. U. Jakobous and F. M. Landstorfer, “Improved PO-MM hybrid formulation for scattering from three dimensional perfectly conducting bodies of arbitrary shape,”

- IEEE Trans. Antennas Propag.*, vol. AP-43, pp. 162, 1995.
- [36]. M. Djordjevic and B. M. Notaros, "Higher order hybrid method of moments-physical optics modeling technique for radiation and scattering from large perfectly conducting surfaces," *IEEE Trans Antennas Propag.*, vol. 53, pp. 800 2005.
- [37]. Y. Zhang, X. W. Zhao, D.G. Donoro, S. W. Ting, and T. K. Sarkar, "Parallelized hybrid method with higher-order MoM and PO for analysis of phased array antennas on electrically large platforms," *IEEE Trans. Antennas Propag.*, vol. 58, pp. 4110 2010.
- [38]. B. H. Jung, T. K. Sarkar, Y. Zhang, etc., *Time and Frequency Domain Solutions of EM Problems Using Integral Equations and a Hybrid Methodology*, New York, IEEE Press, 2010
- [39]. Z. Ji, T. K. Sarkar, B. H. Jung, Y.-S. Chung, M. Salazar-Palma, and M. Yuan, "A Stable Solution of Time Domain Electric Field Integral Equation for Thin-Wire Antennas Using the Laguerre Polynomials," *IEEE Trans. Antennas Propag.*, Vol. 52, No. 10, pp. 2641–2649, Oct. 2004.
- [40]. D. A. Dunavant, "High degree efficient symmetrical Gaussian quadrature rules for the triangle," *Int. J. Num. Meth. Eng.*, Vol. 21, pp.1129–1148, 1985.



## Publications

- [1]. B. H. Jung, T. K. Sarkar, S. W. Ting, Y. Zhang, **Z. Mei**, Z. Ji, M. Yuan, A. De, M. Salazar-Palma, and S. M. Rao, *Time and Frequency Domain Solutions of EM Problems Using Integral Equations and a Hybrid Methodology*, Wiley-IEEE, 2010 (Two of the booke chapters).
- [2]. **Z. Mei**, T. K. Sarkar, and M. Salazar-Palma, "The design of an ultrawideband T-pulse with a linear phase fitting the FCC mask," *IEEE Trans. Antennas Propag.*, vol.59, no.4, pp.1432,1436, April 2011.
- [3]. **Z. Mei**, Y. Zhang, T. K. Sarkar, B. H. Jung, A. Garcia-Lamperez, and M. Salazar-Palma, "An improved marching-on-in-degree method using a new temporal basis," *IEEE Trans. Antennas Propag.*, vol.59, no.12, pp.4643,4650, Dec. 2011.
- [4]. **Z. Mei**, Y. Zhang, T.K.Sarkar, M. Salazar-Palma, and B. H. Jung, "Analysis of arbitrary frequency-dependent losses associated with conducting structures in a time-domain electric field integral equation," *Antennas and Wireless Propagation Letters, IEEE* , vol.10, no., pp.678,681, 2011.
- [5]. **Z. Mei**, Y. Zhang, X. Zhao, B. H. Jung, T.K.Sarkar, and M. Salazar-Palma, "Choice of the scaling factor in a marching-on-in-degree time domain technique based on the associated laguerre functions," *IEEE Trans. Antennas Propag.*, vol.60, no.9, pp.4463,4467, Sept. 2012
- [6]. **Z. Mei**, T.K.Sarkar, and M. Salazar-Palma, "A study of wideband pulse shape distortion due to presence of obstacles," *Microw. Opt. Technol. Lett.*, vol. 55: pp. 1618–1622,2013.

- [7]. **Z. Mei**, T.K.Sarkar, and M. Salazar-Palma, "A Study of Negative Permittivity and Permeability for Small Sphere," *Antennas and Wireless Propagation Letters, IEEE* , vol.12, no., pp.1228-1231, 2013.
- [8]. **Z. Mei**, B. H. Jung, Y. Zhang, X. W. Zhao, T. K. Sarkar, and M. Salazar-Palma, "A study on the numerical accuracy of the matrix elements in a time domain MOD methodology," *Progress In Electromagnetics Research M*, Vol. 33, 185-196, 2013.
- [9]. **Z. Mei**, S. H. Yeung, T. K. Sarkar, and M. Salazar-Palma, "A study of transmission of RF signal with single conductor wire," *Microwave and Optical Technology Letters*, Volume 56, Issue 1, pages 124–127, January 2014
- [10]. **Z. Mei**, Y. Zhang, and T. K. Sarkar, "Time domain marching-on-in-degree method for the conducting objects with loading," *Antennas and Propagation Society International Symposium (APSURSI), 2010 IEEE* , vol., no., pp.1,4, 11-17 July 2010.
- [11]. **Z. Mei**, Y. Zhang, and T. K. Sarkar, "Solving time domain EFIE using higher order basis functions and marching-on in degree method," *Antennas and Propagation Society International Symposium, 2009. APSURSI '09. IEEE* , vol., no., pp.1,4, 1-5 June 2009.
- [12]. **Z. Mei**, T. K. Sarkar, Y. Zhang, and M. Salazar-Palma, "A hybrid method of moment (MoM) and physical optics (PO) technique in the time domain," *Antennas and Propagation Society International Symposium (APSURSI), 2012 IEEE* , vol., no., pp.1,2, 8-14 July 2012
- [13]. **Z. Mei**, Y. Zhang, and T. K. Sarkar, "Improvements in the marching-on-in-degree method for time domain integral equations," *Antennas and Propagation (APSURSI), 2011 IEEE International Symposium on* , vol., no., pp.2350,2353, 3-8 July 2011



- [14]. S. H. Yeung, **Z. Mei**, T. K. Sarkar, and M. Salazar-Palma, "An ultrawideband T-pulse fitting the FCC mask using a multiobjective genetic algorithm," *Microwave and Wireless Components Letters, IEEE* , vol.22, no.12, pp.615,617, Dec. 2012
- [15]. B. H. Jung, **Z. Mei**, and T. K. Sarkar, "Transient wave propagation in a general dispersive media using the laguerre functions in a marching-on-in-degree (MOD) methodology," *Progress In Electromagnetics Research*, Vol. 118, 135-149, 2011.
- [16]. S. H. Yeung, **Z. Mei**, T. K. Sarkar, and M. Salazar-Palma, "Design and testing of a single-layer microstrip ultrawideband 90° differential phase shifter," *Microwave and Wireless Components Letters, IEEE* , vol.23, no.3, pp.122,124, March 2013
- [17]. W. Zhao, A. De, **Z. Mei**, Y. Zhang, and T. K. Sarkar, "Design of a two-element folded-Yagi antenna with super-directivity," *Antennas and Propagation (APSURSI), 2011 IEEE International Symposium on* , vol., no., pp.942,944, 3-8 July 2011
- [18]. B. H. Jung, **Z. Mei**, T. K. Sarkar, and M. Salazar-Palma, "Analysis of transient wave propagation in an arbitrary frequency-dispersive media using the associated Laguerre functions in the FDTD-MOD method," *Microw. Opt. Technol. Lett.*, vol. 54: pp.925–930, 2012
- [19]. Y. Yan, Y. Zhang, X. W. Zhao, **Z. Mei**, W. Zhao, and T. K. Sarkar, "Time-domain method of moments accelerated by adaptive cross approximation algorithm," *Antennas and Propagation Society International Symposium (APSURSI), 2012 IEEE* , vol., no., pp.1,2, 8-14 July 2012

# VITE

Zicong Mei

**Place of birth:** Guangzhou, China

**Date of birth:** April 20, 1985

## **Education**

**Syracuse University**, Syracuse, NY

PH.D. in Electrical and Computer Engineering, August 2008 – May 2014.

Master of Electrical Engineering, August 2013 – December 2013.

**University of Science and Technology of China**, Anhui, China

Bachelor in Electrical and Electronic Engineering, September 2004 - July 2008.